Fall 2020

30 GHz Path Loss Modeling and Performance Evaluation for Noncoherent M-ary Frequency Shift Keying in the 30 GHz Band

Mohanad Razak Mohsen

30 GHz Path Loss Modeling and Performance Evaluation for Non-coherent M-ary Frequency Shift Keying in the 30 GHz Band

by

Mohanad Razak Mohsen

Bachelor of Computer Engineering
Basrah University, 2003

Master of Science
Brunel University, 2010

Submitted in Partial Fulfillment of the Requirements

For the Degree of Doctor of Philosophy in

Electrical Engineering

College of Engineering and Computing

University of South Carolina

2020

Accepted by:

David Matolak, Major Professor

Guoan Wang, Committee Member

Alphan Sahin, Committee Member

Jason Bakos, Committee Member

Cheryl L. Addy, Vice Provost and Dean of the Graduate School

ABSTRACT

A candidate millimeter-wave (mmWave) frequency band and modulation scheme that could fit to many present and future applications has been presented in this work. As is being explored by industry, we also suggest the 30 GHz band as a candidate carrier frequency and non-coherent frequency shift keying (NC-FSK) as a potential modulation scheme for future communication applications. The primary applications are aimed at 5th generation (5G) cellular type systems. Propagation measurements were conducted for outdoor and indoor environments using directional horn antennas for both co-polarized and cross-polarized antenna configurations to model the path loss for our candidate band. The measurements were conducted in typical line-of-sight (LOS) and non-LOS (NLOS) environments in a large building on the University of South Carolina campus, specifically at Swearingen Engineering Center. Several propagation path loss (PL) models are presented based upon this collected data. We can use these PL models in link budgets for estimating transmit power, antenna gains, receiver characteristics (e.g., noise figure), and link distances. The measurements also contribute to the body of knowledge on wireless channel propagation path loss for bands near 30 GHz.

Another measurement campaign was also conducted at the USC campus to measure a unique and complicated vegetation attenuation that may be considered a large challenge to mmWave systems. Radio wave attenuation and depolarization effects through several broadleaf evergreen shrubs at 31 GHz are reported, based upon measurements. To obtain

a comparative reference for this mmWave attenuation, another measurement was also conducted at 5 GHz. From these measurements, we analyzed the proportional relationships between the attenuation and the shrub density (related to species), depth, and measurement geometry. Three different shrub species with different densities and depths, and for different measurement geometries, were employed. Results are in terms of measured specific attenuations at 31 GHz—the attenuation in dB/m. These will also be useful for link budget design, and outdoor and outdoor-indoor models for future mmWave communication.

For our 5G modulation scheme candidate, we evaluate its performance at 31 GHz via an empirical 3-D mmWave channel simulator: the NYUSIM channel model. As with all digital communication systems, performance is measured in terms of error ratios, and we evaluate the bit error rate (BER) performance of NC-FSK for different symbol rates over a variety of wireless mmWave channels. The NC-FSK scheme is known to be energy efficient for large alphabet size, and this is one of its virtues. Another is that since it is a form of FM, nonlinear amplification (far less costly than linear amplification) can be used. The performance evaluations enable us to present enhancements and trade-offs that can be done to improve the system performance by adjustment of the design parameters, i.e., modulation alphabet size and symbol rate, which together determine bandwidth (BW).

TABLE OF CONTENTS

ABSTRACT iii

LIST OF TABLES viii

LIST OF FIGURES ix

LIST OF ABBREVIATIONS xii

CHAPTER 1: INTRODUCTION 1

1.1 5G CHALLENGES 2

1.2 STATISTICAL mmWAVE CHANNEL MODELS 8

1.3 5G EXPECTED APPLICATIONS 10

1.4 DISSERTATION OBJECTIVES 12

1.5 DISSERTATION CONTRIBUTIONS 12

CHAPTER 2: LITERATURE REVIEW 15

2.1 5G CANDIDATE MODULATIONS 15

2.2 PATH LOSS MEASUREMENTS AND MODELING AT mmWAVE BAND 17

2.3 VEGETATION ATTENUATION AT mmWAVE 19

CHAPTER 3: LARGE-SCALE PATH LOSS MEASUREMENTS AND MODELING 22

3.1 BACKGROUND THEORY 23

3.2 MEASUREMENT EQUIPMENT AND TEST CONFIGURATION 27

3.3 OUTDOOR MEASUREMENTS 30

3.4 INDOOR MEASUREMENTS IN INTERIOR CORRIDORS 35

3.5 RESULTS 40
3.6 DISCUSSION 43
3.7 SUMMARY 46
CHAPTER 4: VEGETATION (SHRUB) ATTENUATION MEASUREMENTS 48
4.1 BACKGROUND 48
4.2 WORK MOTIVATION 49
4.3 MEASUREMENT ENVIRONMENT 50
4.4 MEASUREMENT EQUIPMENT 50
4.5 MEASUREMENT SETUP 51
4.6 MEASUREMENT STEPS 53
4.7 RESULTS 54
4.8 CONCLUSION 60
CHAPTER 5: 5G CANDIDATE WAVEFORM 62
5.1 BACKGROUND 62
5.2 CONSTANT ENVELOPE MODULATION SCHEMES 63
5.3 MFSK FEATURES AND APPLICATIONS 65
5.4 NON-COHERENT MFSK FEATURES 67
5.5 NC-MFSK BIT ERROR PROBABILITY OVER THE AWGN CHANNEL 68
5.6 CANDIDATE MODULATION SCHEME EVALUATION AT 31 GHz 70
5.7 FLAT AND FREQUENCY SELECTIVE CHANNELS 70
5.8 NC-MFSK EVALUATION 71
5.9 FSK IN PRESENCE OF INTER-SYMBOL INTERFERENCE (ISI) 75

5.10 NC-MFSK OVER NYUSIM 76
5.11 BANDWIDTH-POWER EFFICIENCY TRADE-OFF IN NC-MFSK 86
5.12 ADAPTIVE MODULATION ORDER SYSTEMS 86
CHAPTER 6: CONCLUSIONS AND FUTURE WORK 94
6.1 DISSERTATION CONCLUSIONS 94
6.2. FUTURE WORK 98
REFERENCES 100
APPENDIX A: FREQUENCY MODULATION & DEMODULATION 110
APPENDIX B: NON-COHERENT DETECTION 113

LIST OF TABLES

Table 3.1 CI, CIX, and FI PL model parameters for LOS outdoor at 31 GHz 32

Table 3.2 CI PL model parameters for LOS interior courtyard at 31 GHz 35

Table 3.3 CI, CIX, and FI PL model parameters for NLOS 2nd Floor/Wing "A" Corridor at 31 GHz 40

Table 3.4 CI, CIX, and FI PL model parameters for LOS 1st, 2nd and 3rd floor corridors at 31 GHz 43

Table 3.5 CI path loss model parameters for different environments 44

Table 3.6 List of PLE and standard deviation values from the literature 45

Table 4.1 Attenuation results of Japanese Boxwood shrub 55

Table 4.2 Measurement and results of Yaupon holly shrub 57

Table 4.3 Measurement results of Shamrock Holly shrub 57

Table 4.4 Average specific attenuations for two frequencies vs. distance from antenna to shrub B 60

Table 5.1 Transmit signal parameters for Flat Channel Case 77

Table 5.2 Transmit signal parameters for Freq. Selective Channel Case 78

Table 5.3 Transmit signal parameters for NC-128FSK 81

LIST OF FIGURES

Figure 3.1 Transmitter and receiver block diagram....28

Figure 3.2 Google Earth ® view (2017) of actual outdoor measurement environment, Swearingen Engineering Center, 65 Tx-Rx measurement points....31

Figure 3.3 V-V and V-H measured PL scatter plots, CI, CIX and FI PL models vs. distance for 31 GHz outdoor LOS setting....33

Figure 3.4 Interior Courtyard, LOS measurement environment, Swearingen Engineering Center, 18-25 meter Tx-Rx separation distance....34

Figure 3.5 V-V Measured PL scatter plots, best fit CI PL models for 31 GHz in interior courtyard/Swearingen Center, LOS environment....35

Figure 3.6 1st floor corridor photograph (left), and floor plan (right), 76 Tx-Rx measurement points....38

Figure 3.7 2nd floor / Wing (A) corridor photograph (left), and floor plan (right). NLOS scenario, 37 Tx-Rx measurement points....38

Figure 3.8 2nd floor / Wing (D) corridor photograph (left), and floor plan (right), 62 Tx-Rx measurement points....39

Figure 3.9 3rd floor corridor photograph (left), and floor plan (right), 58 Tx-Rx measurement points....39

Figure 3.10 V-V and V-H measured PL scatter plots, best fit CI, CIX and FI PL models for 31 GHz in 2nd Floor/wing “A” corridor/ Swearingen Center, NLOS Indoor environment....40

Figure 3.11 V-V and V-H Measured PL scatter plots, best fit CI, CIX and FI PL models for 31 GHz in 1st Floor corridor, LOS Indoor environment....41

Figure 3.12 V-V and V-H Measured PL scatter plots, best fit CI, CIX, and FI PL models for 31 GHz in 2nd Floor/wing “D” corridor/ Swearingen Center, LOS Indoor environment....42

Figure 3.13 V-V and V-H Measured PL scatter plots, best fit CI, CIX, and FI PL models for 31 GHz in 3rd Floor corridor/Swearingen Center, LOS Indoor environment 42

Figure 4.1 Measurement setup for 31 GHz shrub attenuation measurements 52

Figure 4.2 Measurement setup for 5 GHz Tx (left), Rx (right), shrub attenuation measurements 52

Figure 4.3 Measurement geometry to average the small-scale fading effect 54

Figure 4.4 Directional measurement setup with Tx & Rx antenna at edge of Japanese Boxwood shrubs A; lower left inset is close up of the dense branch distribution inside shrubs 56

Figure 4.5 Directional measurement setup with Tx and Rx antenna deployed at edge of Yaupon holly shrubs B; lower left inset is close up of dense branch distribution inside shrubs 57

Figure 4.6 Directional measurement setup with Tx & Rx antenna at edge of Shamrock holly shrubs C; lower center inset shows close up of medium density branch distribution inside shrubs 58

Figure 4.7 Different measurement distances via different shrub-Rx antenna separation distances 60

Figure 5.1 NC-MFSK error probability vs. Eb/N0 for different modulation order M 69

Figure 5.2 Example (1) Power Delay Profile (PDP) generated by NYUSIM for UMi NLOS channel 77

Figure 5.3 Spectrum of NC-8FSK over a flat-fading channel 77

Figure 5.4 Spectrum of NC-8FSK over frequency-selective channel 79

Figure 5.5 Transmitted and Received Signals through both Flat and Freq.-Selective channels 79

Figure 5.6 System performance over NLOS Micro-Urban channel for different symbol times 80

Figure 5.7 Example (2) Power Delay Profile (PDP) generated by NYUSIM for UMi LOS channel 81

Figure 5.8 Power Spectrum of NC-128FSK Tx and Rx signal, Tsym=80 ns, Rb=87.5 Mbps....83

Figure 5.9 Power Spectrum of NC128FSK Tx and Rx signal, Tsym=160 ns, Rb=43.75....83

Figure 5.10 Power Spectrum of NC-128FSK transmitted and received signal, Tsym=200 ns, Rb=35 Mbps....84

Figure 5.11 Power Spectrum of NC-128FSK Tx and Rx signal, Tsym=240 ns, Rb=29.19 Mbps....84

Figure 5.12 NC-128FSK system performance over LOS Micro-Urban channel for different symbol times....85

Figure 5.13 BER vs. throughput trade-offs for fixed BW system....88

Figure 5.14 NC-8FSK system performance over LOS Micro-Urban channel for different data rate....90

Figure 5.15 NC-32FSK system performance over LOS Micro-Urban channel for different data rate....91

Figure 5.16 NC-8, 32, 128FSK system performance over LOS Micro-Urban channel....92

Figure 5.17 NC-128FSK system performance over LOS Micro-Urban channel....92

Figure 5.18 NC-128FSK system performance over LOS Micro-Urban channel for different BW....93

LIST OF ABBREVIATIONS

3GPP ..... 3rd Generation Partnership Project

ABG ..... modelAlpha-Beta-Gamma Model

ACI..... Adjacent Channel Interference

ADC ..... Analog-To-Digital Converter

AWGN ..... Additive White Gaussian Noise

BER..... Bit Error Rate

BPSK ..... Binary Phase Shift Keying

BW ..... Bandwidth

C-MFSK..... Coherent MFSK

CI..... Close-In

CIX..... Close-In With Cross-Polarization Discrimination

cmWave ..... Centimeter Wave

DDM ..... Direct Digital Modulation

DSPs.....Digital Signal Processors

eMBB ..... Enhanced Mobile Broadband

EMC .....Electromagnetic Compatibility

FBMC-OQAM ..... Filter Bank Multi-Carrier with Offset QAM

FEC ..... Forward error correction

FI ..... Floating-Intercept

FIB .....Fast Information Block

FIC ..... Fast Information Channel

FQAM ..... Frequency Quadrature Amplitude Modulation

FSPL ..... Free Space Path Loss

GFDM-OQAM ..... Generalized frequency division multiplexing with Offset QAM

HPBW ..... Half Power Beam Width

IQ ..... In-phase and Quadrature

ISI ..... Inter-Symbol Interference

ITU-R ..... International Telecommunications Union Recommendation

LOS ..... Line-of-Sight

LTE ..... Long Term Evolution

MCM ..... Multicarrier Modulation

MFSK ..... M-ary Frequency-Shift Keying

MIMO ..... Multiple-Input And Multiple-Output

mMTC ..... Massive Machine-Type Communication

mmWave ..... Millimetre Wave

MPC ..... Multi-Path Component

MUT ..... Material Under Test

NC-FSK ..... Noncoherent Frequency-Shift-Keying

NLOS ..... non-LOS

NPA ..... non-Linear Power Amplifiers

OFDM ..... Orthogonal Frequency Division Multiplexing

OFDMA ..... Orthogonal Frequency Division Multiplexing Access

OTFS ..... Orthogonal Time Frequency Space

PAPR ..... Peak To Average Power Ratio

PEP..... Peak Envelope Power

PL..... Path Loss

PLE ..... Path Loss Exponent

PLL ..... Phase-Locked Loop

PN ..... Phase Noise

PSK ..... Phase shift keying

QAM ..... Quadrature Amplitude Modulation

QAM ..... Quadrature amplitude modulation

QPSK ..... Quadrature Phase Shift Keying

R.M.S. DS..... Root-Mean-Square Delay Spread

Rx..... Receiver

SC-FDMA..... Single Carrier Frequency Division Multiple Access

SNR..... Signal-to-Noise Ratio

Tx ..... Transmitter

UHF ..... Ultra-High Frequency

URLLC ..... Ultra-Relaible Low-Latency Communication

V-H ..... Vertical Antenna Polarization Transmit, Horizontal Receive

V-Omni ..... Vertical Antenna Polarization Transmit, Omni Receive

V-V ..... Vertical Antenna Polarization Transmit, Vertical Receive

VCO ..... Voltage Controlled Oscillator

WCP-COQAM..... Windowed Cyclic Prefix-Circular OQAM

XPD ..... Cross-Polarization Discrimination

CHAPTER 1

INTRODUCTION

Within industry and academia there is significant current activity in research and development toward the next generation of mobile broadband technologies, the 5th generation (5G). Coupled with this there is increasing interest in identifying the specific frequency bands that will be needed to deliver 5G services. At this time, there is no overall consensus on what 5G will actually be, although some initial 5G service are being offered by several service providers. Service operators have begun investigating mmWave technology to evaluate the best candidate frequencies for use in mobile applications. The International Telecommunication Union (ITU) and cellular industry organization Third Generation Partnership Project (3GPP) have aligned on a plan for two phases of research for 5G standards. The first phase research is for frequencies under 40 GHz and the second phase will focus on frequencies up to 100 GHz [1]. Furthermore, in an effort to globally align the standardization of mmWave frequencies, the ITU released a list of proposed globally viable frequencies between 24 GHz and 86 GHz after the most recent World Radiocommunications Conference (WRC) [2]. While the ITU, 3GPP, and other standards organizations have decided on 2020 as the deadline for the 5G standard to be defined [3], cellular providers are working on an accelerated schedule for delivering 5G services. Through these various groups, a set of frequencies are beginning to emerge as the candidates for 5G: 28 GHz, 39 GHz, and 72 GHz [4]. The "door is still open" for any

candidate frequency that satisfies the following conditions: first, this candidate should have a low oxygen absorption rate to make it more viable for long distance communications, unlike 60 GHz, which has approximately 20 dB/km loss due to oxygen absorption [5]; second, the candidate frequency should function well in multipath environments and be usable for non-line-of-sight communications. Another important criterion for 5G is that it should carry a very high data rate, e.g., a 1 Gbps downlink to start with and greater in the future. Attractive 5G candidates will also be more energy efficient than their predecessors.

Even though there are many millimeter frequencies that have been tested as candidates for the next wireless communication generation, several features of the 30 GHz band made it our first choice for investigation. We specifically consider 31 GHz, but term this the "30 GHz band." One of these features is that for any mmWave band, 30 GHz will have a relatively small path loss (PL); higher frequencies will have larger path loss. Furthermore, larger signal bandwidth will challenge hardware performance (e.g., amplifiers) and wide bandwidth and higher radio frequency (RF) components will (at least initially) be more complex and expensive. In addition, 30 GHz represents the approximate upper limit of mainstream civil satellite bands, the Ka band, and second, is the approximate upper working limit of some traditional circuit construction techniques, using bond wires for example [6]. Our second motivation is that there are still numerous indoor (and outdoor) settings in which mmWave channel characteristics have not been measured, and similarly, not all frequencies in the mmWave bands, (30-300 GHz) [3], have been investigated.

1.1 5G CHALLENGES

5G networks intended to work at high radio frequencies (millimeter waves), which have the benefit of being able to support large data rates, will be limited in range. Data

transferred through these types of networks is more easily blocked by common objects like trees and buildings. Cities will probably need to install extra repeaters to spread out the waves for extended range, while also maintaining consistent data rates in denser population areas. This will require further infrastructure (e.g., more base stations per unit area), and this will lead to increase the cost.

Higher frequencies enable highly directional radio waves, meaning they can be targeted or aimed, a practice called beamforming. The challenge is that 5G antennas, while being able to handle more users and data, radiate over shorter distances. Working at such high frequencies will produce several challenges, and we explain only a few examples of these challenges in the context of this dissertation.

1. PATH LOSS

In line-of-sight (LOS) communication, the most fundamental relationship between the transmitted and received power is given by Friis' free space transmission equation (1.1) that describes the received power P_r in milliwatts (mW) at a distance d in meters (m):

$$P_r = P_t G_t G_r \left(\frac{\lambda}{4\pi d}\right)^2, \tag{1.1}$$

where P_t is the transmitted power in mW, G_r and G_t are the receiver and transmitter antennas gain in linear scale, respectively, and λ is the carrier wavelength in m. Since the free-space path loss (FSPL) is the reciprocal of gain and if we isolate the term that pertains to the channel itself, we obtain,

$$\text{FSPL} = \left(\frac{4\pi d}{\lambda}\right)^2. \tag{1.2}$$

By substituting $\left(\frac{c}{f}\right)$ for λ, we can express this as,

$$\text{FSPL} = \left(\frac{4\pi df}{c}\right)^2. \tag{1.3}$$

Then, expressing FSPL in terms of dB we have,

$$\mathrm{FSPL(dB)} = 20\log_{10}\left(\frac{4\pi df}{c}\right). \quad (1.4)$$

From (1.4), FSPL increases quadratically with the frequency, FSPL $\propto f^2$. For example, increasing the frequency *f* from 3 to 30 GHz will correspondingly add a power loss of 20 dB for any given transmitter-receiver distance. So, one major challenge of mmWave links is the large propagation loss, which limits the wireless communication link length. For example, the free space path loss of a 75-meter link at 30 GHz can easily exceed 100 dB, which makes communication above this distance extremely challenging.

While free space loss alone is often used in link budget calculations, it is important to understand that in this context, the term "free space" is meant literally; no atmosphere and no reflective surfaces or obstructions of any type. This does not represent a realistic environment for many path scenarios; hence the use of free space loss alone will not result in a realistic link budget. In this work we used three measurement-based large-scale path loss models, explained in chapter three, which provide realistic insight into propagation characteristics of the wireless channel. These are the close-in free space reference distance (CI) model, close-in free space reference distance with cross-polarization discrimination (XPD) factor model (CIX), and the floating intercept (FI) model. Equation (1.1) is often re-written in log-scale:

$$P_r(d)[\mathrm{dBm}] = P_t[\mathrm{dBm}] + G_t[\mathrm{dBi}] + G_r[\mathrm{dBi}] + 20\log_{10}\left(\frac{4\pi df}{c}\right). \quad (1.5)$$

Regardless of the use of directional or omnidirectional antennas, received power in realistic terrestrial conditions (non-free space channels) can be calculated as a function of the measured path loss:

$$P_r(d)[\mathrm{dBm}] = P_t[\mathrm{dBm}] + G_t + G_r - \mathrm{PL}(d)[\mathrm{dB}]. \quad (1.6)$$

2. BLOCKAGE ATTENUATION

Microwave signals are less vulnerable to blockages than are mmWave signals, and in addition incur smaller diffraction losses. Since the mmWave signal propagation incurs much larger diffraction losses than the microwave signals [7], mmWave signals are much more susceptible to blockages. This will result in a nearly bimodal channel loss characteristic according to the lack and existence of LOS.

Equation (1.1) shows that, with an increase in the transmitter and receiver distance the path loss at a specific frequency increases by 20 dB/decade under LOS propagation. In contrast, in some cases (e.g., large-distance, 2-ray conditions) the received power can decrease by 40 dB/decade, plus by an added blocking loss of 15-40 dB for NLOS [7]. Thus, the wireless connection could shift from being usable to unusable based on the presence of blockages. This will result in a large-scale drawback that cannot be bypassed with small scale diversity techniques.

Building penetration loss has been measured at multiple frequencies up to 6 GHz [8] and more recently at mmWave frequencies of 28, 38 and 73 GHz. Although penetration loss measurements showed significant spread, the trend is for loss to be at the level of 10 dB at UHF, rising to around 15 dB at 1800 MHz and around 20 dB at 5 GHz, and rising further to between 20-40 dB at 28 GHz and higher. The high penetration loss makes mmWaves depend mainly on reflections to propagate around obstacles. A corollary of high penetration loss is that, since indoor and outdoor systems may be so well isolated (high outdoor to indoor losses), in order to cover the user population indoors, additional indoor base stations may be used. Also, since about 80% of mobile use is indoor [9], some spectrum for indoor operation may also be needed. This might be the same spectrum as

outdoor systems, but this could depend on propagation and penetration measurements being performed and analyzed. We did a penetration loss measurement for many common building materials at the specific cm/mmWaves frequencies (5 and 31 GHz) to quantify this blockage effect.

3. VEGETATION ATTENUATION

Vegetation is an inherit component of most outdoor environments, and its effect on radio propagation has been investigated for decades. Foliage attenuation is a function of carrier frequency. In comparison to the traditional frequencies (below 6 GHz) used in cellular systems, foliage-induced attenuation increases at cm-wave (3-30 GHz) and mm-wave (30-300 GHz) frequencies. The reason is that at smaller wavelengths, obstacles of a given size, such as a tree trunk or a leaf, cause higher blockage of the Fresnel clearance zone [10] and the size of densely packed vegetation components becomes larger or comparable to the wavelength, and this induces multiple scattering effects that reduce signal power through the obstruction.

There are many factors that should be considered in evaluating vegetation attenuation, such as tree density, height, mean trunk diameter, etc. Near-field multiple scattering, which occurs within a dense leaf cluster, influences the value of forward scattering amplitude, and this determines the attenuation of signal propagating through the foliage [10].

From the electromagnetic wave propagation point of view, all obstacles with a size comparable to the wavelength are important. In the case of a shrub, leaves or needles can have a size comparable to the wavelength. Shrubs have leaves and trunks of size comparable to the mmWave signal wavelength, and this makes this type of vegetation a

particularly significant mmWave signal attenuator. In many popular kinds of shrubs, the distance between each pair of needles or leaves can be as small as 4 mm, less than half a wavelength at 31 GHz, and the needle/leaf length can vary from 1 to 10 cm, which is much larger than a wavelength. In this case multiple scattering among these shrub components may be significant.

Usually, foliage attenuation is quantified as excess loss in addition to the free space path loss, divided by the total length of the path traveled by the radio signal inside the vegetation area. Typically, this is expressed as the specific attenuation, with units of dB/m. In this work (chapter four), based on a ground truth measurement for several different kinds of shrubs, the path-loss measurement and specific attenuation of several shrubs has been calculated.

4. HARDWARE IMPAIRMENTS

For practical system designs of mmWave access at high frequencies up to 300 GHz, hardware impairments such as phase noise (PN), non-linear power amplifiers (NPA), IQ imbalance and analog-to-digital converter (ADC) imperfections must be considered very carefully for realistic performance evaluations.

From the RF design perspective, choosing the right transmission techniques could mitigate the effects of such impairments. One example is that some modulation schemes are well known for their robustness against hardware impairments. Frequency Shift Keying (FSK) is one example that is robust to nonlinear amplification. As operating frequencies increase, the power output of amplifiers is a growing challenge. Oscillator stability is a further challenge at millimeter wavebands, and this can drive a preference for single carrier

operation (rather than multicarrier schemes such as OFDM) so choosing the appropriate physical channel transmission scheme is another design choice.

1.2 STATISTICAL mmWAVE CHANNEL MODELS

For the new 5G systems to operate in bands above 6 GHz, there is a need for accurate radio propagation models for these higher frequencies. Previous generations of channel models were designed and evaluated for operation at frequencies only as high as approximately 6 GHz. For the development of new 5G systems to operate in bands up to 100 GHz, there is a need for accurate radio propagation models at these bands.

There are many existing and ongoing campaign efforts world-wide targeting 5G channel measurements and modeling. They include METIS2020 [83], NIST 5G mmWave Channel Model Alliance [84], MiWEBA [85], mmMagic [86], and NYU WIRELESS [87]. METIS2020, for instance, has focused on 5G technologies and has contributed extensive studies in terms of channel modeling over a wide range of frequency bands (up to 86 GHz), very large bandwidths (hundreds of MHz), and three-dimensional polarization modelling, spherical wave modelling, and high spatial resolution. The METIS channel models consist of a map-based model, stochastic model, and a hybrid model which can meet requirements of flexibility and scalability.

The COST2100 channel model is a geometry-based stochastic channel model (GSCM) that can reproduce the stochastic properties of multiple-input/multiple output (MIMO) channels over time, frequency, and space. The NIST 5G mmWave Channel Model Alliance is a newly established organization that is working to provide guidelines for measurement calibration and methodology, modeling methodology, as well as

parameterization in various environments. They are also establishing a database for channel measurement campaign results.

NYU WIRELESS has conducted and published extensive urban propagation measurements at 28, 38, and 73 GHz for both outdoor and indoor channels, and has created large-scale and small-scale channel models, including the concepts of time cluster spatial lobes (TCSL) to model multiple multipath time clusters that are seen to arrive in particular directions [11]–[15]. Data and models at these frequencies combined with the availability of spectrum world-wide makes these three frequencies a good starting point for mmWave prototyping [15].

The collected data of Rappaport's NYU measurements were the statistics that led to his 3-D mmWave channel model named "NYUSIM". NYUSIM is based on the existing 3GPP 3-D channel model but with extensions to cater for additional 5G modeling requirements and scenarios [16]. The simulator is applicable for a wide range of carrier frequencies: 500 MHz to 100 GHz. The supported radio frequency (RF) bandwidth is from 0 to 800 MHz. The supported operating scenarios are urban microcell, urban macrocell, and rural microcell. The models also incorporate multiple-input multiple-output (MIMO) antenna arrays at the transmitter and receiver.

NYUSIM can be used to generate realistic temporal and spatial channel responses. NYUSIM is built upon the statistical spatial channel model for broadband mmWave wireless communication systems. NYUSIM provides an accurate rendering of actual channel impulse responses in both time and space, as well as realistic signal levels that were measured. In this work, we tested our candidate mmWave candidate modulation

scheme, FSK modulation for different modulation orders, over NYUSIM mmWave channel models.

1.3 5G EXPECTED APPLICATIONS

To develop technology specifications, it is important to imagine envisioned 5G use cases, or scenarios. Mainly 5G use scenarios are going to be one of the three distinctive classes: first, the enhanced mobile broadband (eMBB), which corresponds to a straightforward evolution of the mobile broadband services of today, enabling enhanced user experience primarily via larger data rates. Second is the ultra-reliable and low-low-latency communication (URLLC); these types of services require very low latency and extremely high reliability. Third is the massive machine-type communication (mMTC), which corresponds to services that are characterized by a very large number of devices, like remote sensors, actuators, factory automation, and monitoring of various equipment [16].

Key requirements for mMTC services include very low device cost and very low device energy consumption, allowing for very long device battery life of up to at least several years. Typically, each device consumes and generates only a relatively small amount of data, that is, support for high data rates is not important. The mMTC services will provide wireless connectivity to tens of billions of often low-complexity low-power machine-type devices. Contrary to eMBB, where peak data rates are prioritized, here the accent is on scalable connectivity for an increasing number of devices, wide area coverage and deep indoor penetration. A typical example of mMTC is the collection of the measurements from a large number of sensors, such as smart metering [16].

On the other hand, mMTC is about providing adequate wireless links for network services with rather stringent requirements on availability, latency and reliability. For the concept of mMTC, two important examples are Vehicle-to-X (V2X) communications and industrial control applications.

Standard literature assumptions for mMTC are low complexity and battery constrained (low energy) devices [18]. Many mMTC devices will be limited by their battery due to cost/space constraints, and should preferably use low cost amplifiers; therefore, energy efficiency of mMTC terminals and good coverage are more important than spectral efficiency.

NC-FSK as a constant envelope waveform could be a good choice for mMTC devices because it offers the possibility to use a non-linear cost-effective and power-efficient High-Power Amplifier (HPA) at the transmitter, because the HPA can be operated close to saturation without the need for low distortion. For this reason, constant envelope coded-modulation systems have traditionally been extensively used in, e.g., satellite links, early wireless standards (GSM), Bluetooth, and low rate long distance microwave radio links for cellular backhauling.

The new schemes that are needed for mMTC devices must support their sporadic access. In order to reduce the power consumption, especially for mMTC, low-power devices need to transmit their data immediately after waking up with very low overhead and enter a dormant state directly after data transmission. As devices cannot be fully synchronized in this scenario, the 5G mMTC waveform needs to be robust against timing and frequency offset to limit the amount of required signaling. Given these requirements,

we again suggest NC-FSK as a potential modulation that could fit with mMTC applications.

1.4 DISSERTATION OBJECTIVES

In this section, a list of the dissertation objectives is presented.

1. Conduct outdoor and indoor propagation measurements for LOS and NLOS scenarios at different antenna polarization to analyze the environment and polarization effect on the signal propagation in the 30 GHz band.
2. Develop different path loss models for the collected empirical path loss measurements and recommend the best model that represents the measurements.
3. Measure vegetation attenuation at 30 GHz band for different kind of shrubs and analyze the depolarization effect of these species at this particular frequency band.
4. Repeat the vegetation attenuation measurements at different measurement geometry to analyze the effect of the measurement setup on the attenuation results.
5. Simulate the performance of NC-FSK at different system settings, e.g., different modulation order and different symbol time over a wideband mmWave channel.
6. Summarizes the dissertation conclusions and indicate some ideas for future work.

1.5 DISSERTATION CONTRIBUTIONS

This dissertation project "Performance Evaluation and Channel Modeling for Non-Coherent M-ary Frequency Shift Keying (NC-FSK) in the 30 GHz Millimeter Wave Band" started in 2014 and ended in 2019. We have some published several conference papers and

posters. In addition to this project, we also have a few papers focusing on the penetration loss for different materials at different cm/mmWave frequencies.

[C5] **M. Mohsen,** J. Liu and D. W. Matolak." Attenuation for Several Building Materials at 5, 30, and 90 GHz" to be submitted to Wamicon 2020.

[P3] **M. Mohsen,** D. W. Matolak and J. Liu." Example Attenuations for common Materials at 90 GHz" Poster, *6th NSF Millimeter-Wave RCN Workshop*, Boulder, CO, 23-24 Jul. 2019.

[C4] J. Liu, D. W. Matolak and **M. Mohsen**," Path Loss Modeling and Ray-tracing Verification for 5/31/90 GHz Indoor Channels," *IEEE 90th Vehicular Technology Conference*, Honolulu, HI, 22-25 Sep. 2019.

[C3] D. W. Matolak, **M. Mohsen** and J. Chen. "Path Loss at 5 GHz and 31 GHz for Two Distinct Indoor Airport Settings," *Proc. European Signal Processing Conference (EUSIPCO)*, Coruña, Spain, 2-6 Sep. 2019.

[P2] **M. Mohsen**, A. Grant, and D. W. Matolak. "30 GHz Path Loss Measurement and Modeling for Airport Surface Areas," Poster, *5th NSF Millimeter-Wave RCN Workshop*, Raleigh, NC, 28-29 Jan. 2019.

[C2] **M. Mohsen** and D. W. Matolak "Vegetation Attenuation for Several Evergreen Shrubs at 31 and 5 GHz," *11th Global Symposium on Millimeter Waves (GSMM)*, Boulder, CO, 22-24 May 2018.

[C1] **M. Mohsen** and D. W. Matolak, "31 GHz path loss measurement and modeling for indoor/outdoor environments," *IEEE Wireless Telecommunications Symposium (WTS)*, Phoenix, AZ, 18-20 Apr. 2018.

[P1] **M. Mohsen** and D. W. Matolak, "31 GHz Vegetation Attenuation for Several Evergreen Shrubs," Poster, *3rd NSF Millimeter-Wave RCN Workshop*, Tucson, AZ, 18-19 Jan. 2018.

CHAPTER 2

LITERATURE REVIEW

2.1 5G CANDIDATE MODULATIONS

The 5G mobile communication systems aim to support a large variety of services with different and often divergent requirements, and this has posed significant challenges to the design of 5G systems. Modulation and waveforms are one of the key physical layer choices that determine the system throughput, reliability, and complexity, therefore their design is critical in meeting the variety of requirements of 5G services. Many research overviews have been presented on the modulation and waveforms considered for potential applications in 5G. These sources identify design requirements and discuss the advantages of modulations to meet such requirements.

3GPP long term evolution (LTE) has embraced orthogonal frequency division multiplexing access (OFDMA) for downlink transmission and SC-FDMA (single carrier frequency division multiple access) for uplink transmission. This is to ameliorate the disadvantages with conventional OFDMA, which has high peak to average power ratio (PAPR). High PAPR means that expensive and less efficient power amplifiers with high requirements on linearity must be used. This increases terminal cost and shortens battery life. SC-FDMA signal has lower PAPR because of its innate single carrier structure [29]. Within LTE OFDM and SC-FDMA signal formats a variety of modulation formats are used, including PSK and QAM. Higher order modulation is used to achieve the higher data rates, the modulation order being determined by the signal quality.

Three candidate modulations for 5G, FBMC-OQAM, GFDM-OQAM, and WCP-COQAM have been analyzed in [19]. This research is focused on 5G in cognitive radio based industrial wireless communications. According to the ultra-reliability and low-latency requirements of industrial communications, the authors simulated the aforementioned modulations in low-band transmissions (carrier frequencies below 6 GHz and a bandwidth smaller than 100 MHz) through large indoor spaces and severe multipath channels that emulate industrial halls. They describe the suitability of these 5G multicarrier modulation (MCM) scheme candidates for industrial wireless communications.

The authors of [21] investigated frequency quadrature amplitude modulation (FQAM) which is a combination of frequency shift keying (FSK) and quadrature amplitude modulation (QAM). The authors made a performance comparison between FQAM and QAM via simulation in terms of BER a multi-cell OFDM network with additive Gaussian noise. The results showed that the FQAM system reduced the ICI at the cell edge and therefore achieved a higher transmission rate. FQAM outperformed quadrature amplitude modulation (QAM) in BER and it achieved a better SINR. Furthermore, FQAM is a better choice for communicating in a wireless channel with better efficiency and optimum bandwidth [21].

In [22], the authors showed that the performance of QAM combined with the novel Orthogonal Time Frequency Space (OTFS) modulation could perform well and compensate for the Doppler frequency due to high-speed mobility. OTFS spreads the signals in the time-frequency plane to obtain a superior diversity and higher flexibility in pilot design. The OTFS modulation is a novel family of modulation schemes based on multiplexing the QAM information symbols over localized pulses in the delay-Doppler

signal representation, instead of as in the conventional time-frequency plane. Hence OTFS can be viewed as a special type of a time-frequency spreading technique, where each QAM symbol is carried by a two-dimensional basis function spread over the full time-frequency grid. The OTFS waveforms showed a good performance for the time-frequency selective channel where all received QAM symbols experience the same localized impairment and all the delay-Doppler diversity branches are coherently combined. OTFS-MIMO systems can transmit data streams from each antenna without the communication performance degradation even in high Doppler frequency environments, where such a scheme is best suited.

2.2 PATH LOSS MEASUREMENTS AND MODELING AT mmWAVE BANDS

As noted, due to differences as a function of frequency, the current propagation models used for frequency bands less than 6 GHz are not appropriate and cannot be applied for path loss modeling and channel characteristics for millimeter wave (mmWave) bands. Thus, extensive studies on channel characterization and path loss modeling are required to develop general and appropriate channel models that can be suitable for a wide range of mmWave frequency bands.

Reference [23] presents and compares two candidate large-scale propagation path loss models, the alpha-beta-gamma (ABG) model and the close-in (CI) free space reference distance model, for the design of fifth generation (5G) wireless communication systems in urban micro- and macro-cellular outdoor scenarios. Comparisons are made using the data obtained from 20 propagation measurement campaigns or ray-tracing studies from 2 GHz to 73.5 GHz over distances ranging from 5 m to 1429 m. The results show that the one-parameter CI model has a very similar goodness of fit (i.e., the shadow fading standard

deviation) in both line-of-sight and non-line-of-sight environments, while offering substantial simplicity and more stable behavior across frequencies and distances, as compared to the three-parameter ABG model. Additionally, the CI model needs only one very subtle and simple modification to the existing 3GPP floating-intercept path loss model (replacing a constant with a close-in free space reference value) in order to provide greater simulation accuracy, simplicity, better repeatability across experiments, and higher stability across a wide range of frequencies.

Measurements at 28 GHz and 38 GHz were conducted by the authors of [24] in urban microcellular environments. Measurements were made in both LOS and NLOS scenarios at different transmit antenna heights. Based on the measured data, the authors presented 5G-suitable path loss models. Path loss was expressed in easy-to-use formulas as the sum of a distant dependent path loss factor, a floating intercept, and a shadowing factor; as with most log-distance models, this model also minimizes the mean square error fit to the empirical data. A comparison between CI and FI path loss models was made and the authors illustrated the differences of the two modeling approaches. They showed that a floating intercept model reduces the shadow factors by several dB and offers smaller path loss exponents.

Reference [25] presents a study of CI, FI, and ABG models for an indoor environment in the 4.5, 28, and 38 GHz frequency bands. Measurements for the indoor LOS and NLOS scenarios were taken every meter over a separation distance of 23 m between the Tx and Rx antenna locations. Results show that the large-scale path loss over distance could be modeled better by using the simple proposed model with one parameter path loss exponent PLE (n). This PLE can be physically related to the transmitter power.

The PLE values for the LOS scenario were 0.92, 0.90, and 1.07 for the V-V, V-H, and V-Omni antenna polarizations, respectively, at the 28 GHz frequency and were 2.30, 2.24, and 2.40 for the V-V, V-H, and V-Omni antenna polarizations, respectively, at the 38 GHz frequency.

The FI model can obscure the physical effects of path loss with distance, since the intercept can vary significantly with environment, without any clear connection to propagation physics. Therefore, the FI model may not be the best to physically represent the channel, particularly for NLOS environments. The multifrequency ABG path loss model [30] showed all frequency slope values in LOS and NLOS environments represented an unrealistic amount of attenuation with increasing frequency. Also, the small difference in standard deviation across Tx-Rx separation distances suggests that the simpler, physically-based CI model could be more suitable for closed-form analysis than the FI and ABG models.

2.3 VEGETATION ATTENUATION AT mmWAVE

In [26], several measurements were reported to determine the extent of attenuation of mmWave signals when propagated through vegetation. This work discussed existing methods for predicting vegetation attenuation that are either deterministic—which are complex to implement—or are completely empirical and take no account of measurement geometry. The author presented a new semi-empirical model that is based on measurements of vegetation attenuation, taking into account the measurement geometry. Further indoor measurements were made in this work through three kinds of deciduous trees. The results of the measurements show the variability of the attenuation through the vegetation to be about 20 dB/m for the in-leaf tree and 7 dB/m for the out-of-leaf, for the frequency of 20

GHz. This is due to the random nature of the position of branches and leaves, since at millimetric frequencies the signal behaves almost optically, with the extent of attenuation corresponding to the alignment of leaves. When compared with the measured results, the prediction given by the proposed model underestimates the attenuation. However, this is not unexpected as the young plants used for the indoor measurements were generally of denser foliage than is found in outdoor settings. Furthermore, the geometry of the indoor measurement was quite different from that of the outdoor measurements on which the model was based.

In [27] propagation measurements were made to examine millimeter-wave signal propagation through conifer vegetation. Linearly polarized continuous-wave signals at 9.6, 28.8, 57.6. and 96.1 GHz were used to evaluate attenuation, depolarization, and backscattering from coniferous trees. Azimuth and elevation scans were conducted for various transmitter heights and path lengths. Results from the measurements were presented and compared with data gathered from similar measurements taken through deciduous vegetation. Vegetation loss for the first 30 meters of foliage depth increased in nearly linear at a rate of 1.3 to 2.0 dB per meter, depending on frequency, and beyond 30 meters, the loss curve decreased at an exponential rate that averaged only 0.05 dB loss per additional meter beyond 30 m. These results showed a clear trend for increased losses with increased frequency but not in a directly proportional relationship (higher frequencies were attenuated less than the ratio of the increase in frequency). These ratios of vegetation losses versus frequency appear to be related to how closely the wavelength of the propagated wave compares to the scale size of the leaves and branches obstructing the path.

Reference [28] presented 73 GHz wideband outdoor foliage and ground reflection measurements. Propagation measurements were made with a channel sounder, with rotatable horn antennas at both the transmitter and receiver, to study foliage-induced scattering and de-polarization effects, to assist in developing future wireless systems that will use adaptive array antennas. Signal attenuation through foliage was measured to be 0.4 dB/m for both co- and cross-polarized antenna configurations with an XPD of 25.4 dB when using a pair of 27 dBi horn antennas. The measured ground reflection coefficients ranged from 10.2 dB to 34 dB of reflection loss.

CHAPTER 3

LARGE-SCALE PATH LOSS MEASUREMENTS AND MODELING

The radio-link reliability strongly depends on propagation properties and, therefore, effective prediction tools and models are required in the design and planning phases of modern radio systems. Accordingly, an accurate and simple path loss model is critical for outdoor and indoor environments where deployment is likely to occur. We have conducted measurement campaigns at 31 GHz in outdoor and indoor settings of a typical office building, Swearingen Engineering Center, in Columbia, South Carolina. The acquired measurement results provide data that allowed us to develop large-scale path loss models for an outdoor environment around the building and in its courtyard, and for indoor environments for different floors, both for line-of-sight (LOS) and non-line-of-sight (NLOS) conditions.

Close-in (CI) free space reference distance, close-in free space reference distance with cross-polarization discrimination (XPD) factor model (CIX), and the floating intercept (FI) single-frequency directional large-scale path loss models [41], [42] were developed based on the acquired data. With determination of each model's parameters via a linear regression of the experimental data, standard deviations in these three models in both LOS and NLOS scenarios allow direct comparisons of model goodness of fit. Based on the resulting path loss model parameters, we provide some insight into the propagation mechanisms such as reflection and waveguiding at this particular mmWave frequency.

3.1 BACKGROUND THEORY

Large-Scale Path Loss Models

To characterize our radio-propagation environments at 31 GHz, we used three measurement–based large-scale path loss models that provide insight into propagation characteristics of the wireless channel. These are the close-in (CI) free space reference distance model, close-in free space reference distance with cross-polarization discrimination (XPD) factor model (CIX), and the floating intercept (FI) model. The CI model can be used for LOS and NLOS environments for co- and cross-polarization antenna configurations. The path loss exponent (PLE) values represent the rate of increase of attenuation with logarithm of distance.

- Floating intercept (FI) model

The floating-intercept (FI) path loss model of (3.1) [31] has three parameters: α represents the floating-intercept in dB, β is the slope of the line, and σ is the standard deviation of the linear fit line. Neither α nor β necessarily have any physical basis but are simply the result of a linear fit of path loss in dB to the logarithm of distance. The FI model equation is as follows:

$$\mathrm{PL}^{\mathrm{FI}}(\mathrm{d})[\mathrm{dB}] = \alpha + 10 \cdot \beta \log_{10}(\mathrm{d}) + \mathrm{X}_{\sigma}^{\mathrm{FI}}. \quad (3.1)$$

Shadowing is represented by the zero-mean (usually assumed Gaussian) random variable $\mathrm{X}_{\sigma}^{\mathrm{FI}}$ with standard deviation of σ dB.

The path loss at each measurement point is calculated from the measured received signal power using the link budget (3.2).

$$\mathrm{PL} = \mathrm{P}_{\mathrm{Tx}} + \mathrm{G}_{\mathrm{Tx}} + \mathrm{G}_{\mathrm{Rx}} - \mathrm{P}_{\mathrm{Rx}} - \mathrm{L}_{\mathrm{C}} \quad (3.2)$$

where P_{TX} and P_{RX} are the transmitted and the received power in dBm, G_{TX} and G_{TX} are the gains of the transmitter and receiver antennas in dBi, PL and L_C are the path loss and cable loss, respectively, in dB.

- Close-in free space reference distance (CI) model

The CI model is implemented in 3GPP models by making a subtle modification to the FI model, by replacing a floating (non-physically based) intercept constant with a frequency-dependent constant that represents free space path loss in the first meter of propagation [33]. In the past, models in the ultra-high frequency (UHF) and microwave bands used a close-in reference distance of 1 km or 100 meters [34], since base station towers were tall without any nearby obstructions, and cells size were on the order of many kilometers. In mmWave CI models, typically d_0 = 1 meter since base stations will be at lower heights or mounted indoors, and closer to obstructions [34], and link distances will be shorter, up to a few hundred meters. The CI 1 meter reference distance is a conveniently suggested standard that ties the true transmitted power or path loss to a convenient close-in distance of 1 m, as suggested in [31].

The CI path loss model is found by determining the PLE (n) by the least-squares approach that fits the measured data with smallest error but using a real physical "anchor point" (the CI intercept). This intercept is the free space path loss when the separation distance between Tx and Rx is d_0. The CI model is

$$PL^{CI}(d)[dB] = FSPL(d_0) + 10n\log_{10}\left(\frac{d}{d_0}\right) + X_{\sigma}^{CI}, \quad (3.3)$$

where $d_0 = 1\ \text{m},\ d \geq d_0$, and X_σ^{CI} is a zero mean (~Gaussian) random variable with σ the standard deviation in dB, and FSPL denotes free space path loss in dB, calculated using (3.4),

$$\text{FSPL}(d) = 20\log_{10}\left(\frac{4\pi df}{c}\right), \tag{3.4}$$

where f=frequency and c=speed of light in free space.

It is noteworthy that the FI model is identical to the CI model if we equate β in the FI model in (3.1) with the PLE *n* in the CI model in (3.3) and set α in (3.1) to be the free space PL at 1 meter. In our study we focused more on the CI path loss model for the following reasons:

- Unlike the FI model, CI model is physically tied a close-in free space reference and standardizes all measurements around a 1 meter free space reference distance. So, the CI model offers simplicity by reducing the number of empirical parameters.
- The CI model provides a more conservative NLOS path loss estimate at large distances, whereas the FI model predicts smaller path loss close to the transmitter and more loss at greater distances [35].
- Standardizing to a reference distance of 1 meter makes comparisons of measurements and models simpler, and provides a standard definition for the PLE, while enabling intuitive and rapid computation of path loss.
- The CI model also has a useful "companion" model: the close-in free space reference distance with cross-polarization discrimination (XPD) factor model.

For the cross-polarization propagation models, the CIX model has been used in [31], [36]. This model has an added constant attenuation factor called the cross-polarization discrimination factor (XPD), which is a function of the antennas. The equation for this model is given by (3.5). The CIX model uses the PLE found from the *co*-polarized measurement for the same reference distance using (3.3) and adds the XPD. Thus, the CIX path loss model for the vertical transmit and horizontal receive (V-H) configuration is the same as the CI path loss for vertical transmit and vertical receive (V-V) model, but with intercept shifted up by the value of XPD:

$$\mathrm{PL}^{\mathrm{CIX}}(\mathrm{d}) = \mathrm{FSPL}(\mathrm{d_0}) + 10\mathrm{n_{V-V}}\log_{10}\left(\frac{\mathrm{d}}{\mathrm{d_0}}\right) + \mathrm{XPD} + \mathrm{X}_{\sigma}^{\mathrm{CIX}}. \tag{3.5}$$

In this model, n is the co-polarization path loss exponent and $\mathrm{X}_{\sigma}^{\mathrm{CIX}}$ is another zero-mean Gaussian (in dB) random variable with standard deviation σ_{CIX}, distinct from the co-polarized value of standard deviation.

The new approach proposed in [32] has been used to simplify the CIX model to avoid the computational complexity of the often-used MMSE approach. The XPD factor can be calculated by averaging the difference between the co-polarization PL and cross-polarization PL over the distance [32].

$$\mathrm{XPD} = \sum_{\mathrm{i}=1}^{\mathrm{k}} \frac{|\mathrm{PL_{VV}}(\mathrm{d_i}) - \mathrm{PL_{VH}}(\mathrm{d_i})|}{\mathrm{k}} \tag{3.6}$$

where $\mathrm{PL_{VV}}$ and $\mathrm{PL_{VH}}$ represent the co- and cross-polarization path losses in dB, respectively.

3.2 MEASUREMENT EQUIPMENT AND TEST CONFIGURATION

The measurement equipment block diagram is shown in Figure 3.1. A 5 GHz single tone IF signal generated by a vector signal generator (Keysight, model N5182A MXG) with a power level of -10 dBm entered the input to a custom-designed RF up-converter (Microwave Dynamics, model LO-MIX301-2832). The upconverter modulated the IF signal to produce an RF CW signal at a center frequency of 31 GHz. This mmWave signal then entered an amplifier (Microwave Dynamics, model AP2832-25) to yield an RF signal with output power of 25 dBm. This signal was transmitted by a 10 dBi gain horn antenna (Pasternack, model PE9850/2F-10), with 54.4° azimuth and elevation half power beam widths (HPBWs). At the receiver (Rx), the received signal was captured by an identical model horn antenna, whose output entered a mmWave signal and spectrum analyzer (Rohde & Schwarz, model FSW26/FSW43). The analyzer settings were center frequency 31 GHz, frequency span 1 MHz, and resolution bandwidth 1 kHz.

The transmitter Tx and Rx hardware were placed on a wheeled cart for ease of transportation and consistency of measurement antenna heights. The Tx and Rx antennas were mounted at heights of 1.5 and 1 meters, respectively. To maintain the boresight alignment between the antennas while moving along all our measurement points, a simple optical alignment was made using a laser pointer. A manual adjustment positioner was built to up-tilt and down-tilt the antennas on both Tx and Rx.

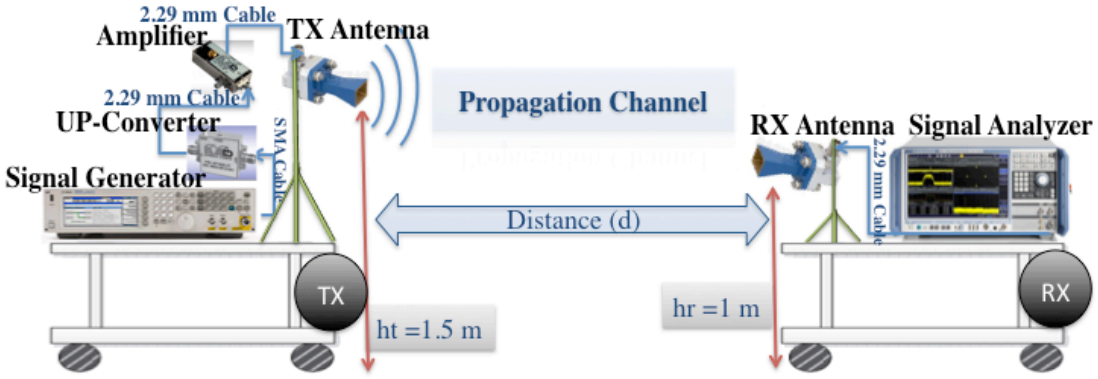

Figure 3.1 Transmitter and receiver block diagram.

3.2.1 Measurement Procedure

Millimeter-wave propagation measurements were conducted at 31 GHz for outdoor and indoor environments using directional antennas for both co-polarized and cross-polarized antenna configurations. The measurements were conducted in typical line-of-sight (LOS) and non-LOS (NLOS) environments inside and around a large building on the University of South Carolina campus. Several propagation PL models are presented based upon the measurements collected data.

Measurements were conducted both outside and inside Swearingen Engineering Center building on the University of South Carolina campus in downtown Columbia, South Carolina. Swearingen is a 4-story building. Each floor of this building contains typical offices or classrooms with common obstructions such as doors, desks, chairs and other office furniture. Our measurements covered a variety of different scenarios for both outdoor and indoor environments. Furthermore, measurements were conducted in an open interior courtyard to study the effect on path loss of the Tx and Rx antenna heights above the ground.

3.2.2 Several remarks on our measurements are worth pointing out:

(1) For averaging out small scale fading (due to multi-path components (MPCs) from reflections, diffraction, and scattering from the floor, nearby walls and other obstructions), we collected data to compute a spatial average at each measurement point. This consisted of three individual measurements separated by approximately one wavelength, all at the same link distance.

(2) Since future mmWave wireless systems are expected to be used not only for stationary devices but also with mobile devices with various physical orientations, all the measurements were done for both co- and cross-polarization antenna configurations. For co-polarization measurements, the Tx and Rx horn antennas were vertically polarized (V-V) whereas for the cross-polarization measurements, the Tx was vertically polarized, and the Rx antenna was horizontally polarized (V-H).

(3) The Tx and Rx antennas were aligned on boresight in the azimuth and elevation planes regardless of whether the environment was line of sight (LOS) or non-LOS (NLOS). Since the Tx antenna is higher than the Rx antenna, when the Rx was close to the Tx, the Rx antenna was uptilted for boresight alignment. For large Tx-Rx separation distances, the Rx antenna alignment was closer to the horizontal than at closer distances.

(4) Our measurement Tx-Rx separation distance range started at 1 meter, satisfying the far-field criterion, and ended at the farthest end of the corridor for the indoor measurements, or at the end of the freely available space for the outdoor

measurements. For all measurements, the received signals achieved a signal-to-noise ratio (SNR) ≥ 20 dB [2].

(5) We avoided doing our measurements during the rush hours to avoid pedestrian body blockage, so all listed LOS measurements results represent true LOS conditions.

(6) All path loss model parameters were found using routines developed using MATLAB 2016b/MathWorks® software. We followed the mathematical procedures for the closed-form solutions for minimum shadow fading (SF) standard deviation large-scale path loss model parameters for both close-in and floating intercept path loss models, from [7]. PL in close-in model represented by the best fit minimum mean square error (MMSE) PLE over all measurements from a particular measurement campaign. As we see in equation (3.3), shadowing effect represented by a zero mean Gaussian random variable (X_σ) with a standard deviation σ in dB, also known as the shadow factor, representing largescale signal fluctuations resulting from shadowing by large obstructions in the wireless channel.

3.3 OUTDOOR MEASUREMENTS

3.3.1 FRONT COURT MEASUREMENTS

Outdoor path loss measurements were conducted in the front court of the Swearingen building for a range of distances and for different polarization. The collected data is presented as path loss models shown in several following figures.

A. Environment Description

The outdoor measurement area was near the main entrance of Swearingen Center along the front courtyard; see Figure 3.2. The Tx remained fixed in position and the Rx equipment was moved on the cart at distance increments of 1 merter. The Tx area is open but backed by concrete walls and tinted glass doors and windows of the building itself; some shrubs and trees were near the path of the Rx cart. The ground is covered by concrete slabs.

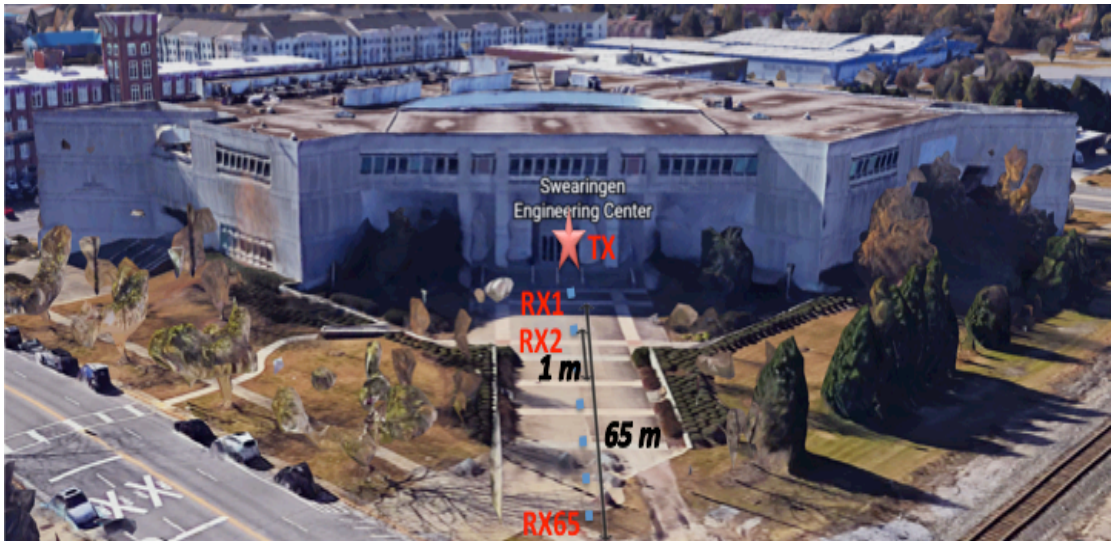

Figure 3.2 Google Earth ® view (2017) of actual outdoor measurement environment, Swearingen Engineering Center, 65 Tx-Rx measurement points.

B. Results

Figure 3.3 displays the directional path loss scatter plots and best fit CI, CIX and FI models in our outdoor LOS environment for co-polarized (V-V) and cross-polarized (V-H) antenna configurations. The measured V-V path losses are larger than FSPL for $10\log_{10}(d) \leq 12$ ($d \leq 15.8$ m), but at larger distances, the path losses are slightly less than free space. This may be attributable to some waveguiding effects. The walls and aluminum

tinted glass doors behind the transmitter and the smooth concrete floor as shown in Figure 3.2 likely produce significant reflections.

Table 3.1 shows the parameters for all the models. It can be seen that FI α values differ from the free space path loss at 1 meter: 65.68 dB compared to 62.27 dB FSPL. This is expected [31]. Furthermore, the FI slope values (β) of the least-squares fit line in (3.1) are less than free space (β=2) and the V-V slope is close to or less than the V-H slope. The CI co-polarized slope (1.95) is only slightly less than that of free space, as expected, whereas the CI cross-polarized slope (2.98) is larger than that of free space.

Table 3.1 CI, CIX, and FI PL model parameters for LOS outdoor at 31 GHz.

31 GHz Directional FI, CI and CIX Path Loss Models Parameters							
Pol.	**CI: d_0=1 m FSPL(1 m)=62.27dB**		**FI**			**CIX**	
	PLE	σ_{dB}	$\propto_{dB}$	β	σ_{dB}	**XPD**	σ
V-V	1.95	2.01	65.68	1.73	1.79	/	/
V-H	2.98	5.17	80.67	1.76	1.52	15.42	5

According to Table 3.1, for the FI model the V-V and V-H models have similar values of slope (β). The value of the floating-intercept (α) is almost 15 dB larger in the V-H case than in the V-V case. The two model lines are easily distinguishable, and this is expected since there is little in this outdoor LOS propagation environment to cause depolarization. The 31 GHz directional outdoor LOS V-H XPD factor was found to be approximately 15.42 dB, shown in Figure 3.3.

For directional measurements in LOS environments, the PLE is not frequency dependent [31]. Based on that fact we compared our PLE values with those from the

literature, where the PLE values were 1.7 and 4.1 for co- and cross- polarization, respectively, for 28 GHz [31]. This is in reasonable agreement with our results given the difference in the environments.

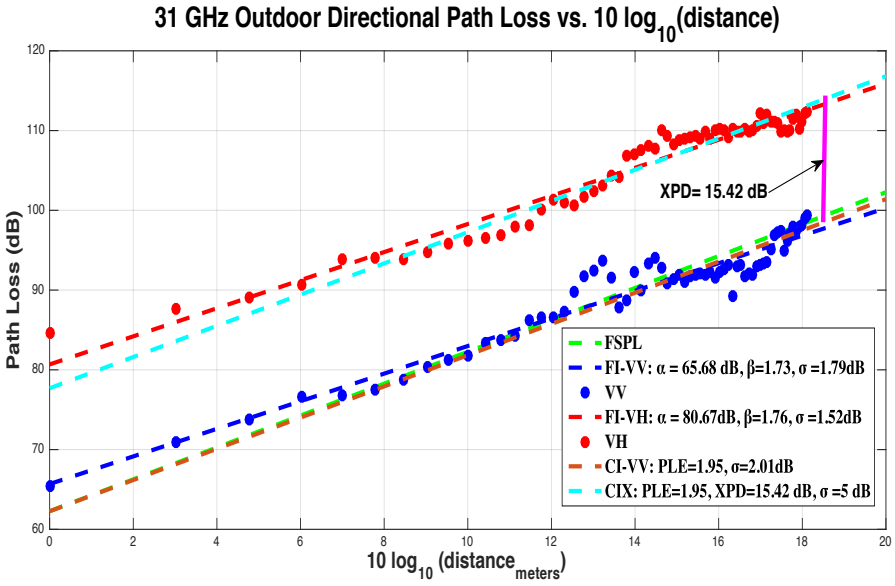

Figure 3.3 V-V and V-H measured PL scatter plots, CI, CIX and FI PL models vs. distance for 31 GHz outdoor LOS setting.

3.3.2 COURT YARD MEASUREMENTS

A. Environment Description

B. Measurements were conducted in an open interior courtyard to study the effect on path loss of the Tx and Rx antenna heights above the ground. Figure 3.4 shows the actual measurement environment for three different Tx antenna heights (1.5, 4.15, and 8.3 meters) for eight different Tx-Rx separation distances, in the interior courtyard of Swearingen Engineering Center. For the courtyard measurements, we followed the same Tx-Rx positioning scenario. The Tx location at each floor is open but backed by curved concrete walls and

tinted glass doors. Some shrubs and trees are in the courtyard and near the path of the Rx cart, and concrete slabs cover the courtyard ground.

Figure 3.4 Interior Courtyard, LOS measurement environment, Swearingen Engineering Center, 18-25 meters Tx-Rx separation distance.

C. Results

Figure 3.5 shows the CI path loss model of (3.1) for our multi-floor building courtyard LOS scenario. We observe a slight reduction in path loss as the antenna height decreases.

Table 3.2 shows that the PLE decreases very slightly from 2.13 to 2.06 as the Tx antenna height decreases from 8.3 m to 1.5 m. In [39] the authors conclude that lower base station heights provide better close-in coverage and this agrees with these courtyard results. The very small decrease in the PLE means that one need not use distinct models for the different heights in this particular setting. It would be of interest to see if such a trend continued for larger transmitter heights.

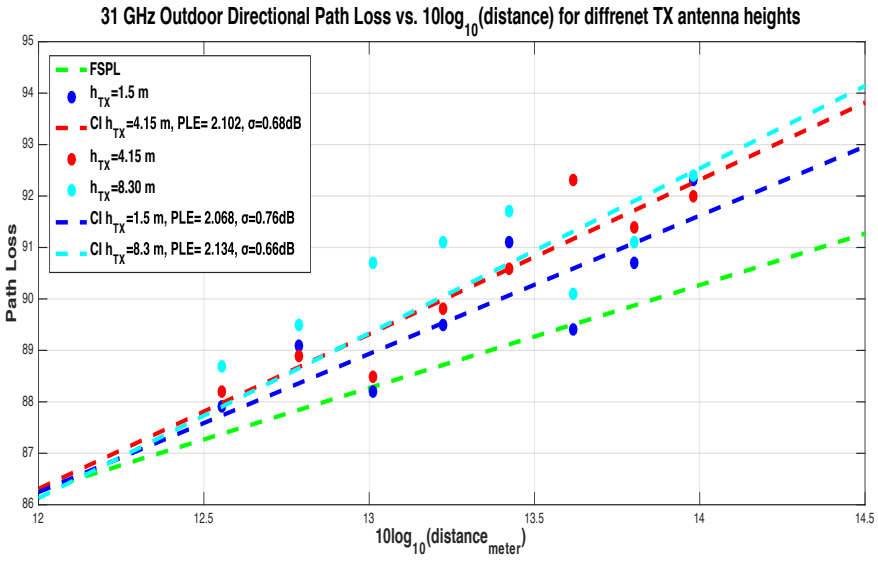

Figure 3.5 V-V Measured PL scatter plots, best fit CI PL models for 31 GHz in interior courtyard/Swearingen Center, LOS environment.

Table 3.2 CI PL model parameters for LOS interior courtyard at 31 GHz.

Tx Antenna Height (meters)	**CI: d_0=1 m FSPL (1 m) = 62.27 dB**	
	PLE	σ_{dB}
1.5	2.06	1.86
4.15	2.10	1.65
8.30	2.13	2.22

3.4 INDOOR MEASUREMENTS IN INTERIOR CORRIDORS

Indoor environments are significantly different from the outdoor in many ways. As a consequence, indoor path loss models will account for the variations in floor plans, construction materials used, type and number of obstructions like furniture, and people and their movements, etc. In addition, shadowing and multipath propagation from reflection, refraction, scattering, and penetration also impact the received signal characteristics.

We focused on a very important aspect of mmWave signal propagation indoors, which is the waveguide phenomenon in corridors. All of our indoor measurements were conducted along corridors in different floors for both LOS and NLOS scenarios with both co- and cross-polarization antenna configurations.

3.4.1 WAVEGUIDE LIKE STRUCTURES FOR FUTURE NETWORKS

Tunnels and "tunnel-like" constructions such as corridors are regarded in the literature as oversize dielectric waveguides [32], [36] and [40], with transversal dimensions much larger than wavelength, thus a number of modes are propagating. Waveguiding effect can make corridors a good propagation environment that can be used as a wireless communication channel for providing high-rate network access to offices where the transmitter antenna excites waveguide modes in the corridor. These modes propagate through the corridor experiencing multiple reflections from terminations and non-uniformities and are received by the receiver antenna. As in many multipath channels, the signal power at a receiving point is expressed as a sum of direct and reflected paths from the source.

The radio signal attenuation in waveguide-like constructions is usually much lower than in free space and decreases with increasing frequency. Hence such settings can present a "radio-friendly" medium for future 5^{th} generation communication systems [36].

Attenuation in the corridors is due to the finite conductivity of the corridor walls celling, floor, and losses at each reflection from non-uniformities in the corridor. The signal is attenuated as it interacts with the corridor walls, floor and ceiling, but the wave largely

propagates in the longitudinal direction inside the corridor and effects of wooden doors and losses due to roughness of sidewalls and tilt are typically small.

3.4.2 ENVIRONMENT DESCRIPTION

Figures 3.6-3.9 show the floor plans and photographs of the 1st, 2nd/wing A, 2nd/wing D, and 3rd floor corridors, respectively, where the indoor measurements were taken. All corridors walls are of two layers of plasterboard with air gap in between; the average thickness of these interior walls is 13 cm. These walls do not contain a metal stud layer. The width of the 2nd/wing "D" and 3rd floor corridors is 2.4 m, whereas the width of the 2nd/wing "A" floor corridor is 2.9 m, and the width of the 1st floor corridor is 4.2 m. The ceiling is gypsum board and the ceiling height of all corridors is 2.4 m, except for the first-floor corridor, which has height 3.4 m. The main difference between corridor construction features is the floors. The 2nd floor corridors have a floor of vinyl tiles (Figure 3.7 and 3.8) whereas the 3rd floor is covered by carpet (Figure 3.9) and the first floor is terracotta tile (Figure 3.6). Figure 3.6 shows the floor plan and photograph of Swearingen Center's main entrance hall, with corridors on both sides. Our LOS measurements for the first floor were along these corridors and the entrance hall, where one side was a glass wall of 1.1 m by 1 m transparent and aluminum-framed glass with thickness of 1 cm, and the other side was a plasterboard wall.

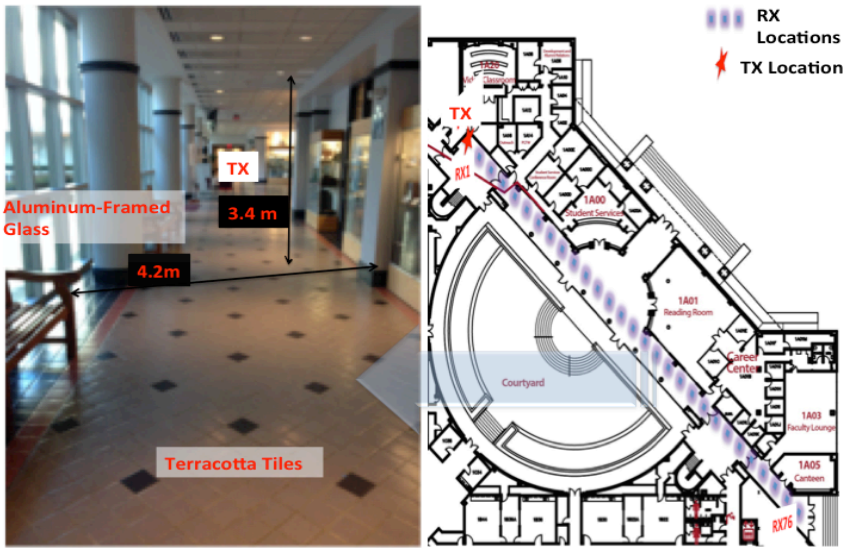

Figure 3.6 1st floor corridor photograph (left), and floor plan (right), 76 Tx-Rx measurement points.

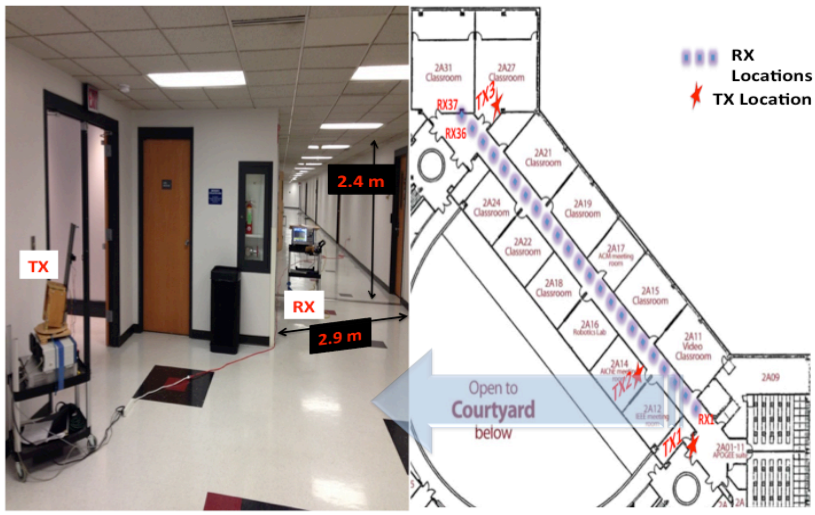

Figure 3.7 2nd floor / Wing (A) corridor photograph (left), and floor plan (right). NLOS scenario, 37 Tx-Rx measurement points.

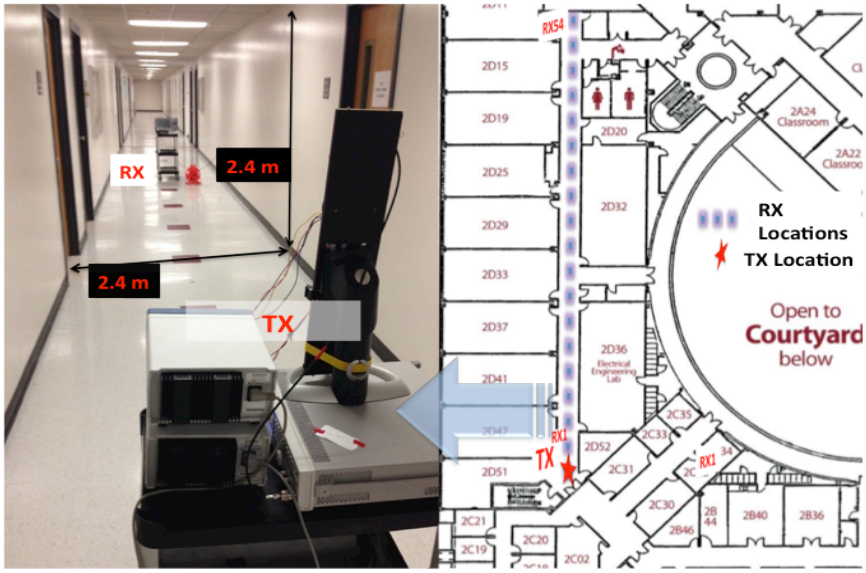

Figure 3.8 2nd floor / Wing (D) corridor photograph (left), and floor plan (right), 62 Tx-Rx measurement points.

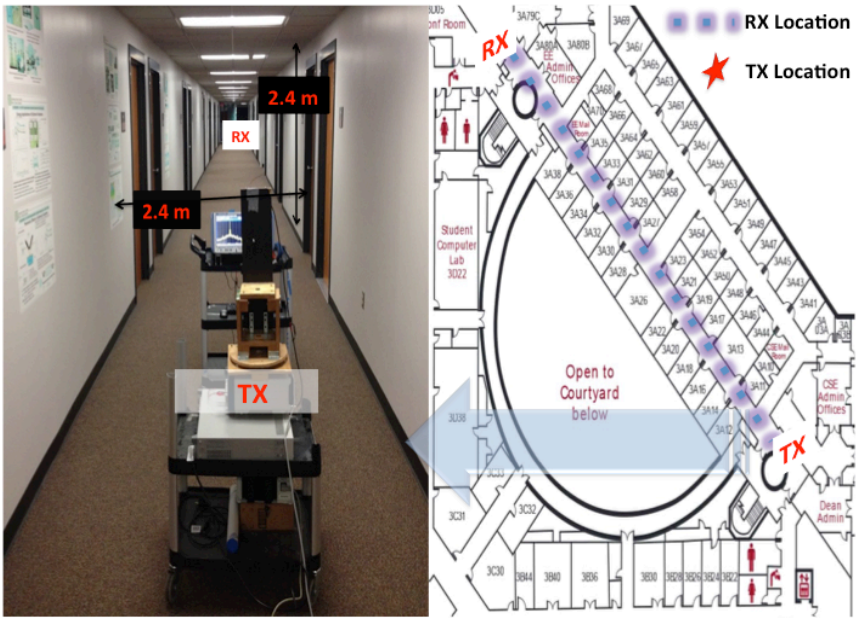

Figure 3.9 3rd floor corridor photograph (left), and floor plan (right), 58 Tx-Rx measurement points.

3.5 RESULTS

A. Interior Corridors / NLOS Scenario

The best-fit models for V-V and V-H configurations for the 2nd Floor Corridor / wing" A" NLOS scenarios are shown in Figure 3.10. The CI model has, as expected, PLEs larger than free space, 2.79 and 3.57, and the XPD factor is 11.17 dB. This indicates a significant de-polarization effect in our NLOS indoor environments since this value is less than that found for the LOS case.

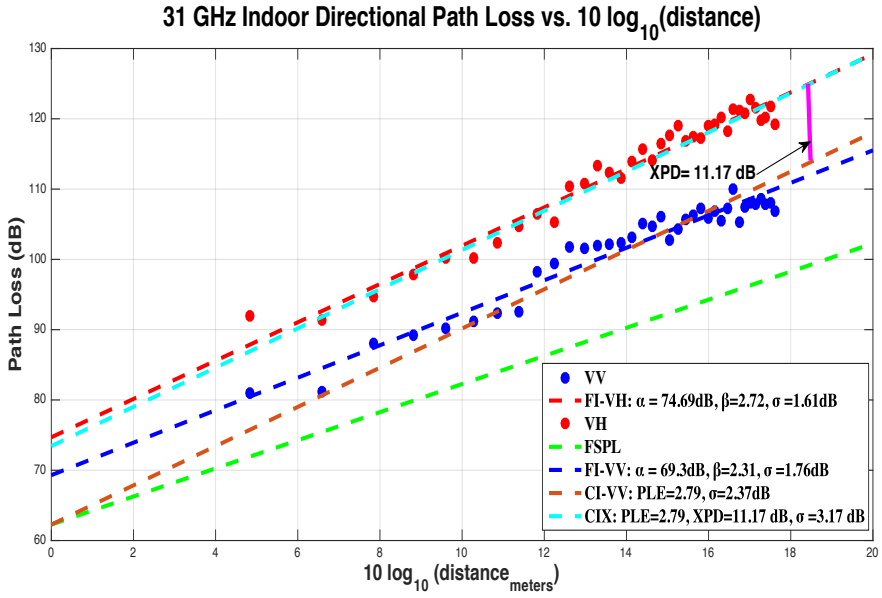

Figure 3.10 V-V and V-H measured PL scatter plots, best fit CI, CIX and FI PL models for 31 GHz in 2nd Floor/wing "A" corridor/Swearingen Center, NLOS Indoor environment.

Table 3.3 CI, CIX, and FI PL model parameters for NLOS 2nd Floor/Wing "A" Corridor at 31 GHz.

Pol.	CI: d_0=1 m		FI			CIX	
	PLE	σ_{dB}	α_{dB}	β	σ_{dB}	XPD	σ
V-V	2.79	3.37	69.30	2.31	2.76	/	/
V-H	3.57	4.23	74.69	2.72	2.81	11.17	3.17

Table 3.3 shows the CI, CIX and FI path loss model parameters for these NLOS scenarios.

B. Interior Corridors / LOS Scenario

Figures 3.11-3.13 display the LOS directional path loss scatter plots and best fit CI, CIX, and FI models in the 1st, 2nd/ wing"D," and 3rd floor corridors, respectively, for both co-polarized (V-V) and cross-polarized (V-H) antenna configurations. Table 3.4 shows the corresponding CI, CIX, and FI path loss model parameters for these three floors corridors, for the LOS environment.

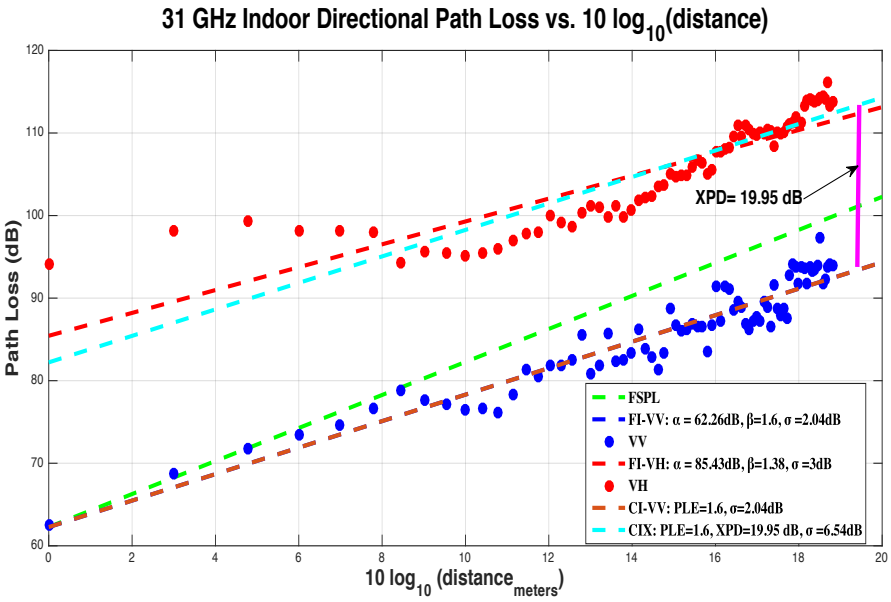

Figure 3.11 V-V and V-H Measured PL scatter plots, best fit CI, CIX and FI PL models for 31 GHz in 1st Floor corridor/Swearingen Center, LOS Indoor environment.

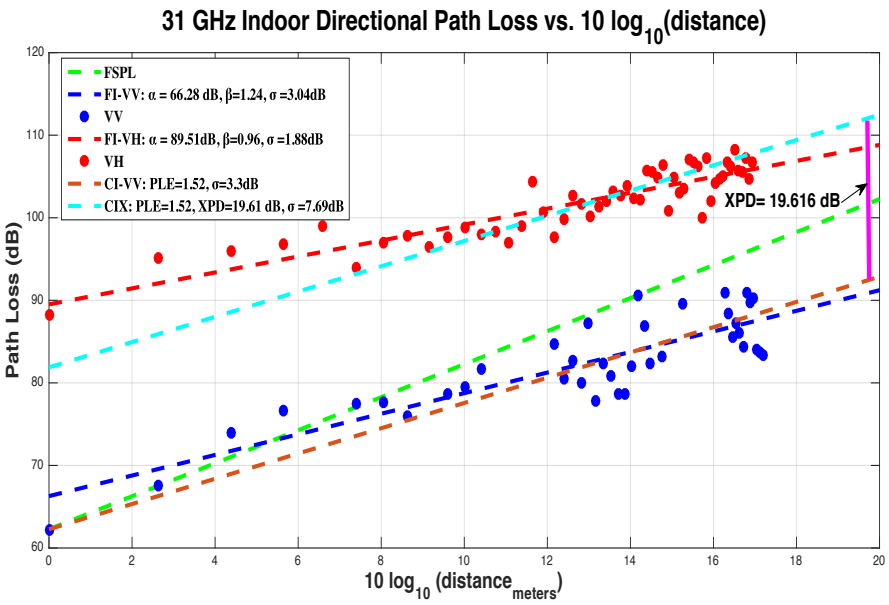

Figure 3.12 V-V and V-H Measured PL scatter plots, best fit CI, CIX, and FI PL models for 31 GHz in 2nd Floor/wing "D" corridor/Swearingen Center, LOS Indoor environment.

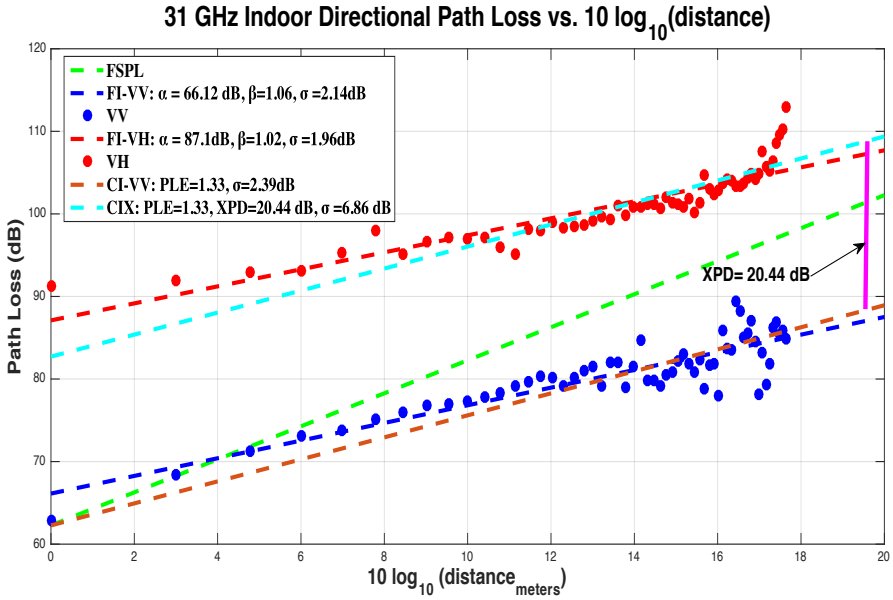

Figure 3.13 V-V and V-H Measured PL scatter plots, best fit CI, CIX, and FI PL models for 31 GHz in 3rd Floor corridor/Swearingen Center, LOS Indoor environment.

Table 3.4 CI, CIX, and FI PL model parameters for LOS 1st, 2nd and 3rd floor corridors at 31 GHz.

FI, CI and CIX PL Models Parameters for 1st floor/LOS							
Pol.	**CI: d_0=1 m**		**FI**			**CIX**	
	PLE	**σ_{dB}**	**α_{dB}**	**β**	**σ_{dB}**	**XPD**	**σ**
V-V	1.60	2.39	62.26	1.60	2.04	/	/
V-H	2.86	6.73	85.43	1.38	3.00	19.95	6.54
FI, CI and CIX PL Models Parameters for 2nd floor/LOS							
Pol.	**CI: d_0=1 m**		**FI**			**CIX**	
	PLE	**σ_{dB}**	**α_{dB}**	**β**	**σ_{dB}**	**XPD**	**σ**
V-V	1.52	3.30	66.28	1.24	3.04	/	/
V-H	2.91	8	89.51	0.96	1.88	19.61	7.69
FI, CI and CIX PL Models Parameters for 3rd floor/LOS							
Pol.	**CI: d_0=1 m**		**FI**			**CIX**	
	PLE	**σ_{dB}**	**α_{dB}**	**β**	**σ_{dB}**	**XPD**	**σ**
V-V	1.33	2.56	66.12	1.06	2.14	/	/
V-H	2.72	7.11	87.10	1.02	1.96	20.44	6.86

3.6 DISCUSSION

As a comparison between the indoor and outdoor path loss, CI path loss models show that for the V-V polarization antenna configuration, the PLE value for the outdoor setting is 1.9, very nearly that of free space, and for indoor corridors, the values range from 1.3-1.6, with average PLE 1.4. All these values are less than the free space path loss exponent (*n=2*), meaning that the waveguiding effects occur in these indoor corridor environments. In the second-floor corridor, the PLE is 2.79 for the NLOS scenario. The

cross-polarization PLEs for LOS environments range from 2.7-2.9. The NLOS indoor cross-pol PLE is 3.5 and the outdoor cross-pol LOS PLE is 2.98.

Even though NLOS standard deviation is usually larger than that for LOS conditions, for our measurements the average value of the path loss model standard deviation for the LOS environment is 2.71 dB, whereas it is 2.37 dB for the NLOS co-polarized environment. Larger fluctuations in received signal strength about the distance-dependent mean path loss were observed at 31 GHz in LOS environments for V-H cross-polarized directional antennas (7.28 dB) compared to NLOS cross-polarized directional antennas (4.23 dB). So, LOS conditions for both polarization configurations (co- and cross-polarization) have higher standard deviation than the NLOS condition. These results might be attributed to the number of measurement points for the NLOS condition, which is smaller than the number of LOS measurement points (37).

Table 3.5 CI path loss model parameters for different environments.

Pol.	**LOS**		**NLOS**		**Outdoor LOS**	
	PLE	**σ [dB]**	**PLE**	**σ [dB]**	**PLE**	**σ [dB]**
V-V	1.48	2.75	2.79	3.37	1.95	2.01
V-H	2.83	7.28	3.57	4.23	2.98	5.17

Table 3.5 shows average values of our CI model parameters. A comparative analysis with the literature shows that our model parameters are in reasonable agreement with those found by other authors, for frequency bands near to 31 GHz; see Table 3.6.

Table 3.6 List of PLE and standard deviation values from the literature.

PLE	$\boldsymbol{Std._{dB}}$	**Scenario**	**Reference**
1.7	2.5	LOS_Indoor	[31]
1.9	1.1	LOS_Outdoor	[41]
1.6	2.5	LOS_Indoor	[42]
2.4	5.8	LOS_Indoor	[41]
3.5	3.3	NLOS_Indoor	[41]
4.3	9.1	NLOS_VH Indoor	[44]

From using different PL models to represent our collected measurement data we conclude that the directional CI path loss model better explained the physical propagation at 31 GHz, compared to the FI model. For example, the FI model slope values were 1.0 and 0.7 for V-V and V-H antenna polarizations, respectively, for the LOS third floor case. This suggests a potentially unrealistic situation with very low loss when using the FI model.

Using a simple version of CIX path loss model, the XPD factor has been calculated: XPD is 15.4 dB for outdoor LOS, and for indoor NLOS XPD is 11.17 dB. The average indoor LOS XPD is 20 dB, which shows a large isolation between co- and cross-polarized transmission when using a high gain directional horn antenna. For the cross-polarized configuration, this CIX model showed a reduced standard deviation compared to the CI model, most notably $\sigma_{\mathrm{CI}} = 4.2$ dB and $\sigma_{\mathrm{CIX}} = 3.1$ dB in NLOS environments.

3.7 SUMMARY

In this chapter we reported on propagation path loss measurements at 31 GHz in outdoor and indoor settings for different conditions (LOS and NLOS) and for different polarization (V-V and V-H). These results are of interest to understand the impact of the environment and antenna polarization on this 5G candidate band. The maximum distance range for the measurements was 65 meters for the outdoor environment and 76 meters for indoor measurements. These ranges gave us sufficient data to present three common path loss models: the CI, CIX, and FI path loss models. The CI path loss models showed that for co-polarization antenna configuration, the PLEs for both outdoor frontcourt and indoor corridors both have values of less than that of free space, i.e., less than two. For the corridors, this means that waveguiding effects occur, as expected. The NLOS scenario showed a higher attenuation and higher depolarization than the LOS scenario, also as expected. The simple CIX path loss model was used to effectively model path loss for the cross-polarized antenna configuration. The XPD factor was calculated for this model in the indoor LOS environment as 20 dB, for our high gain directional horn antennas. For our interior (still "outdoor") courtyard results, the transmitter antenna height showed a very slight impact on the received signal in terms of PLE when varied over the range of $1.5\ \text{m} \leq h_{TX} \leq 8.3\ \text{m}$. A comparative analysis with the literature shows that our results are in general agreement with that of other authors for frequency bands that are near to 31 GHz.

Results show that floating-point reference large-scale path loss model applied in our study might look better than the Close-in (CI) reference distance model by yielding a smaller value of standard deviation. Yet the reduction in the standard deviation is only by

a fraction of a dB compared to the simpler, physically-based CI model. The improvement in error with the more complex two-parameter FI model is typically insignificant. On the other hand, CI model standardizes all measurements around an inherent 1 m free space reference distance that is physically based, thus allowing easy use for varying distances, through the use of just a single parameter (PLE, or n).

CHAPTER 4

VEGETATION (SHRUB) ATTENUATION MEASUREMENTS

4.1 BACKGROUND

The most effective way purported to increase area spectral efficiency in 5G is to shrink cell size to provide more spectrum to each user [45]. The reduction of cell size and base station antenna heights in future cellular networks will force us to investigate the impact of vegetation on radio wave propagation at mmWave bands because the probability of a link traversing vegetation will increase. For such cases, it is important to know the range of expected attenuations. This knowledge will assist in optimizing spectrum utilization and enhancing the quality of services provided.

The study of propagation through vegetation is challenging due to variations in vegetation density, measurement geometry, and vegetation composition. In addition, vegetation is prone to environmental effects, such as surrounding construction that can introduce reflected, diffracted, or scattered signal components. Several measurements have been made to determine the attenuation of mmWave signals through vegetation, e.g., [45]-[49]. Measurement results and some methods for predicting attenuation exist, but many of these measurements were made through different kinds of trees or in a forest with gaps between trees.

In this chapter we present the results of a measurement campaign for three common broadleaf evergreen southeastern shrubs ((A) Japanese Boxwood, (B) Yaupon Holly Stokes Dwarf and (C) Shamrock Holly) for two different frequencies (31 and 5 GHz) and several measurement geometries. The measurements used a narrowband signal to estimate the specific attenuation (α) in dB/m and de-polarization effects.

4.2 WORK MOTIVATION

The lack of experimental studies specifically targeting foliage attenuation for (mmWave) radio paths obstructed by a single very dense vegetative obstacle, where both terminals are outside the vegetative medium, serves as the first motivation for this work. Different species of shrubs have different densities, trunk sizes, leaf and branch sizes, water content, and heights, and this can make it difficult to characterize and quantify their bulk attenuation in an understandable, easy to measure and relevant manner for use in a practical (engineering) model. Such vegetation is very common around houses and public buildings in urban areas for both landscaping and privacy purposes, hence characterizing its attenuation should be useful.

The second motivation for this measurements is the limited information on standardized measurement procedures for such cases. Some past measurement campaigns [50]-[54] explored only the obstructed link between two boresight-aligned directional antennas. This procedure has been used for lower frequency bands and for separated large trees, where diffraction around the trunk or tree canopy is the main propagation mechanism. However, in higher frequency bands and for very dense media like shrubs, the previous approach may not be best. A more reliable vegetation attenuation measuring technique is needed to measure the vegetation loss in a convenient way. Yet a clear procedure to

calculate vegetation attenuation for mmWave has not been reported. To the best of our knowledge there is no study of this type.

4.3 MEASUREMENT ENVIRONMENT

Measurements were conducted outside Swearingen Engineering Center building on the University of South Carolina campus in downtown Columbia, South Carolina. Measurement sites were selected based on accessibility and shrub density. Three sites were chosen for the measurements to address three common broadleaf evergreen southeastern shrubs, (A) Japanese Boxwood, (B) Yaupon Holly Stokes Dwarf and (C) Shamrock Holly, at two different frequencies with several measurement geometries. Measurement sites were selected based on accessibility and shrub density. Concrete walls were behind the transmitter and grass-covered ground for the first and second sites (shrubs A & B) Figures 4.4 - 4.5, whereas the third site (shrub C) was in an open area surrounded by a concrete ground surface, shown in Figure 4.6.

Measurements were conducted in late Fall, in humid weather but without precipitation. We also tried to avoid the effects of wind by measuring on non-windy days. Because most of the twigs and branches are of a size comparable to the wavelength of the measurement signals, random motion due to wind could cause some time-variant scattering.

4.4 MEASUREMENT EQUIPMENT

We used the same 31 GHz equipment that was used in the indoor path loss measurement campaign described in chapter 3. Furthermore, for the vegetation attenuation we also made 5 GHz measurements to study the effect at a different frequency. The following are the hardware components that were used for the 5 GHz frequency, see Figure

4.2: a Keysight (N5182A-MXG) vector signal generator was the signal source of the 5 GHz signal, and the Tx antenna was an ATM Inc. directional horn antenna (E541212-02) with gain 10 dBi and half-power beamwidth (HPBW) 60˚ degrees. The receiver used an identical antenna, followed by the R&S signal and spectrum analyzer. For the 5 GHz measurements, no up or down-conversions were required.

4.5 MEASUREMENT SETUP

Measurements were conducted at three sites, and at each, the transmitter (Tx) and the receiver Rx hardware were placed on a wheeled cart for ease of transportation and consistency of measurement antenna heights. The Tx and Rx antennas were located outside the vegetation; this is the scenario most likely to be encountered with practical systems. First, the antennas were positioned close to the edge of the vegetation to minimize outer leaf layer diffracted signal components and over the canopy diffracted signal components, yet still ensuring the shrubs were in the far field. The Tx and Rx antennas both were mounted at heights at least 5~10 cm lower than the measured shrub height. A manual adjustment positioner was built to up-tilt and down-tilt the antennas on both Tx and Rx. We also varied this geometry some to assess this, as we describe subsequently. In our second measurement setup, the receiver moved along the line of the signal propagation direction (outside the vegetation) away from the shrub front face at different values of shrub-Rx antenna distance, as will be discussed in section 4.7.2.

The measurements used a narrowband signal, specifically a single tone, to estimate the specific attenuation and de-polarization effects. Spatial averaging was done to remove small-scale fading effects. The measurement setups for 31 and 5 GHz are shown in Figures 4.1 and 4.2 respectively.

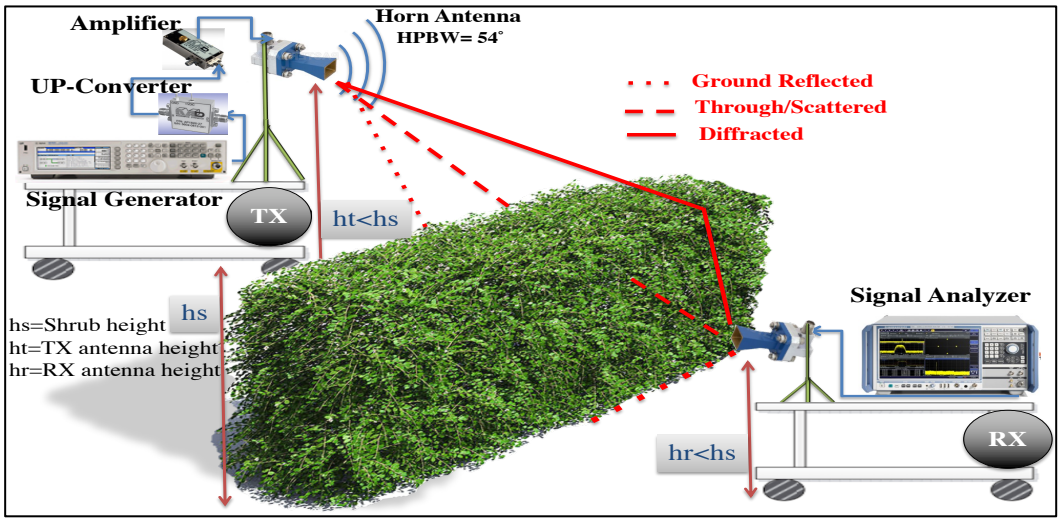

Figure 4.1 Measurement setup for 31 GHz shrub attenuation measurements.

Figure 4.2 Measurement setup for 5 GHz Tx (left), Rx (right), shrub attenuation measurements.

Figure 4.1 shows the propagation mechanisms that can exist in the presence of this vegetation measurement, and include diffraction, reflection and scattering. Different combinations of diffracted, reflected and scattered signal components may be present at every site. The superposition of signal components propagating through these mechanisms

results in significant frequency selective fading, manifested by variations in excess attenuation with measurement positions [55]. The spatial averaging, we applied yields an estimate for the bulk material attenuation.

4.6 MEASUREMENT STEPS

1. CALIBRATION

To improve accuracy and to avoid the effects of nearby obstacles, we first made a calibration measurement in LOS conditions with transmitter (Tx) and receiver (Rx) directional antennas boresight aligned in the same location where the shrub attenuation measurements were conducted. Shrub attenuation was determined as the difference between measured average received power through a specific kind of shrub, denoted $P_{r_{Measured}}$, and the received power of the LOS calibration link, denoted $P_{r_{FS}}$, in the same measurement location for the same Tx-Rx separation distance, including the width of the shrub:

$$\mathrm{L[dB]} = \mathrm{P_{r_{FS}}} - \mathrm{P_{r_{Measured}}} \tag{4.1}$$

2. SMALL-SCALE FADING

For averaging out small scale fading (due to multi-path components (MPCs) from reflections, diffraction, and scattering from the floor, nearby walls and other obstructions), we collected data to compute a spatial average at each measurement point. This consisted of three individual measurements separated by approximately one wavelength of the corresponding frequency, all at the same link distance. We repeated this process for 4, 2, and 6 times for shrubs A, B, and C, respectively by moving the Rx antenna a wavelength's distance at each measurement point. This is illustrated in Figure 4.3. Points L_1 and L_2 on the left side of the shrubs are different Tx measurement locations where at each Tx location, three different Rx measurement points were used, with the result averaged. We also

calculated the standard deviation (α) in dB of these measurements as an estimate of the spatial variation.

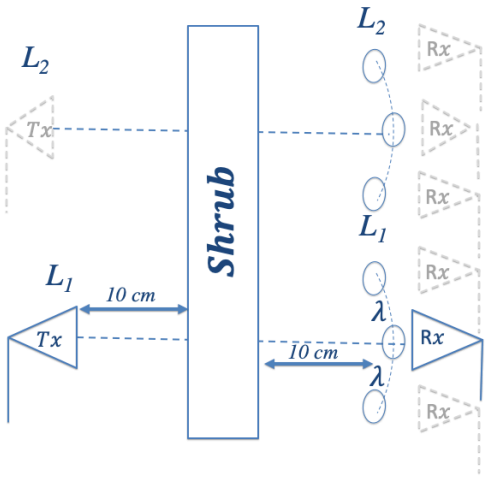

Figure 4.3 Measurement geometry to average the small-scale fading effect.

3. SHRUB DE-POLARIZATION

To quantify the de-polarization effect of the shrubs, all the measurements were done for both co- and cross-polarized antenna configurations. For co-polarization measurements, the Tx and Rx horn antennas were vertically polarized (V-V), whereas for the cross-polarization measurements, the Tx was vertically polarized, and the Rx antenna was horizontally polarized (V-H). Ultimately it would be of value to understand the relationship between the polarization of a signal propagating through the shrub and the depth and density of the shrub.

4.7 RESULTS

4.7.1 EFFECT OF SHRUB DENSITY

Usually, foliage attenuation is modeled as excess loss in addition to the free space path loss. Typically, this excess loss is divided by the total length of the path traveled by

the radio signal inside the vegetated area, to obtain what is termed the specific attenuation, expressed in dB per unit length [56]. According to the International Telecommunications Union Radio sector, ITU-R recommendation P.833-9 [57], when the radio path is obstructed by a single vegetative obstruction where both terminals (Tx and Rx) are outside the vegetative medium, such as a path passing through the canopy of a single plant species, this situation can be modeled on an approximate basis in terms of the specific attenuation and total excess loss as follows:

$$\mathrm{PL} = \mathrm{PLFS\ (dB)} + \mathrm{M\ (dB)} \tag{4.2}$$

$$\alpha = \frac{\mathrm{M\ (dB)}}{\mathrm{d\ (m)}} \tag{4.3}$$

where PL denotes path loss in dB, PLFS is free space path loss in dB, and M is the total shrub attenuation in dB for the shrub depth d (m). The specific attenuation α is M/d dB/m. The following results are for 31 GHz for the three distinct species of broadleaf evergreen shrubs.

A) SHRUB A, JAPANESE BOXWOOD (DENSEST)

Here the measurements were conducted for four locations along the Boxwood shrubs. Even though the shrubs are pruned to form a hedge row with nearly constant width, the measured path losses at the several locations are slightly different: see Table 4.1. We attribute this to the variation in density.

Table 4.1 Attenuation results of Japanese Boxwood shrub.

Pol.	PL (dB)				Avg. PL (dB)	α (dB/m)
	L1	L2	L3	L4		
V-V	133	133	143	138	136.75	24.4
V-H	134	133	145	135	136.75	24.4

In Table 4.1, the values of the specific attenuation for V-V and V-H polarization are the same, and we attribute that to the high density of this Boxwood shrub (A); see Figure 4.4. The likely anisotropic scattering caused by shrub stems and leaves causes a rotation in the signal polarization to a range of angles, hence the polarization for any signal passing through the shrub may appear almost uniform.

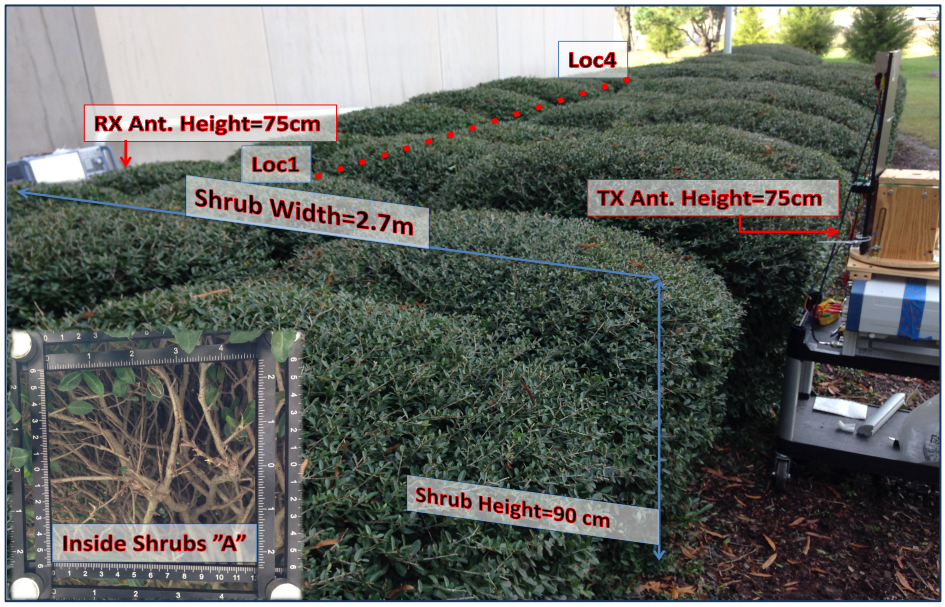

Figure 4.4 Directional measurement setup with Tx & Rx antenna at edge of Japanese Boxwood shrubs A; lower left inset is close up of the dense branch distribution inside shrubs.

B) SHRUB B: YAUPON HOLLY STOKES DWARF (SPARSEST)

These measurements were conducted for two locations along the Yaupon holly shrubs. Results appear in Table 4.2. This shrub was located adjacent to concrete walls and a metal louver shading window which would be a good signal reflector. Thus, we aimed our directional antennas to minimize this effect as much as possible. See Figure 4.5 for the measurement setup.

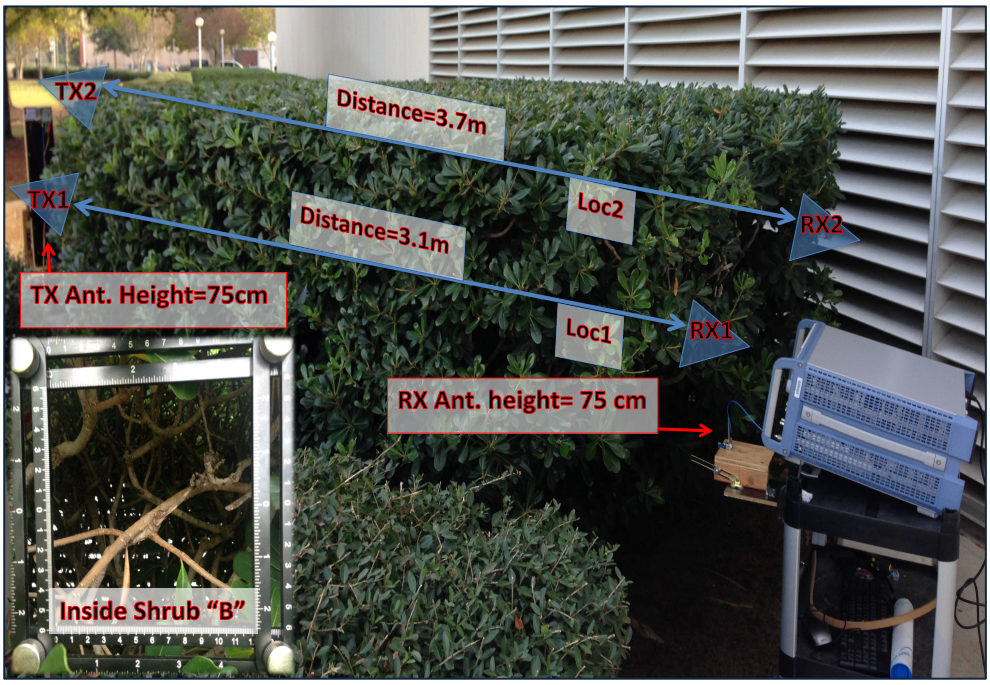

Figure 4.5 Directional measurement setup with Tx and Rx antenna deployed at edge of Yaupon holly shrubs *B*; lower left inset is close up of dense branch distribution inside shrubs.

Table 4.2 Measurement and results of Yaupon holly shrub.

Pol.	PL (dB)		Avg. PL (dB)	α (dB/m)
	L1	L2		
V-V	126	128	127	16
V-H	121	126	123.5	15

C) SHRUB C: SHAMROCK HOLLY (MEDIUM DENSITY)

The Shamrock Holly measurements were conducted for six locations. See Table 4.3 for results.

Table 4.3 Measurement results of Shamrock Holly shrub

Pol.	PL (dB)						Avg. PL (dB)	α (dB/m)
	L1	L2	L3	L4	L5	L6		
V-V	132	119	121	112	122	123	121.5	17.9
V-H	133	120	120	114	125	123	122.5	18.3

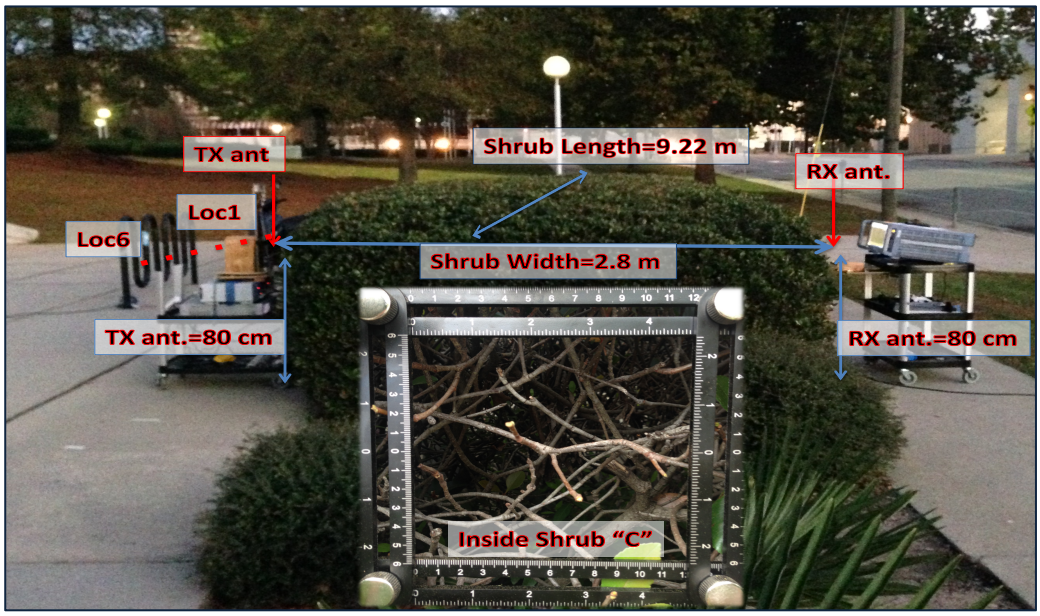

Figure 4.6 Directional measurement setup with Tx & Rx antenna at edge of Shamrock holly shrubs C; lower center inset shows close up of medium density branch distribution inside shrubs.

4.7.2 FREQUENCY & MEASUREMENT GEOMETRIC CONSIDERATION

For two different frequencies we measured the path loss through shrub B for four different Tx-Rx separation distances, illustrated in figure 4.7. At 5 GHz, the wavelength is ~6 cm, larger than the physical dimensions of most of the shrub features in both the canopy (leafy outer) layer and the inner branch network. One can expect different scattering effects in these two layers. At 31 GHz, the wavelength is ~1 cm, which is smaller than both the leaves and most of the shrub branch diameters. These shrub feature sizes in relation to wavelength account for the larger attenuations at the higher frequency. The comparative 5 and 31 GHz attenuation results are listed in Table 4.4. As expected, for all shrub kinds, attenuation increases as frequency increases from 5 to 31 GHz.

Also, we can see from Table 4.4 that when the Tx antenna is closest to the shrub the attenuation is high. In this case the signal reaches the receiver essentially only by means of

the forward scattering path which is the most attenuating path, whereas an increase in received signal strength is expected as the antenna is moved away from the shrubs because this better allows for diffraction over the top of the shrub and reflection from surrounding walls. For both frequencies, specific attenuation decreases as the distance between (both) antennas and the shrub increases. This likely means that additional reflected, scattered, and diffracted energy can reach the Rx as the antenna "field of view" widens as the antenna is moved away from the shrub. Our best estimate of the actual shrub attenuation is that for the smaller distances.

Considering the near field and far field phenomena of the electromagnetic field around an object such as a transmitting antenna, or the result of radiation scattering off an object (shrub), to get the best estimate of the shrub specific attenuation, the Rx antenna should be close to the shrub so that any reflected transmitted signal components from surrounding objects are outside the Rx antenna main beam. We also have to ensure that the shrub is beyond the Fraunhofer far-field distance (D_f) [58], [59] because the far field carries a relatively uniform plane wave pattern of the transmitted test signal,

$$D_f = \frac{2D^2}{\lambda} \tag{4.4}$$

where D is the largest aperture dimension of the antenna and λ is the transmitted signal wavelength. According to (4.4) and using our value of dimension D for each antenna, we find that our second measurement (Table 4.4), with Tx antenna at distance 10 cm from the shrub and Rx antenna at distance of 25 cm (L_2) from the shrub, is the best measurement to estimate the specific attenuation value of the shrub. This measurement setup also satisfies (4.4) for both 31 GHz and nearly for 5 GHz frequency.

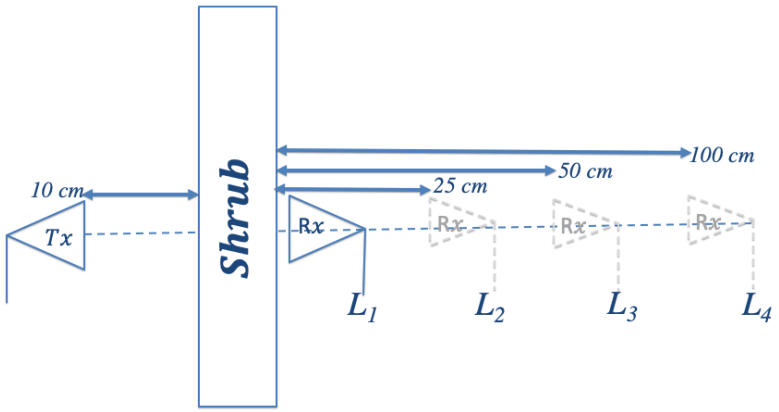

Figure 4.7 Different measurement distances via different shrub-Rx antenna separation distances.

Table 4.4 Average specific attenuations for two frequencies vs. distance from antenna to shrub B.

Distance of Rx Antenna to Shrubs (cm)	0	25-30	50	100
5 GHz Average α (dB/m)	17.85	15.23	12.83	10.03
31 GHz Average α (dB/m)	26.33	24.12	21.8	19

4.8 CONCLUSION

In this chapter, radio wave attenuation and depolarization effects through three broadleaf evergreen shrubs were reported, based upon measurements at two frequencies, 5 and 31 GHz. From this, we analyzed the relationships between this attenuation and the two frequencies, and the shrub density, depth, and measurement geometry. These vegetation attenuation measurements revealed the large attenuation magnitude for the mmWave bands, and how this attenuation varies with the shrub density. The average value of the specific attenuation α, in dB/m, was computed. The measured specific attenuation is very large, at least 15 dB/m, and up to 24 dB/m for the densest shrub. This is much larger than what we have found in the literature for vegetation attenuation. As would be expected, the higher the

density of shrub branches and foliage, the larger the specific attenuation. These results will be useful for link budget design, and outdoor and outdoor-indoor models for future mmWave communication.

The results have also emphasized the importance of careful measurement geometry in signal propagation studies to ensure that appropriate measurement geometries are chosen and taken into account in the interpretation of the results. Most importantly, care needs to be exercised to ensure that the ground and site specific artifacts do not influence the attenuation measurement. Any contributions from ground reflection and/or diffraction over the top or edges of the shrubs could influence the attenuation measurement. We have shown that measurement geometry; specifically, the distance from the directional antenna(s) to the shrub can substantially affect the estimate of specific attenuation as additional multipath components can reach the receiver; specific attenuation measured in this way decreases as the antennas are moved away from the shrub, hence a suitable distance must be defined to unambiguously define the actual shrub specific attenuation.

The study has confirmed that there is a strong frequency dependence of signal attenuation by vegetation, with higher frequencies experiencing more attenuation than low frequencies. The results show that the attenuations at 5 GHz are much smaller than at 31 GHz.

CHAPTER 5

5G CANDIDATE WAVEFORM

5.1 BACKGROUND

The modulation scheme or schemes adopted for 5G will play a major role in determining the performance and complexity of the handsets and other nodes and will have a major impact on performance. In addition to the high data rates needed, 5G modulation scheme performance issues include peak to average power ratio, spectral efficiency, and performance in the presence of interference and noise [60].

Because of the variety of future application and the wide range of the available spectrum that the millimeter wave bands offer, 5G systems will have to cope with a high degree of heterogeneity in terms of services and requirements. The flexible and efficient use of non-contiguous unused spectrum for different network deployment scenarios will be a key challenge for 5G systems [62]. So, we will need a flexible system to be able to make the right trade-offs according to the requirements of the applications and according to the wireless channel conditions.

The importance of modulation schemes in wireless systems has led to advancements in digital signal processors (DSPs), microprocessor design, and various cellular standards. Much of the success of wireless standards is due to the contribution of modulation schemes that allow power efficient mobiles that require minimal bandwidth

and battery size and provide clearer voice reception and low-error-probability data. Thus, modulators (and of course companion demodulators) are fundamental components in wireless systems.

The goal of a modulation technique is not only to transport a message signal through a radio channel but to achieve this with the best quality, power efficiency, low cost, high flexibility, and the requirement that the technique should effectively use the available resources. There are a number of factors that enter into the choice of a modulation scheme for use in a wireless application. Performance of a cellular system is dependent on the efficiency of the modulation scheme in use. In this chapter, a closer study of a specific modulation technique is explored in order to determine its suitability for a particular set of wireless applications.

In this chapter, we analyze a waveform candidate that can be suitable for specific 5G application cases: non-coherent M-ary frequency shift keying (NC-MFSK). It is well known that NC-MFSK is often used for its simple design and low-cost implementation. Furthermore, MFSK is a most energy-efficient scheme. In [63], the authors refer to the NC-MFSK scheme as “Green Modulation” for its simplicity and low-energy consumption.

5.2 CONSTANT ENVELOPE MODULATION SCHEMES

Digital communication systems operate in the presence of path loss, multipath propagation, interference, and atmospheric-induced fading. In order to maintain sufficient received power at the destination, it is required that a device for generating adequate transmitter output power based on fixed-but-limited available power be employed, so modulations that transmit information via their amplitude, e.g., quadrature amplitude

modulation (QAM), and therefore need a linear amplifying characteristic, are not optimal in this sense for use on channels operating where maximum transmitter power efficiency is required [64].

In the mobile radio channel, since multipath fading distorts the amplitude of the carrier, a signal that is sent by modulating the phase or frequency of the carrier, which has no impact on the amplitude, is often preferable. Those modulations are called constant envelope modulations*;* that is, no variation in envelope amplitude occurs. The distortion of carrier amplitude by other factors such as fading or nonlinear amplification will not affect the signal. Therefore, it is possible to use a nonlinear amplifier since such modulations are robust to such amplitude distortions.

All constant envelope modulations allow the transmitter's power amplifiers to operate at or near saturation levels [64], implying the most efficient use of the available transmit power. On the other hand, standard (filtered) BPSK and QPSK, and QAM modulations contain AM components in the modulated envelope, which require from 3 to 6 dB of back off (from saturation) in the output power amplifier to reduce or eliminate distortion and spectrum "splatter" of sideband components that might cause adjacent channel interference (ACI) [65]. Most non-constant envelope modulations actually require fully linear power amplification and thus for power outputs comparable to that of saturated RF power amplifier stages, linear modulations require RF power amplifiers that output up to 4 times more power. This is needed to handle the peak envelope power (PEP), which is the highest envelope power supplied to the antenna transmission line, required by the waveform [66]. These larger power amplifiers are less efficient, consume more primary

power, generate more heat and are more expensive than their “Class C” amplifier counterparts [65].

Another consideration regarding RF amplifier devices that operate in a nonlinear mode at or near saturation is the spectral spreading that they reintroduce, due to the nonlinearity subsequent to band limiting prior to amplification. Because of the need for the transmitted power spectrum to fall under a specified mask imposed by regulating agencies such as the FCC or International Telecommunications Union (ITU), the modulation must be designed to keep this spectral spreading to a minimum [64]. This constraint necessitates limiting the amount of instantaneous amplitude fluctuation in the transmitted waveform in addition to imposing the requirement for the constant envelope.

Constant envelope schemes have advantages in terms of transmitter efficiency and receiver simplicity, as well as minimizing electromagnetic compatibility (EMC) problems, which occur when one piece of electronic equipment or an electromagnetic system is adversely affected by the operation of another [67]. Constant envelope schemes showed major advantages in WLAN type applications [62]. Foremost amongst these is the lower power consumption of Class C amplifiers and of limiting IF amplifiers at the receiver.

5.3 MFSK FEATURES AND APPLICATIONS

1. Power Efficiency: as a constant envelope modulation, MFSK is a power efficient modulation scheme whose efficiency improves as the number of frequencies employed (M) increases, of course at the expense of additional complexity and smaller bandwidth efficiency. The power efficiency of FSK can help overcome path loss and shadowing in mmWave bands. In the future 5G broad range of applications, sensors are typically powered by limited-lifetime batteries which are

hard to replace or recharge [68]. Similarly, for other applications where a large number of sensors are deployed over a region, the circuit energy consumption is comparable to the transmission energy due to the short distance between nodes [69]. Thus, minimizing the total energy consumption in both circuits and signal transmission is a crucial task in designing the hardware. So, the used modulation should be simple enough to be manufactured but still robust enough to provide the desired service.

2. Fast Start-Up Times: For many applications where the devices frequently switch from sleep mode to active mode, modulator circuits should have fast start-up times. An M-ary FSK modulator with $M = 2^b$ orthogonal carriers could benefit from the advantage of using the Direct Digital Modulation (DDM) approach, meaning that it does not need the mixer and the Digital to Analog Converter (DAC) [69]. This property gives MFSK a faster start-up time than the other modulation schemes.
3. Reliable Link: M-FSK has the advantage that as (M) increases, a more reliable link can be provided, but at the expense of a spectral efficiency reduction (i.e., bandwidth expansion). Thus, MFSK can use the large bandwidth at mmWave frequencies to achieve multi Gbps wireless links. This is a consequence of the energy efficiency of point #1.
4. Robust to Hardware Impairments: FSK is also less affected by hardware impairments (amplifier non-linearity/phase noise) than typical MPSK and MQAM modulations, which suffer more in terms of BER in the presence of these impairments [70].

5. FSK modulation encodes information in the signal frequency, so the transmitted signal has a constant envelope. The power amplifier is often one of the most expensive components in the modem. In FSK, cheap nonlinear amplifiers can be used with high power efficiency and hence the modulated signal is less sensitive to amplitude distortion introduced by the channel or the hardware. The price exacted for this robustness is a lower spectral efficiency: because the modulation technique is nonlinear, it tends to have a higher bandwidth occupancy than the amplitude and phase modulation techniques.

6. FSK is often the preferred method of modulation for maritime data communication, due mainly to its immunity from amplitude interference and equipment simplicity. Radio telex, Navtex, and some facsimile transmissions use a narrow band form of FSK known as audio FSK (Fast Information Blocks (FIB) and Fast Information Channel (FIC)) [71].

5.4 NON-COHERENT MFSK FEATURES

The theory of noncoherent detection assumes that the phase of the received signal is arbitrary rather than carefully controlled and estimated. We consider the noncoherent version of MFSK for the following reasons:

1. The required additional energy for NC-MFSK to equal CMFSK performance is small, for example, noncoherent FSK requires, at most, only 1 dB more E_b/N_0 than that for coherent FSK for the probability of bit error: $P_b < 10^{-4}$ [72].
2. The noncoherent FSK demodulator is considerably easier to build since coherent reference signals need not be generated. The extra hardware required for coherent

FSK detection is hence hard to justify. Coherent FSK is not often used in practice due to the difficulty (and cost) in generating multiple reference frequencies close together at the receiver. Furthermore, for large M, MFSK coherent detection requires the receiver to obtain a precise frequency and carrier phase reference for each of the transmitted orthogonal carriers, increasing the complexity of the detector. Thus, most practical MFSK receivers use non-coherent detectors.

3. Flexibility: FSK has the advantage that the same transmitted signal can be demodulated with low complexity for low-price equipment, and with high complexity for high-priced equipment. Coherent FSK signals can be noncoherently demodulated to avoid the carrier recovery, using non-coherent detection will reduce the receiver's complexity at the expense of performance loss. This feature gives the noncoherent detection system the flexibility to be used with both CFSK and NC-FSK.
4. For coherent FSK signals to be orthogonal, the FSK frequencies separation must be a multiple of $1/(2T_{sym})$. The minimum null-to-null bandwidth for coherent FSK is $B_{null}= (M + 3) R_s/2$ Hertz. For noncoherent FSK signals to be orthogonal, the FSK frequencies separation must be a multiple of $1/T_{sym}$. The minimum null-to-null bandwidth for noncoherent FSK is $B_{null}= (M + 1) R_s$ Hertz. Thus, for the same symbol rate R_S, more system bandwidth is required for noncoherently detected FSK than for coherently detected FSK. For large M, this is approximately a factor of 2.

5.5 NC-MFSK BIT ERROR PROBABILITY OVER THE AWGN CHANNEL

In this chapter, we start the analysis based on an AWGN channel to evaluate NC-MFSK performance using the NYUSIM channel simulator that is described in chapter six.

The AWGN model is often used as a channel model in which the only impairment to communication is a linear addition of wideband or white noise with a constant spectral density (expressed as watts per hertz of bandwidth) and a Gaussian distribution of amplitude [73]. The model does not account for fading, frequency selectivity, interference, nonlinearity or dispersion. However, it produces simple and tractable mathematical models which are useful for gaining insight into the underlying behavior of a system before these other phenomena are considered.

For NC-MFSK the bit error probability over the AWGN channel is

$$P_{b,NC-MFSK} = \left(\frac{M/2}{M-1}\right)\sum_{n=1}^{M-1}\frac{(-1)^{n+1}}{n+1}\binom{M-1}{n}\exp\left(-\frac{n(\log_2 M)E_b}{(n+1)N_o}\right), \quad (5.1)$$

where $\binom{M-1}{n} = \frac{(M-1)!}{(M-1-n)!n!}$, $k=\log_2 M$ bits/symbol, and $E_s=E_b(\log_2 M)=kE_b$.

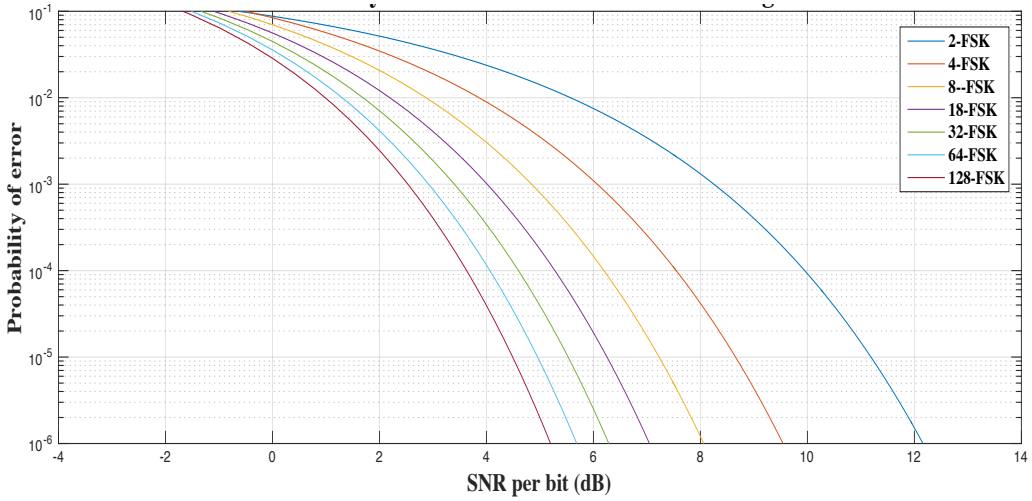

Figure 5.1 NC-MFSK error probability vs. E_b/N_0 for different modulation order M.

To confirm simulation validity, NC-FSK signal samples were generated and sent in the presence of AWGN. Figure 5.1 shows the performance improvement of MFSK with an increase in the modulation order. The noise power was defined by the ratio of energy

per bit to noise power per Hertz (E_b/N_0). This ratio is proportional to the well-known signal to noise ratio (SNR) and is referred to as this for convenience.

5.6 CANDIDATE MODULATION SCHEME EVALUATION AT 31 GHZ

The initial performance verification of communication systems at the early stages of the design cycle is most often performed based on the channel characteristics. Therefore, accurate emulation of fading channels is a key step in the design and verification of wireless communication systems. For this reason, mmWave channel modeling and characterization has been attracting great attention in the literature. Currently, models such as the 3D-3GPP Model, COST 2100, METIS Model, and 3D-mmWave channel model proposed by New York University (NYUSIM) Wireless Lab are available [75]. In this chapter we evaluate the Non-Coherent M-ary Orthogonal Frequency Shift Keying (NC-MFSK) modulation performance at 31 GHz and its features that were described in chapter 5. NYUSIM is the channel model that we consider in evaluating our candidate modulation scheme.

5.7 FLAT AND FREQUENCY SELECTIVE CHANNELS

In multi-path channel environments, the ratio of the root mean-square (RMS) delay spread (σ_τ) to the symbol duration (T_{sym}) quantifies the severity of inter symbol interference (ISI) for single-carrier systems, and this ratio determines the complexity of the equalizer required at the receiver. For example, typically when the symbol period is greater than 10 times the R.M.S. delay spread, no ISI equalizer is needed in the receiver [76].

The correspondence with the frequency domain is the notion of coherence bandwidth, which is proportional to the inverse of the delay spread: the shorter the delay spread, the larger is the coherence bandwidth. Approximately speaking, coherence bandwidth is the bandwidth over which the channel can be assumed to have a flat (non-

selective) amplitude response. In other words, the (frequency) flat channel is the channel that passes all spectral components with approximately equal gain and linear phase, meaning all frequency components of the signal will experience the same magnitude of fading. In contrast, in frequency-selective fading the coherence bandwidth of the channel is on the order of, or even smaller than the bandwidth of the signal. Different frequency components of the signal will experience different fading.

Even though our measurements were all for a narrow band signal, in this chapter we evaluate our candidate modulation scheme for a wide band signal. The difference between wideband and narrowband fading models is that, as the transmit signal u(t)'s bandwidth (BW) increases so that the delay spread approaches BW^{-1}, the approximation $u(t - \tau_n(t)) \approx u(t)$ is no longer valid. Thus, the received signal is a sum of all copies of the original signal, where each copy is delayed in time by τ_n and shifted in phase by $\phi_n(t)$. The signal copies will combine destructively when their phase terms differ significantly and will distort the direct path signal when $u(t - \tau_n)$ differs from u(t). So, in the case of a wideband signal we incur a form of distortion due to the multipath delay spread.

5.8 NC-MFSK EVALUATION

In wireless communication systems where interference is a major issue, the performance of a modulation scheme in an interference environment is extremely important. In general, the interference effects on a signal as well as the performance of the specific demodulator can be analyzed as a complete system using simulation to determine relative performance. The performance of our candidate modulation scheme has been evaluated via an "end-to-end" system wireless mmWave channel simulator, that we created from modifying a channel simulator (NYUSIM) that was developed based on realistic

measurements for both flat fading and time-selective channels in different scenarios (LOS & NLOS). We combine this simulator with a transmitter and receiver simulation (data stream generator, modulator and demodulator). This simulation models the physical layer. The simulator has been run for different system settings, i.e., modulation order, symbol rate, and bandwidth. The performance evaluations enable us to present enhancements and trade-offs that can be employed to improve the system performance by adjustment of the design parameters. This includes adjustment of modulation alphabet size and symbol rate, which together determine bandwidth.

5.8.1 NC-MFSK PERFORMANCE EVALUATION ASSUMPTIONS

Several assumptions were made in our simulations. These are described as follows:

- No equalizer was used at the receiver for simplicity. This is because typically, equalization for nonlinear modulations is generally complex. Furthermore, when the symbol period is greater than 10 times the R.M.S. delay spread σ_τ, performance does not degrade by much from ISI, and hence no receiver equalizer is needed. In the simulator software, for flat fading, the symbol times were selected to be longer than at least ten times the mmWave channel R.M.S. delay spread.

- One of our underlying assumptions is that for the pedestrian mmWave channel we can consider the channel to be time-invariant. The pedestrian speed for example is ~3m/sec and for the 31 GHz frequency we use, the wavelength is λ= 0.01 meters, so the maximum Doppler frequency f_d = 300 Hz, and the resulting coherence time is approximately 1/300=0.003 sec. Compared to typical symbol times this corresponds to thousands of symbols before any change can occur to the channel; this supports our assumption of considering the propagation channel time-invariant.

5.8.2 NC-MFSK PERFORMANCE EVALUATION PROCESS

We used the NYUSIM channel simulator to evaluate the performance of NC-MFSK over different mmWave channels. The main programming processing loops perform the following steps:

1. Generate random binary source data.
2. Apply NC-FSK modulation to the data symbols, with a selected value of alphabet size *M*, symbol duration, and sampling rate.
3. Generate the radio channel. The NYUSIM main operations are,
    - Selection of the environment (LOS or NLOS).
    - Determination of propagation pathways.
    - Determination of propagation channel matrices for the paths.
    - Composition of the radio channel impulse response h(t).
4. Pass the modulated signal through the NYUSIM channel. In a frequency selective channel, the channel output can be expressed as the convolution of the input signal x(t) and the channel impulse response h(t) plus some noise, r(t)=h(t)*x(t)+ n(t).
5. Add the noise (AWGN) n(t) for the desired value of SNR.
6. Demodulate the received signal using the NC-MFSK demodulator.
7. Evaluate the performance by calculating the number of bit errors.

We simulated the NC-FSK transmitted signals for different symbol rate R_S for different modulation levels over different channels using the NYUSIM mmWave channel simulator. Our aim was to determine whether or not the NC-MFSK can really perform well in terms of acceptable BER, and how large a practical alphabet size M might be for a given

amount of transmitted power. We also validated the basic performance of the simulation itself. For the simulation, the following are our underlying system assumptions:

1) Constant transmitter power.
2) Variable data rate MFSK modulation scheme with non-coherent (NC) detection;
3) Variable bandwidth or fixed bandwidth system, for different simulation runs.
4) Perfect estimation of the channel status is available at the transmitter within a permissible delay; this helps to enable adaptive modulation order according to the channel condition.

Assumption (1) is often relaxed in practical systems that use transmitter power control, but as noted, for our pedestrian channels, time variation is slow enough to allow the channel fading and path loss to be considered constant. Future work could consider long-term performance that allows transmit power adaptation.

5.8.3 POWER DELAY PROFILE (PDP) GENERATED BY NYUSIM

In practice the number of pulses that can be distinguished with a very wideband signal is very large. Reflections from obstacles near the Tx or Rx (which cause reflection with a short excess delay), often arrive with power close to that of a LOS component. This gives a fairly flat transfer function H(f). Some relatively strong impulses from remote obstacles (e.g., high-rise buildings) can cause strong reflections with large excess delay. The combined effects often result in multiple clusters of reflections or multipath components (MPCs).

Time clusters are composed of MPCs traveling close in time but can arrive from potentially different angular directions in a short propagation time window. NYUSIM modeled the channel as a tapped delay line implementation [77], and the number of taps (N) is determined by the product of delay spread and the system sampling rate. NYUSIM determines the discrete tap spacing Δt so that the path gains and the power delay profiles generated by NYUSIM would look like a series of spikes as shown in Figure 5.2. These "taps" are weighted proportional to the energy in the reflected waves from the different paths of the signal. As noted, these channel components are convolved with the transmitted signal components to yield the received signal.

5.9 FSK IN PRESENCE OF INTER-SYMBOL INTERFERENCE (ISI)

Time-delay spread caused by differing-length transmission paths between transmitter and receiver can have a serious detrimental effect on the received FSK modulated signal. This time delay spread introduces data-dependent ISI, so to avoid the interference the symbol time should be much larger than the delay spread. Another alternative is to employ channel equalization, which is processing at the receiver to undo the delay distortion. This of course increases receiver complexity, and is something we do not address here, but is recommend as an area for future research.

From the perspective of the frequency domain, ideally, the spacing Δf between FSK tones should be selected in such a way that they do not encounter frequency selectivity. In that case, these tones experience a flat gain in the frequency domain that can be easily compensated for at the receiver side. This generally means reducing the spacing, which means reducing data rate.

If frequency spacing is not reduced, the channel's frequency selectivity will fade different FSK symbols differently. FSK symbols will arrive not only with a random amplitude but also a distorted shape, and different symbols incur different channel gains. What we will show subsequently illustrates MFSK performance simulated over frequency selective channels.

5.10 NC-MFSK OVER NYUSIM

5.10.1 EXAMPLE (1): NC-8FSK Performance in NLOS / Micro-Urban Environment.

We tested the performance of NC-8FSK over a channel generated by the NYUSIM channel simulator whose power delay profile is shown in Figure 5.2. The R.M.S. delay spread σ_τ =67 ns, Tx-Rx separation distance is 1 km and path loss exponent PLE=3.7[1]. For both the transmitter and receiver, antenna polarization is co-polarized.

A. FLAT FADING CHANNEL CASE

Table 5.1 contains the transmit signal parameters for this case. Figure 5.3 plots the spectrum of both the transmitted and received NC-8FSK signal. The transmitted signal spectrum (yellow line of Figure 5.3) shows that the NC-8FSK modulated signal is composed of eight tones each having a normalized peak (0 dB) separated by ~ 78 kHz. The received signal (red line of Figure 5.3) also shows the 8 tones when passed the through the mmWave multipath channel.

---

[1] The PLE is reported just for completeness since as noted, the channel is considered time-invariant, thus the PLE sets the mean channel gain.

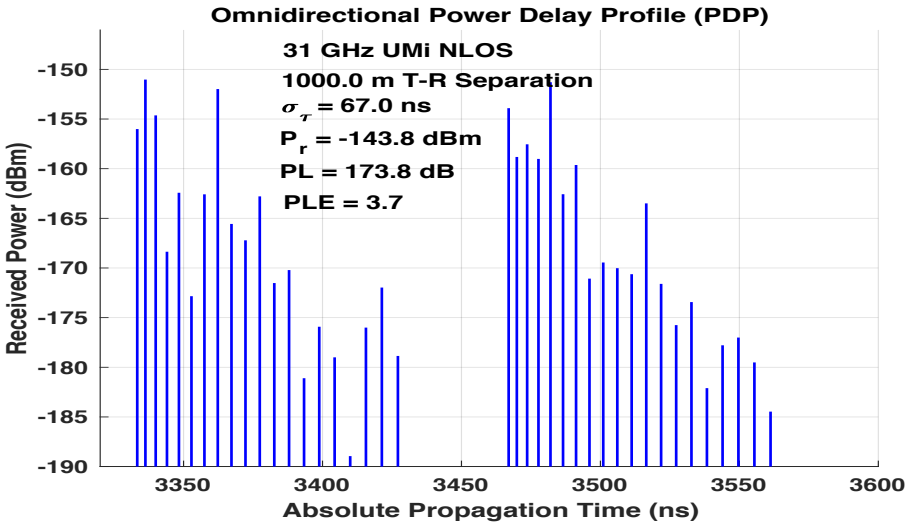

Figure 5.2 Example (1) Power Delay Profile (PDP) generated by NYUSIM for UMi NLOS channel.

Table 5.1 Transmit signal parameters for Flat Channel Case.

Transmitter setting					
M	BW(MHz)	Δf (Hz)	R_s (sps)	R_b(kbps)	T_{Sym} (ns)
8	6.25	781250	781250	2343.75	1280

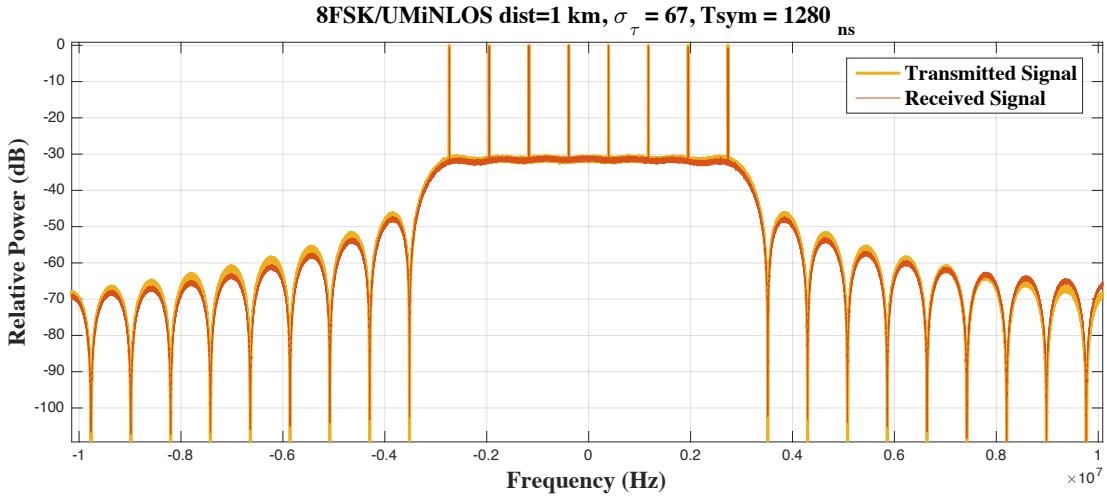

Figure 5.3 Spectrum of NC-8FSK over a flat-fading channel.

Figure 5.3 shows that the channel is flat or frequency nonselective and passes all spectral components of the transmitted signal with approximately equal gain (and linear phase, which of course is not shown in the power spectrum). The eight tones comprising the FSK signal maintain the same frequency separation and power levels relative to each other. This is because the signal symbol time T_{sym} =1280 ns is much larger than the R.M.S delay spread σ_τ =67 ns, or equivalently, the signal BW is much smaller than the coherence bandwidth.

B. FREQUENCY-SELECTIVE FADING CHANNEL CASE

Table 5.2 contains the transmit signal parameters for this case. Figure 5.4 shows the received signal spectrum (green line) after passing through the mmWave frequency selective fading channel. There are still eight identifiable tones, but their relative power levels differ due to the frequency-selective fading. Figure 5.5 shows the NC-8FSK spectra in the same channel but for 80 ns and 1280 ns symbol time.

Table 5.2 Transmit signal parameters for Freq. Selective Channel Case.

Transmitter setting					
M	BW (MHz)	Δf (MHz)	R_s (Msps)	R_b(Mbps)	T_{Sym} (ns)
8	100	12.5	12.5	37.5	80

As with all digital communication systems, performance is measured in terms of error ratios, so we evaluated the bit error rate (BER) performance of NC-8FSK for different symbol rates over several wireless mmWave channels. The NC-8FSK performance is for the same channel but this is evaluated for different symbol times (and signal bandwidths). The BER versus received signal to noise ratio (E_b/N_0) is shown in Figure 5.6.

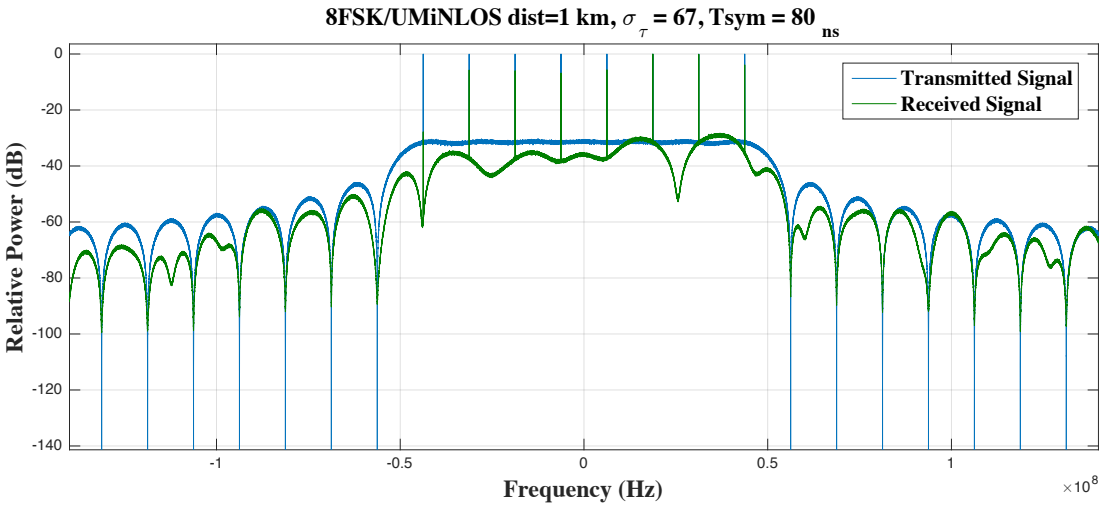

Figure 5.4 Spectrum of NC-8FSK over frequency-selective channel.

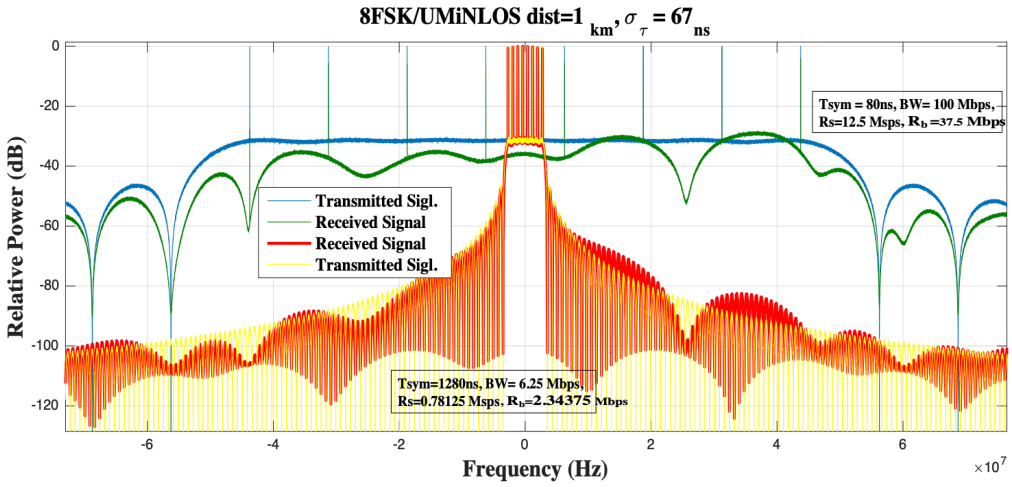

Figure 5.5 Transmitted and Received Signals through both Flat and Freq.-Selective channels.

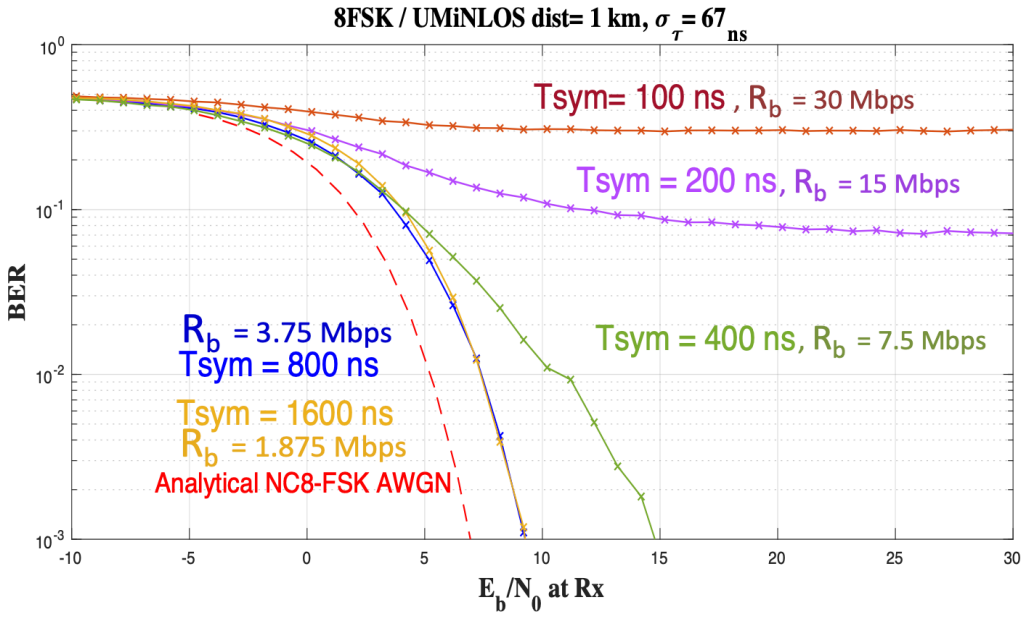

Figure 5.6 System performance over NLOS Micro-Urban channel for different symbol times.

We can see that as the symbol time increases, the performance improves and for very large symbol time the performance become closer to the analytical AWGN (non-dispersive channel) NC-FSK performance. At certain (saturated) level of data rate we obtain the best system performance at a specific modulation order and channel, any further decrease in the data rate beyond that level won't further enhance the performance of the communication system. For modulation order M=8, when the T_{sym} = 800 ns and bit rate R_b=3.75 Mbps for instance, the required E_b/N_0 to satisfy a BER of 10^{-3} is only 2 dB from the analytical AWGN channel performance of NC-8 FSK. As we increase the symbol time to T_{sym} =1600 ns the system performance is almost identical. As is well known, this improved performance comes at the expense of a smaller data rate.

5.10.2 EXAMPLE (2): NC-128 FSK Performance in LOS / Micro-Urban. To test the performance of NC-MFSK for higher modulation order and see the effect on the

performance, we simulated transmission of NC-128 FSK over a channel generated by the NYUSIM channel simulator whose power delay profile is shown in Figure 5.7.

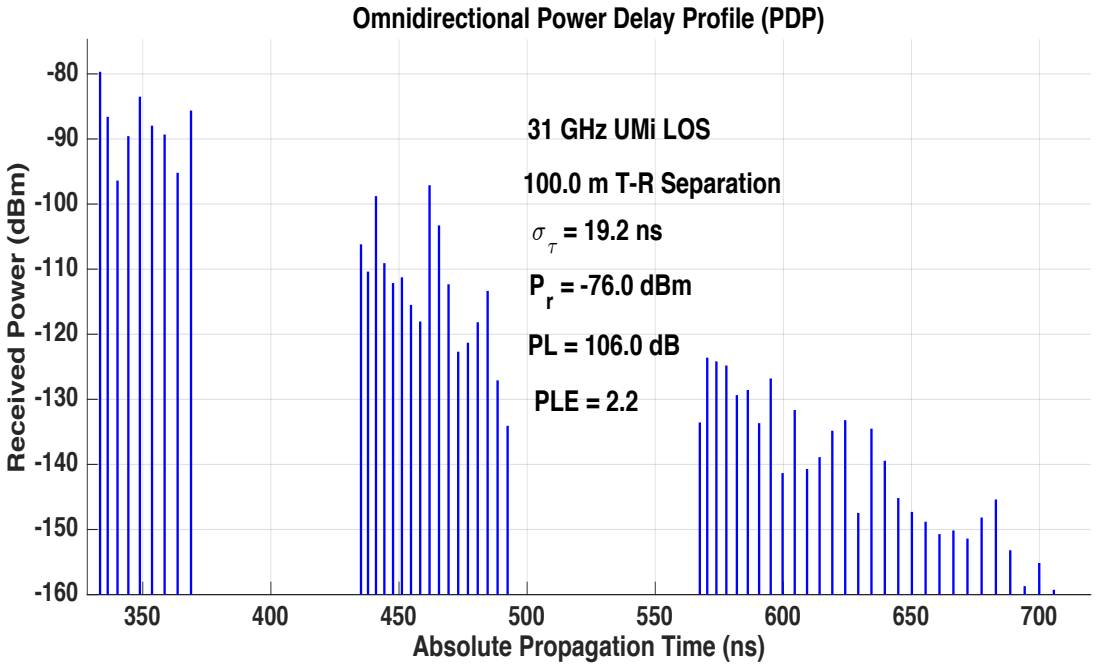

Figure 5.7 Example (2) Power Delay Profile (PDP) generated by NYUSIM for UMi LOS channel.

Our transmitted signal over this LOS channel assumes a link distance of 100 meter and R.M.S. delay spread σ_τ =19.2 ns, with PLE=2.2. In this example the Tx-Rx separation distance is much smaller than that of example 1 (where it was 1 km). This channel has a smaller path loss. Also, the channel has a larger number of clusters and a larger time gap between clusters due to change of the environment topology. Table 6.3 contains the transmit signal parameters for this case.

Table 5.3 Transmit signal parameters for NC-128FSK.

Transmitter setting					
M	BW(MHz)	Δf (MHz)	R_s (Msps)	R_b(Mbps)	T_{Sym}(ns)
128	533-1600	533-1600	4.1-12.5	28.7-87.5	80-240

The required bandwidth BW would be large for 128 tones with appropriate frequency separation Δf (533-1600 MHz) for a symbol rate ranging from 4.1 to 12.5 Msps, so it is hard to obtain a flat channel response for 128 FSK because the bandwidth would be larger than this channel's coherence bandwidth, unless data rate were made unattractively small (e.g., ~tens of kbps). All the channels that were generated according to Table 6.3 parameters are frequency selective for the data rates we use, but the smaller the band width the better the performance. This is because at the large value of M=128 the bandwidth must be large because of the separation frequency required between sequential tones.

In Figure 5.8 the σ_τ is in the range of 19 ns which is small (open urban area) compared to the T_{sym} = 80 ns obtained from the BW = 1.6 GHz Thus, it is reasonable to expect a flat-fading channel model. Under the above considerations, the channel model between the transmitter and the receiver is assumed to be flat-fading with path-loss. We still see for some portions of the transfer function there are spectral nulls of depth up to ~30 dB. For any given tone's spectra, the channel *is* frequency flat, but the difference in tone amplitudes would require equalization to compensate. We still see the effect of the channel frequency selectivity in Figures 5.8, 5.10, and 5.11 even when we increase the symbol time.

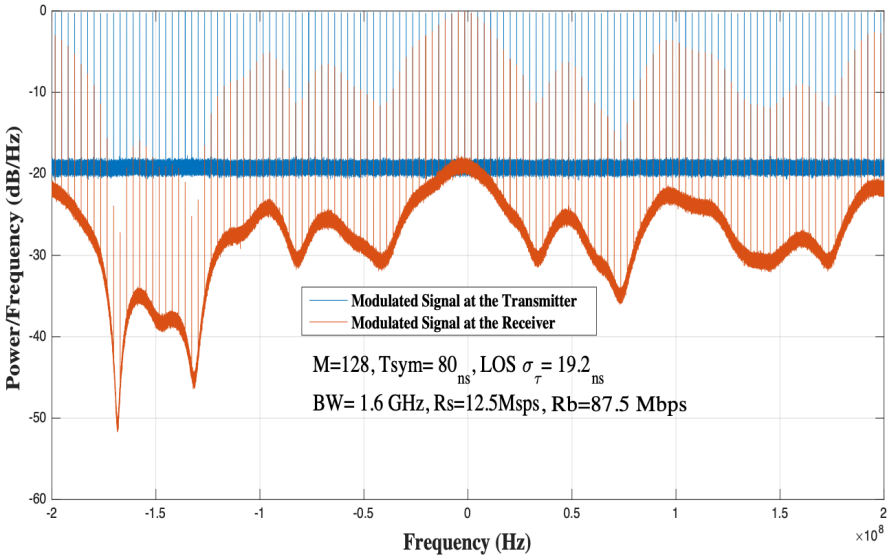

Figure 5.8 Power Spectrum of NC-128FSK transmitted and received signal, T_{sym}=80 ns, R_b=87.5 Mbps.

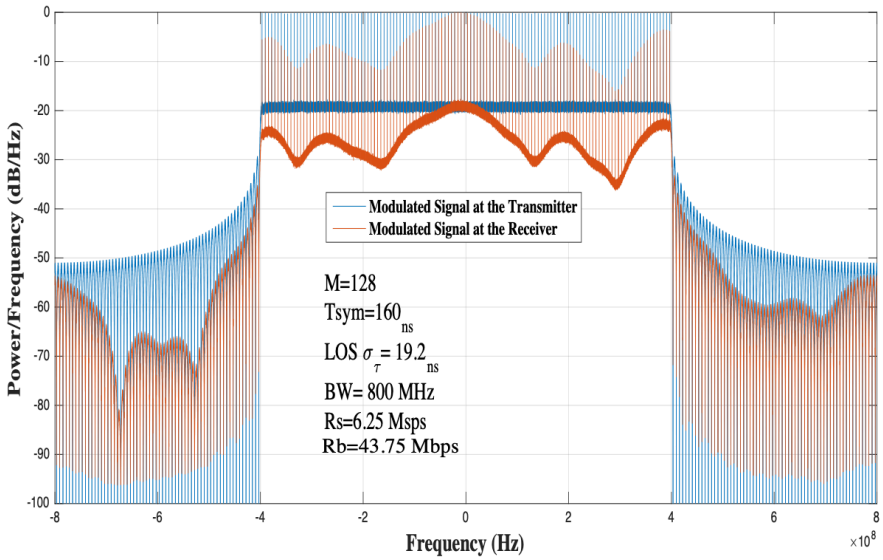

Figure 5.9 Power Spectrum of NC-128FSK transmitted and received signal, T_{sym}=160 ns, R_b=43.75.

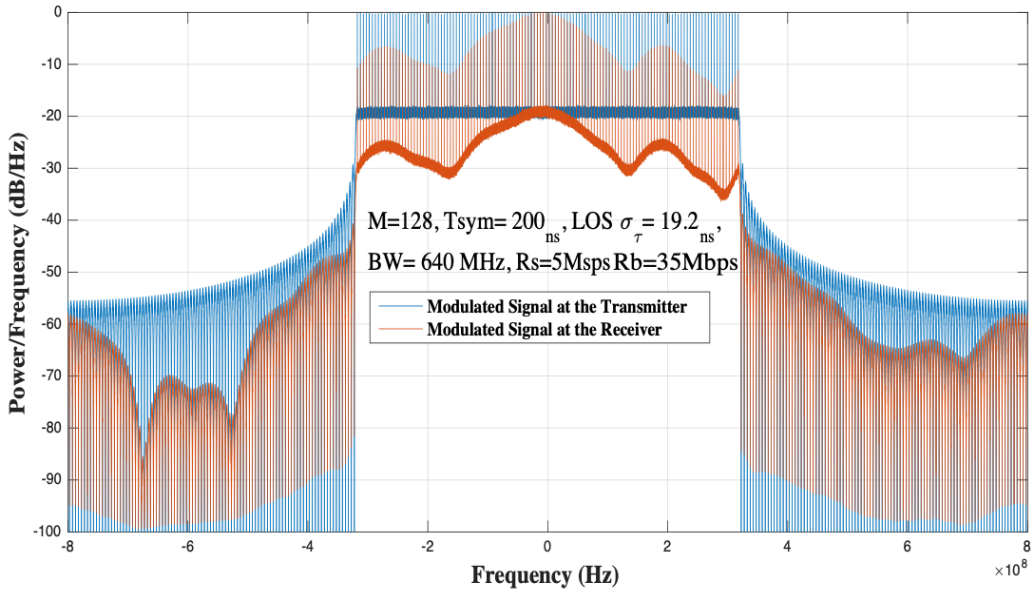

Figure 5.10 Power Spectrum of NC-128FSK transmitted and received signal, T_{sym}=200 ns, R_b=35Mbps.

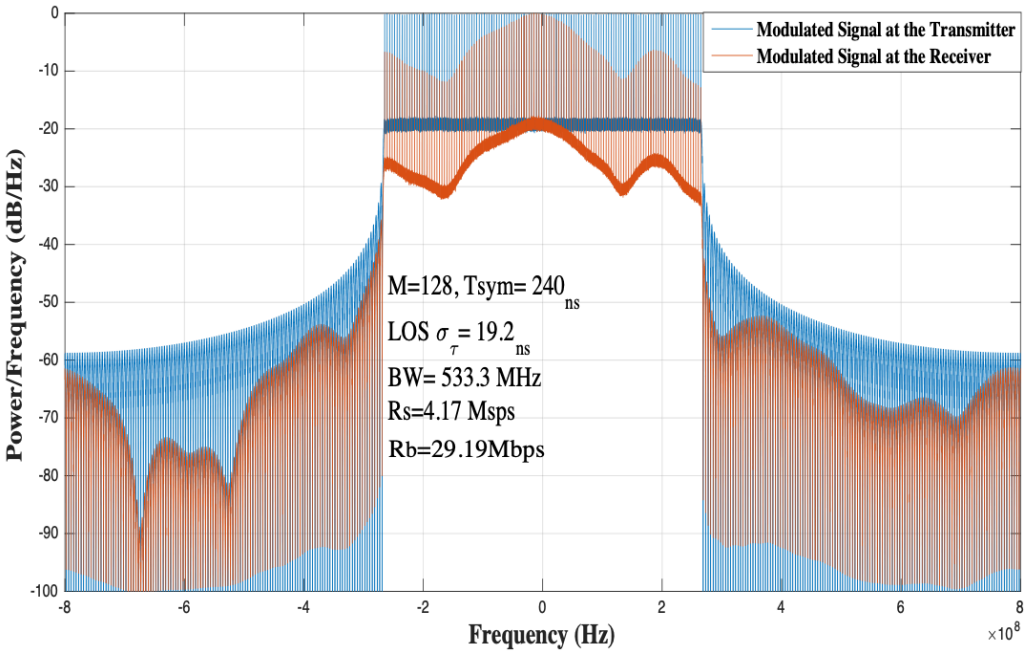

Figure 5.11 Power Spectrum of NC-128FSK transmitted and received signal, T_{sym}=240 ns, R_b=29.19 Mbps.

For any M-ary orthogonal scheme, the required E_b/N_0 for a given probability of error decreases as M increases without the need for multi-symbol coherent detection. In fact, as M approaches infinity the required E_b/N_0 decreases asymptotically to the Shannon limit of −1.6 dB [78]. In this example, where the modulation order is much higher than the one used in the first example, we expect to see a decrease in the required E_b/N_0 to reach to the required BER. However, this decrease is slow with increasing M, and extremely large values are impractical because of the increase in required bandwidth.

Figure 5.12 shows the BER vs. SNR performance of the NC-128FSK schemes of Figures 5.8-5.11 over the LOS millimeter channel with RMS-DS σ_τ=19.2 ns. As the symbol time increases, the BER decreases. For the largest symbol time (240 ns, with bit rate R_b=29.167 Mbps) the BER curve is about 4 dB more than the analytical AWGN channel BER for NC-128FSK at BER=10^{-3}.

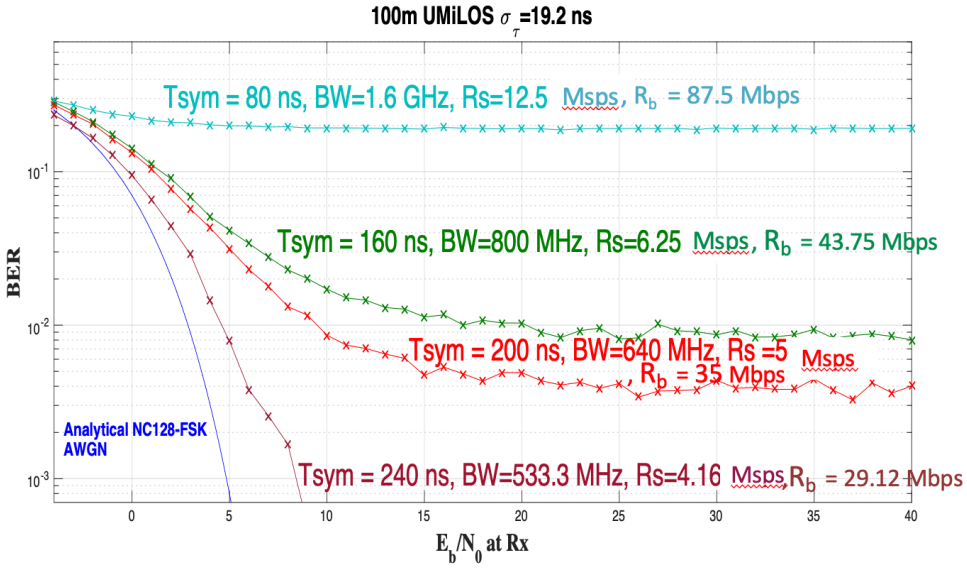

Figure 5.12 NC-128FSK system performance over LOS Micro-Urban channel for different symbol times.

5.11 BANDWIDTH-POWER EFFICIENCY TRADE-OFF IN NC-MFSK

In power-limited systems with ample bandwidth, the following trade-offs afford a reliable communication channel with a reasonable data rate for a target BER and a limited power budget. The trade-offs that can improve the performance are as follows:

1) Improve (reduce) the P_b at the expense of bandwidth for a fixed transmit power P_T.

2) Reduce P_T at the expense of bandwidth for fixed P_b.

In design of a digital communication system, very often there is a tradeoff between bandwidth efficiency and power efficiency. For any modulation, except MFSK, higher level modulation schemes (M-ary keying), decrease bandwidth occupancy but increase the required received power (reduce power or energy efficiency).

As noted, FSK modulation systems can offer a high bit rate at the expense of bandwidth. On the other hand, historically the maximum signal bandwidth in wireless communication is about 5% of the carrier frequency [80]. Therefore, the higher the carrier frequency, the greater the signal bandwidth. The 31 GHz band can provide an available spectrum bandwidth of up to 1.5 GHz or more. Considering this fact, it possible to increase the data throughput using FSK.

As bandwidth is increased, eventually the channel becomes dispersive, and this manifest itself as frequency selectivity across the M tones. This could be alleviated with equalization, or by the careful selection of subbands that carry smaller M-ary FSK signals in parallel.

5.12 ADAPTIVE MODULATION ORDER SYSTEMS

Adaptive modulation means dynamically varying the modulation in order to maximize the throughput in response to channel conditions. In other words, a system can

operate at its maximum throughput under “clear sky” conditions and decrease it gradually under fading or dispersion or interference. This is usually considered an acceptable trade-off and is used in modern cellular and WiFi systems. The main idea here is to take advantage of the reduction in BER with M of MFSK modulation. Based on the feedback channel status, the transmitter adapts its modulation level to get the targeted BER, and an achievable rate of transmission.

The idea of providing channel feedback to enable the transmission to keep track of the channel status was first proposed in the late 1960’s [81]. The adaptation technique takes a range of forms: maintaining a constant signal to noise ratio (SNR) by varying the transmitted power level, varying the symbol transmission rate, varying the modulation scheme constellation size, or any combination of these or other parameters [82]. Modern systems also vary the FEC code rate as well.

Unlike the fixed or “blind” modulation, which has no feedback information, in the adaptive modulation order system a feedback channel is required to inform the transmitter about the received signal condition (e.g., BER). Figure 5.13 shows the principle behind adaptive modulation, which is simple: transmit at as high a data rate as possible when the channel is good, and at a lower rate when the channel is poor, thus limiting the number of dropped packets and maintaining a target BER.

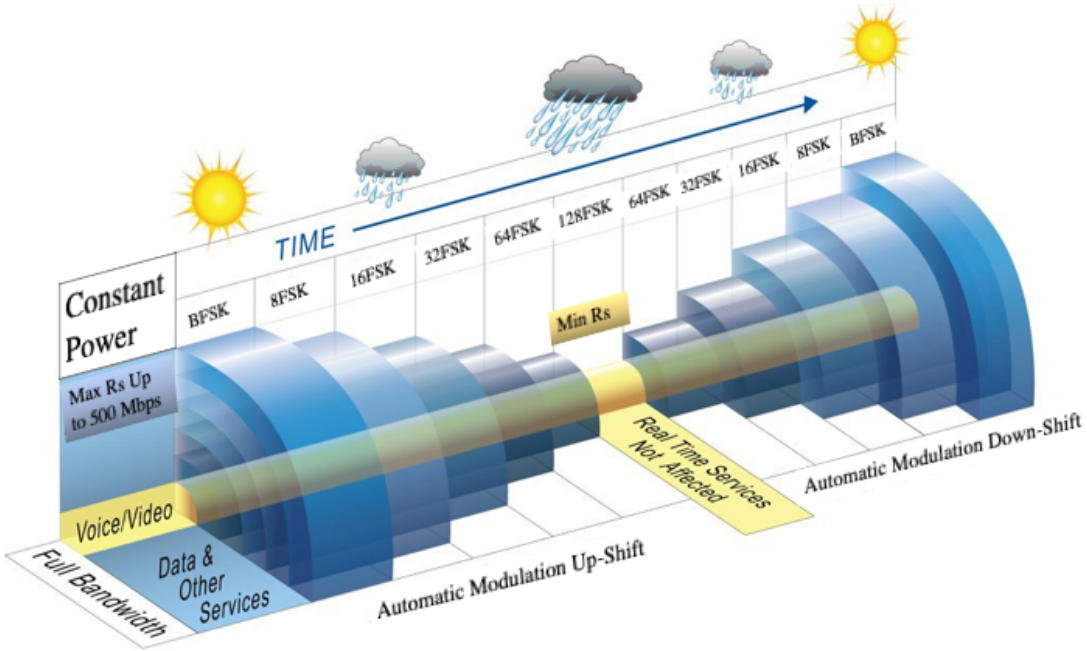

Figure 5.13 BER vs. throughput trade-offs for fixed BW system.

Adaptive modulation order could be a successful solution for some applications, where the main concern is to provide the maximum possible coverage while maintaining a reasonable transmission rate and target BER. A variable-rate and low-power NC-MFSK modulation scheme for power limited systems over mmWave fading channels could be desirable for this kind of applications and could alleviate the poor performance of the FSK over frequency-selective fading channels. By matching the modulation order to the conditions on the radio link (e.g., the pathloss, the interference, the sensitivity of the receiver, the available transmitter power margin, etc.) we get an acceptable bit rate and robust data transmission.

The effect of the modulation order on the system performance was clearly shown in Examples (1) and (2) in section 5.10.1 and section 5.10.2. Figure 5.4 showed that for a modulation order of 8 and for T_{sym}=80 ns, the throughput would be only 3.75 Mbps, but the

performance was acceptable even over a frequency-selective channel. The power spectrum of the received signal showed clearly identifiable tones with different relative power levels but still acceptable performance. On the other hand when M=128, Power Spectrum in figure 5.8 of NC-128FSK transmitted and received signal for the same T_{sym}=80 ns, the throughput would much larger, R_b=87.5 Mbps, but we would see for some portions of the transfer function there are spectral nulls of depth up to ~30 dB for the received signal spectrum.

Adaptive modulation is a technique to get the maximum possible data rate that can be reliably transmitted over fading channels. Thus, without wasting power or sacrificing BER, adaptive modulation schemes provide a higher average link spectral efficiency (bps/Hz) by adapting to fading.

In addition to changing transmission parameters to adapt to channel conditions, one might also allow some variation in the target BER. The question ultimately arises as to which of these parameters should be adapted to obtain the desired performance. We assume that the resulting adaptive modulation schemes are subject to an average power and BER constraint. So, in the next examples we focus on changing the data rate by changing the modulation depth without significantly changing BER.

Good performance of adaptive modulation requires accurate channel estimation at the receiver and a reliable feedback path between the receiver and transmitter. So other assumptions are that the network control entity obtains an accurate channel estimate from the receiver, and the impact of estimation error and feedback delay on adaptive modulation schemes are negligible.

Example (1): NC-MFSK performance over section 6.4.1's transmission channel generated via the NYUSIM channel simulator, with RMS delay spread equal to 67ns. Our target BER is 0.01, and the adaptive parameters signal alphabet size (M), bandwidth, and data rate can be changed to achieve the best system performance to maintain that performance as channel conditions change.

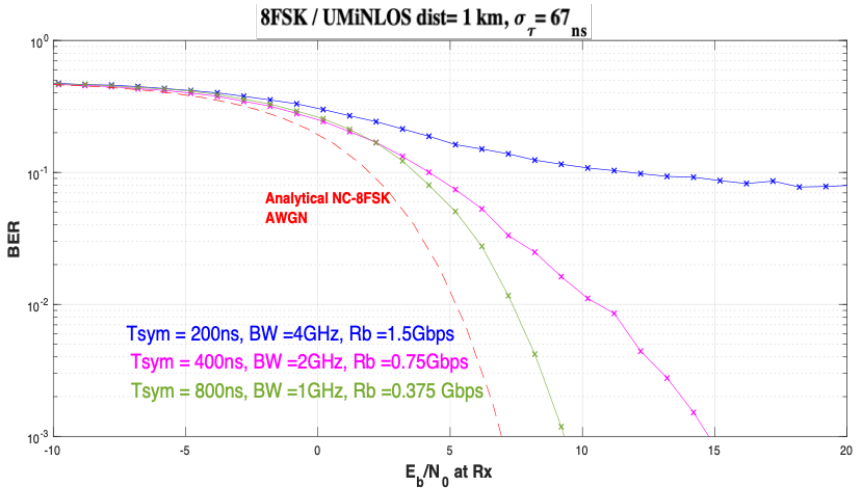

Figure 5.14 NC-8FSK system performance over LOS Micro-Urban channel for different data rate.

Figure 5.14 shows the expected required signal energy for different data rates when the modulation order M=8 for a 1 km link range. There are two cases shown that satisfy our target value of BER, the first when R_b= 0.75 Gbps, with required Eb/N0 =10.6 dB, and the second case is when Rb=0.375 Gbps, with required Eb/N0 =7.6 dB. For both cases in this example, any further increase in the value of Eb/N0 would of course guarantee more reliable system performance (retransmitting fewer packets) but larger SNR won't enable higher data rate. We would need to increase modulation order to get higher data rate for these same channel conditions, as we see in the next example.

Figure 5.15 shows NCFSK system performance for higher modulation order M=32 over the same channel as example (1). With BER restriction of 0.01, the maximum data rate that we can obtain is 1.25 Gbps and the required Eb/N0 is 17.1 dB. For lower Eb/N0 of 14 dB we can get data rate up to 0.625 Gbps.

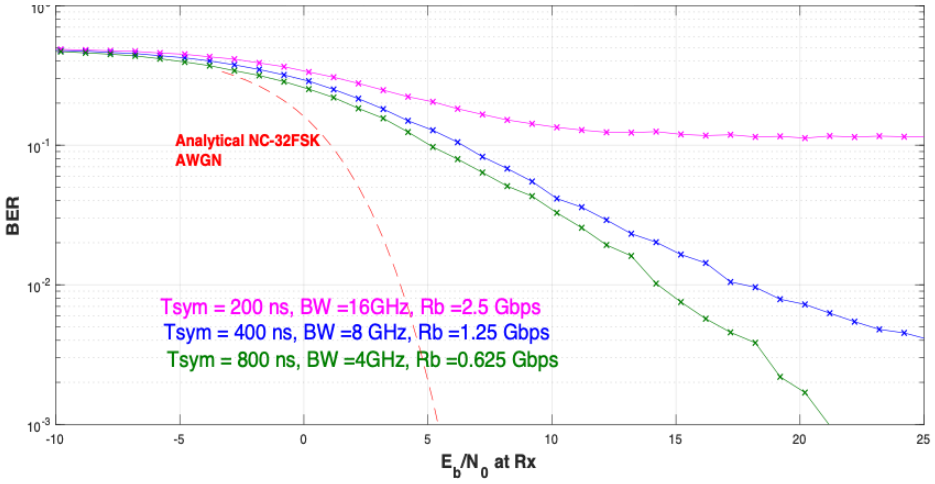

Figure 5.15 NC-32FSK system performance over LOS Micro-Urban channel for different data rate.

Our simulation results illustrate, as expected, that over a given channel condition, higher data rate requires an increase in the modulation order, and any increase in the transmitted power makes the system more reliable (lower value of BER). Figure 5.16 shows the maximum data rate for three candidate modulation orders M=8, 32, and 128 and the required power for each case to satisfy the BER value of 0.01. When M=8 the Rb=0.625 Gbps, and minimum Eb/N0=7 dB; when M=32, the maximum data rate is 0.625 Gbps, with required Eb/N0=10.1 dB, and when M= 128, Rb= 0.875 Gbps for Eb/N0 17 dB.

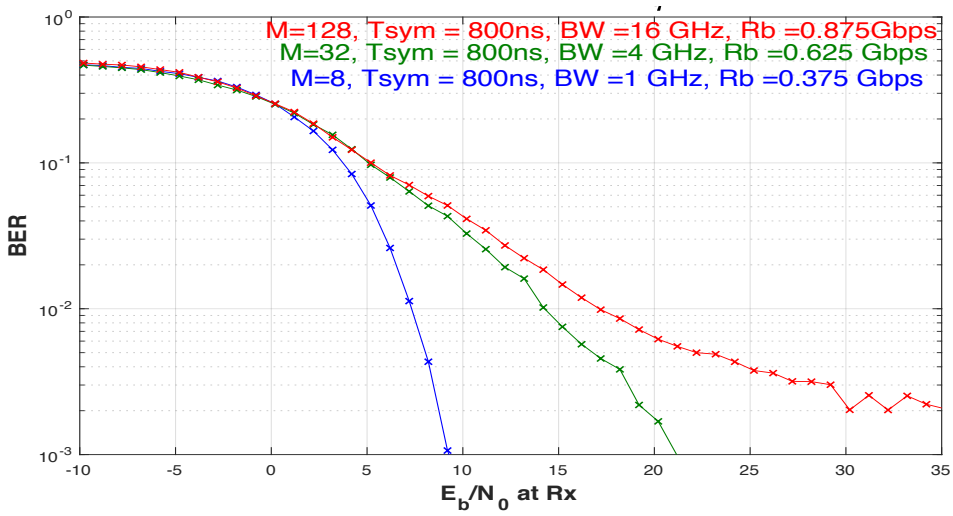

Figure 5.16 NC-8, 32, 128FSK system performance over LOS Micro-Urban channel.

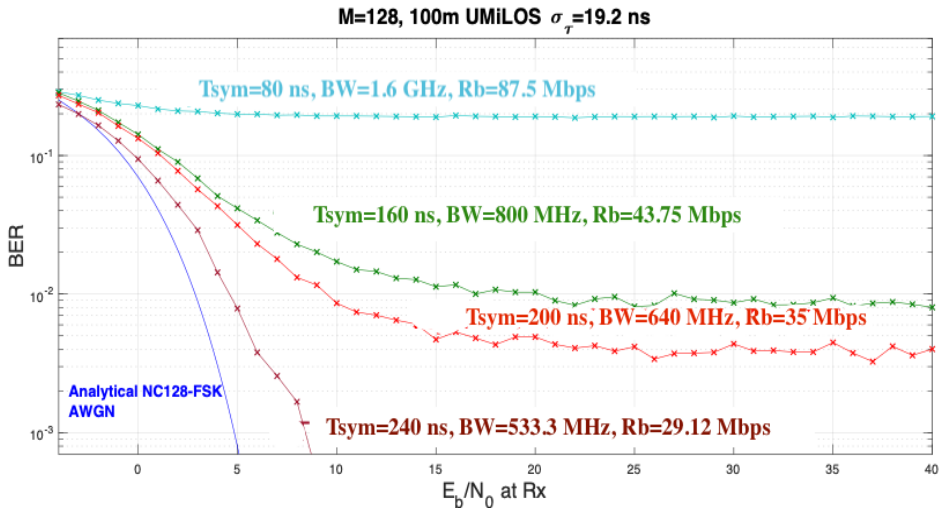

Figure 5.17 NC-128FSK system performance over LOS Micro-Urban channel.

Example (2): NC-MFSK performance over section 6.4.2's transmission channel generated using the NYUSIM channel simulator. The target BER is still 0.01. The RMS delay spread for this channel is σ_τ =19.2 ns, smaller than that of Example (1), hence this is a relatively better channel.

Figure 5.17 shows the simulation results of NC-128 FSK over this channel for different symbol durations and different corresponding data rates. Using candidate system configurations of Tsym= 200 ns and Tsym= 240 ns that will provide Rb=35 Mbps and 29.12 Mbps, respectively, would be good trade-off options between the data rate and Eb/N0 since the first option requires Eb/N0=9.2 dB and the second requires Eb/N0= 4.6 dB.

Figure 5.18 shows the results of simulating NC- 8, 32, 128 FSK over the same example channel. Here we have a more stringent BER performance requirement of BER= 0.001. The selection of Rb=312.5 Mbps for the 32 FSK scheme is a good choice since it meets the BER requirement and provides a larger data rate than the M=8 option.

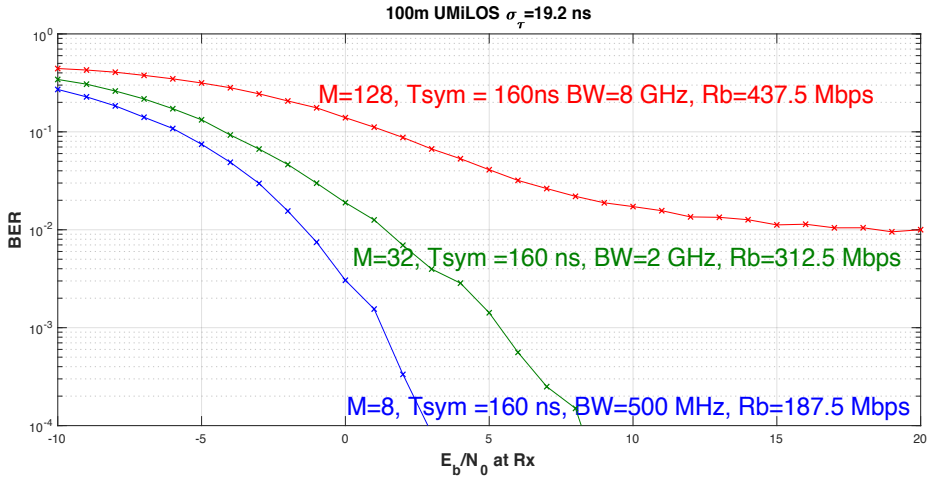

Figure 5.18 NC-128FSK system performance over LOS Micro-Urban channel for different BW.

CHAPTER 6

CONCLUSIONS AND FUTURE WORK

In this dissertation, we have investigated the potential of using a new waveform for mmWave systems. This waveform, NC-FSK, has been used in some applications in the past, but has characteristics that make it particularly suitable for very wideband channels available in the mmWave bands. Path loss measurement and modeling for the 30 GHz band has also been presented in this work. Furthermore, vegetation attenuation at cm/mmWave frequencies has been investigated and specified in terms of specific attenuation dB/m, for several evergreen shrubs. In this chapter, the main conclusions and discussion of avenues for future research for academia and industry are presented.

6.1 DISSERTATION CONCLUSIONS

The main objective of our research was to study the mmWave propagation characteristics and challenges and evaluate a proposed waveform for a specific mmWave-band system.

1. Path Loss Measurements and Modeling

    - Several 30 GHz path loss models have been presented in this work. Results show that floating-intercept reference large-scale path loss models in our study might look better than the close-in (CI) reference distance models

because they often yield a smaller value of standard deviation. Yet the reduction in the standard deviation is only a fraction of a dB (average of 0.4 dB for the co-polarization cases) compared to the simpler, physically-based CI model. That is, the improvement in error with the more complex two-parameter FI model is typically insignificant, so we recommend use of our CI models.

- The CI path loss models showed that for co-polarization antenna configuration, the PLEs for both outdoor frontcourt and indoor corridors have values less than that of free space, i.e., less than two. For the corridors, this means that waveguiding effects occur, as expected. The NLOS scenario showed a higher attenuation and higher depolarization than the LOS scenario, also as expected. The simple CIX path loss model was used to effectively model path loss for the cross-polarized antenna configuration. The XPD factor was calculated for this model in the indoor LOS environment as 20 dB, and that is comparable to the value that has been calculated in [31], equal to 12 dB at 28 GHz in LOS indoor environment and comparable to XPD value of [32], equal to 23.8 dB and 14.6 dB at 73 and 28 GHz, respectively, for an LOS corridor environment using omnidirectional antennas.

2. Vegetation Attenuation

- Radio wave attenuation and depolarization effects through three broadleaf evergreen shrubs were reported, based upon measurements at two

frequencies, 5 and 31 GHz. The vegetation attenuation of the shrubs was presented in terms of specific attenuation in dB/m.

- The measured specific attenuation is very large, at least 15 dB/m, and up to 24 dB/m for the densest shrub. As would be expected, the higher the density of shrub branches and foliage, the larger the specific attenuation. These results will be useful for link budget design, and outdoor and outdoor-indoor models for future mmWave communication.
- Results emphasized the importance of careful measurement geometry in signal propagation studies to ensure that measurement results truly represent the intended effect. Measurement procedures also must be taken into account in the interpretation of the results. We have shown that measurement geometry; specifically, the distance from the directional antenna(s) to the shrub can substantially affect the estimate of specific attenuation as additional multipath components can reach the receiver; specific attenuation measured in this way decreases as the antennas are moved away from the shrub.
- The study has confirmed that there is a strong frequency dependence of signal attenuation by vegetation, with high frequencies experiencing more attenuation than low frequencies.

3. NC-FSK for the mmWave Channel

- We proposed a signaling scheme design for the mmWave channel based on NC-FSK. Our investigation employed simulations, and based upon

empirical channel models, we investigated performance in terms of BER. For relatively small modulation order M=8, a channel with R.M.S delay spread σ_τ=67 ns is flat-fading when the symbol time of the transmitted signal T_{sym}=1280 ns, much greater than σ_τ. This system yields R_b~2.34 Mbps. The same channel becomes frequency-selective when the symbol time is reduced to 80 ns, comparable to σ_τ, at the same modulation level. Our result showed that unless data rate is very small, it is hard to obtain a flat channel response for relatively higher modulation level, e.g., NC-128FSK, because the bandwidth would be larger than this channel's coherence bandwidth.

- FSK as a constant envelope modulation scheme offers, particularly using its high order and non-coherent version, a high data rate and low complexity and low-cost hardware implementation. It also has several other features that were described in this dissertation that make NC-FSK a good choice for specific future mmWave applications that required a simple, flexible design, low cost equipment and battery constrained (low energy) devices. A typical example is the collection of the measurements from a massive number of sensors, such as smart metering. The results showed that our NC-FSK design could have a low BER comparable to that on the AWGN channel for relatively small M and $T_{sym}>>\sigma_\tau$ However, our simulation results for relatively large band width (BW=533-1600 MHz) showed that this scheme will suffer from ISI due to the large bandwidth.

6.2 FUTURE WORK

Possible extensions of this dissertation work are listed next:

1. FSK without equalizers is a low complexity scheme. However, to further improve performance and enable even larger data rates for 5G communication networks, receiver enhancement techniques should be investigated. These include equalization, adaptive modulation order, and antenna diversity. Evaluating uncoded symbol error probability performance is typically sufficient but use of FEC encoding and decoding should also be applied to evaluate application performance, at least for several key applications. Use of our propagation path loss and vegetation attenuation models can be combined with the dispersive channel simulator (NYUSIM).

2. Apply MIMO through the NYUSIM simulations to further improve performance and 5G capacity.

3. To evaluate the modulation scheme in various scenarios of 5G users, we need to simulate our system not only for the pedestrian user scenario but also should investigate other user mobility conditions, e.g., vehicular.

4. Conduct a wideband NC-FSK signaling measurement for different scenarios to provide a ground truth measurement that can calibrate and verify the simulation results of the NC-FSK performance for wideband signals.

5. Try new techniques to alleviate the ISI problem of wideband high order NC-FSK systems, e.g., emulate an FSK multicarrier transmission, in which a wideband signal is created from a number of narrow band M-ary FSK signals. That number

would be determined by the amount of the available bandwidth and the channel status. Gain compensation across the sub-bands would be required, but each subband would be designed to experience flat fading.

6. Wideband measurements to quantify the vegetation attenuation and penetration loss for different materials could be made. In contrast with the narrow band measurement, wideband measurements enable us to distinguish between any reflected components and the direct attenuated signal component that passes through the MUT.

REFERENCES

[1] Communication from the commission to the European parliament, the council, the European economic and social committee and the committee of the regions, *Communication from the Commission to the Institutions*, 02/06/2016.

[2] Resolution Com6/20, Provisional Final Acts WRC-15. WRC-15 (pp. 424-426). Geneva: ITU. http://www.itu.int/dms_pub/itu-r/opb/act/R-ACT-WRC.11-2015-PDF-E.pdf.

[3] IMT 2020 https://www.itu.int/dms_pubrec/itu-r/rec/m/R-REC-M.2083-0-201509-I!!PDF-E.pdf.

[4] CISCO VNI 2016: http://www.cisco.com/c/en/us/solutions/collateral/service-provider/visual-networking-index-vni/mobile-white-paper-c11-520862.html.

[5] T. S. Rappaport, J. N. Murdock and F. Gutierrez, "State of the Art in 60-GHz Integrated Circuits and Systems for Wireless Communications," in *Proceedings of the IEEE*, vol. 99, no. 8, pp. 1390-1436, Aug. 2011.

[6] 5G Candidate Band Study Study on the Suitability of Potential Candidate Frequency Bands above 6GHz for Future 5G Mobile Broadband Systems, 2015. https://www.ofcom.org.uk/__data/assets/pdf_file/0014/31910/qa-report.pdf.

[7] T. S. Rappaport, G. R. MacCartney, Jr., M. K. Samimi, and S. Sun, “Wideband millimeter-wave propagation measurements and channel models for future wireless communication system design” *IEEE Trans. Comm.*, vol. 63, no. 9, pp. 3029_3056, Sep. 2015.

[8] International Telecommunications Union, ‘Compilation of measurement data relating to building entry loss’, 2016. [Online]. Available: https://www.itu.int/dms_pub/itu-r/opb/rep/R-REP-P.2346-1-2016-PDF-E.pdf.

[9] Ofcom.org.uk,2019. [Online]. Available: https: //www.ofcom.org.uk/ data/assets/pdf_ file / 0014/31910/qa-report.pdf

[10] T. S. Rappaport et al., “Millimeter Wave Wireless Communications”, 1st Edition, Prentice Hall,2015.

[11] T. S. Rappaport, S. Sun, R. Mayzus, H. Zhao, Y. Azar, K. Wang, G. N. Wong, J. K. Schulz, M. K. Samimi, and F. Gutierrez, Jr., “Millimeter Wave Mobile Communications for 5G Cellular: It Will Work!” *IEEE Access*, vol. 1, pp. 335–349, May 2013.

[12] T. S. Rappaport, R. W. Heath, Jr., R. C. Daniels, and J. N. Murdock, *Millimeter Wave Wireless Communications*, Pearson/Prentice Hall, 2015.

[13] M. K. Samimi, T. S. Rappaport, and G. R. MacCartney, Jr., “Probabilistic omnidirectional path loss models for millimeter-wave outdoor communications,”IEEE Wireless Communications Letters, vol. 4, no. 4, pp. 357–360, Aug.2015.[Online].Available:http://ieeexplore.ieee.org/xpl/articleDetails.jsp?arnumber=7070688

[14] M. K. Samimi and T. S. Rappaport, “3-d statistical channel model for millimeter-wave outdoor communications,” I*EEE International Conference on Communications (ICC)*, June 2015. [Online]. Available:http: //arxiv.org/abs/1503.05619.

[15] “Local multipath model parameters for generating 5g millimeter-wave 3gpp-like channel impulse response,” 10th European Conference on Antennas and Propagation (EuCAP 2016), Apr. 2016. [Online]. Available: http://arxiv.org/abs/1511.06941.

[16] K. Haneda *et al*., "5G 3GPP-Like Channel Models for Outdoor Urban Microcellular and Macrocellular Environments," *2016 IEEE 83rd Vehicular Technology Conference (VTC Spring)*, Nanjing, 2016, pp. 1-7.

[17] Dahlman, Erik, et al. *5G NR: the next Generation Wireless Access Technology*. Elsevier Ltd, 2018.

[18] C. Bockelmann, H. Schepker and A. Dekorsy, "Compressive Sensing based Multi-User Detection for Machine-to-Machine Communication," Transactions on Emerging

Telecommunications Technologies: Special Issue on Machine-to Machine: An emerging communication paradigm, vol. 24, no. 4, pp. 389-400, June 2013.

[19] A. Lizeaga, P. Rodríguez, I. Val and M. Mendicute, "Evaluation of 5G Modulation Candidates WCP-COQAM, GFDM-OQAM, and FBMC-OQAM in Low-Band Highly Dispersive Wireless Channels," *Journal of Computer Networks and Communications*, vol. 2017, pp. 1-11, 2017. Available: 10.1155/2017/2398701.

[20] M. Alhasani, Q. Nguyen, G. Ohta and T. Sato, "A Novel Four Single-Sideband M-QAM Modulation Scheme Using a Shadow Equalizer for MIMO System Toward 5G Communications", *Sensors*, vol. 19, no. 8, p. 1944, 2019. Available: 10.3390/s19081944.

[21] S. Wu, Y. Wang, M. Al-Imari and M. Nekovee, "Frequency and quadrature amplitude modulation for 5G networks", *2016 European Conference on Networks and Communications (EuCNC)*, 2016. Available: 10.1109/eucnc.2016.7560993 [Accessed 4 November 2019].

[22] C. An and H. Ryu, "Design and Performance Evaluation of OTFS Modulation System using 2D iDFT and DFT", *Journal of the Institute of Electronics and Information Engineers*, vol. 54, no. 9, pp. 14-20, 2017. Available: 10.5573/ieie.2017.54.9.14.

[23] S. Sun et al., "Propagation Path Loss Models for 5G Urban Micro- and Macro-Cellular Scenarios", *IEEE 83rd Vehicular Technology Conference (VTC Spring)*, 2016. Available: 10.1109/vtcspring.2016.7504435 [Accessed 4 November 2019].

[24] G. MacCartney, Junhong Zhang, Shuai Nie and T. Rappaport, "Path loss models for 5G millimeter wave propagation channels in urban microcells", *IEEE Global Communication Conference (GLOBECOM), 2013.*

[25] M. Majed, T. Rahman, O. Aziz, M. Hindia and E. Hanafi, "Channel Characterization and Path Loss Modeling in Indoor Environment at 4.5, 28, and 38 GHz for 5G Cellular Networks", *International Journal of Antennas and Propagation*, vol. 2018, pp. 1-14, 2018. Available: 10.1155/2018/9142367.

[26] M. Al-Nuaimi and R. Stephens, "Measurements and prediction model optimisation for signal attenuation in vegetation media at centimetre wave frequencies", *IEE Proceedings - Microwaves, Antennas and Propagation*, vol. 145, no. 3, p. 201, 1998. Available: 10.1049/ip-map:19981883.

[27] Jones, David L.," Vegetation loss measurements at 9.6, 28.8, 57.6, and 96.1 GHz through a conifer orchard in Washington State", *U.S. Dept. of Commerce, National Telecommunications and Information Administration,* vol. 145, October 1989.

[28] T. Rappaport and S. Deng, "73 GHz wideband millimeter-wave foliage and ground reflection measurements and models", *2015 IEEE International Conference on Communication Workshop (ICCW)*, 2015. Available: 10.1109/iccw.2015.7247347 [Accessed 4 November 2019].

[29] Meza C.A, Kyujin Lee, Kyesan Lee, 2011, "PAPR reduction in single carrier FDMA uplink system using parametric linear pulses", *ICT Convergence (ICTC), International Conference*, pp.422-429.

[30] T. Abbas, F. Qamar, I. Ahmed, K. Dimyati, and M. B. Majed, "Propagation channel characterization for 28 and 73 GHz millimeter-wave 5G frequency band," in *2017 IEEE 15th Student Conference on Research and Development (SCOReD)*, pp. 297–302, Putrajaya, Malaysia, December 2017.

[31] Maccartney, George R., et al. "Indoor Office Wideband Millimeter-Wave Propagation Measurements and Channel Models at 28 and 73 GHz for Ultra-Dense 5G Wireless Networks," *IEEE Access,* vol. 3, 2015, pp. 2388–2424.

[32] Batalha, Iury S., et al. "Large-Scale Channel Modeling and Measurements for 10 GHz in Indoor Environments." *International Journal of Antennas and Propagation*, vol. 2019, 2019, pp. 1–10., doi:10.1155/2019/9454271.

[33] K. Haneda et al., "5G 3GPP-like Channel Models for Outdoor Urban Microcellular and Macrocellular Environments," *Vehicular Technology Conference (VTC 2016-Spring)*, *IEEE*, May, 2016.

[34] S. Sun *et al*., "Propagation Path Loss Models for 5G Urban Micro- and Macro-Cellular Scenarios," *2016 IEEE 83rd Vehicular Technology Conference (VTC Spring)*, Nanjing, 2016, pp. 1-6.

[35] E. Oughton and Z. Frias, "The cost, coverage and rollout implications of 5G infrastructure in Britain", *Telecommunications Policy*, vol. 42, no. 8, pp. 636-652, 2018. Available: 10.1016/j.telpol.2017.07.009.

[36] S. Sun et al.," Investigation of Prediction Accuracy, Sensitivity, and Parameter Stability of Large-Scale Propagation Path Loss Models for 5G Wireless Communications," *IEEE Transactions on Vehicular Technology*, vol. 65, no. 5, pp. 1-18, May 2016.

[37] A. Al-Samman, T. Rahman, M. Azmi, M. Hindia, I. Khan and E. Hanafi, "Statistical Modelling and Characterization of Experimental mm-Wave Indoor Channels for Future 5G Wireless Communication Networks", *PLOS ONE*, vol. 11, no. 9, p. e0163034, 2016.

[38] A. F. Molisch, *Wireless Communications,* John Wiley & Sons, Upper Saddle River, NJ, 2010.

[39] S. Sun, G. R. MacCartney, Jr., and T. S. Rappaport," Millimeter-Wave Distance-Dependent Large-Scale Propagation Measurements and Path Loss Models for Outdoor and Indoor 5G Systems," *10th European Conference on Antennas and Propagation (EuCAP 2016*), April. 2016.

[40] J. N. Murdock, E. Ben-Dor, Y. Qiao, J. I. Tamir, and T. S. Rappaport, ``A 38 GHz cellular outage study for an urban campus environment," *in Proc. IEEE Wireless Commun. Network. Conf.*, Paris, France Apr. 2012.

[41] Didascalou, D., et al. "Subway Tunnel Guided Electromagnetic Wave Propagation at Mobile Communications Frequencies," *IEEE Transactions on Antennas and Propagation*, vol. 49, no. 11, 2001, pp. 1590–1596., doi:10.1109/8.964095.

[42] T. S. Rappaport, G. R. MacCartney, Jr., M. K. Samimi, and S. Sun, ``Wideband millimeter-wave propagation measurements and channel models for future wireless

communication system design (invited paper)," *IEEE Trans. Comm*., vol. 63, no. 9, pp. 3029_3056, Sep. 2015.

[43] S. Geng, J. Kivinen, X. Zhao and P. Vainikainen, "Millimeter-Wave Propagation Channel Characterization for Short-Range Wireless Communications," in *IEEE Transactions on Vehicular Technology*, vol. 58, no. 1, pp. 3-13, Jan. 2009.

[44] C. R. Anderson and T. S. Rappaport, ``In-building wideband partition loss measurements at 2.5 and 60 GHz," *IEEE Trans. Wireless Communication,* vol. 3, no. 3, pp. 922_928, May 2004.

[45] T. Zwick, T. J. Beukema, and H. Nam, ``Wideband channel sounder with measurements and model for the 60 GHz indoor radio channel," *IEEE Trans. Vehicular Technology Conference*, vol. 54, no. 4, pp. 1266_1277, Jul. 2005.

[46] T. S. Rappaport, S. Deng, ”73 GHz Wideband Millimeter-Wave Foliage and Ground Reflection Measurements and Models,” *in 2015 IEEE International Conference on Communications (ICC), ICC Workshops*, 8-12 June 2015.

[47] Wang, Qi, et al. “Attenuation by a Human Body and Trees as Well as Material Penetration Loss in 26 and 39 GHz Millimeter Wave Bands.” *International Journal of Antennas and Propagation,* vol. 2017, 2017, pp. 1–8., doi:10.1155/2017/2961090.

[48] Nashashibi, A.y., et al. “Millimeter-Wave Measurements of Foliage Attenuation and Ground Reflectivity of Tree Stands at Nadir Incidence.” *IEEE Transactions on Antennas and Propagation*, vol. 52, no. 5, 2004, pp. 1211–1222., doi:10.1109/tap.2004.827250.

[49] Savage, Nick, et al. “Radio Wave Propagation through Vegetation: Factors Influencing Signal Attenuation.” *Radio Science*, vol. 38, no. 5, 2003, doi:10.1029/2002rs002758.

[50] Ndzi, D. L., Kamarudin, L. M., Ezanuddin, A. A. M., Zakaria, A., Ahmad, R. B., Malek, M. F. B. A., Jafaar, M. N. (2012). “Vegetation Attenuation Measurements And Modeling In Plantations For Wireless Sensor Network Planning.” *Progress In Electromagnetics Research* B, 36, 283–301. doi: 10.2528/pierb11091908

[51] Hanci, B.y., and I.h. Cavdar. “Mobile Radio Propagation Measurements and Tuning the Path Loss Model in Urban Areas at GSM-900 Band in Istanbul-Turkey.” *IEEE 60th Vehicular Technology Conference, 2004. VTC2004-Fall. 2004*, doi:10.1109/vetecf.2004.1399948.

[52] Y. S. Meng, Y. H. Lee, and B. C. Ng, "Study of propagation loss prediction in forest environment," *Progress In Electromagnetics Research B*, Vol. 17, 117-133, 2009.

[53] K. L. Chee, S. A. Torrico, and T. Kurner, "Radiowave Propagation Prediction in Vegetated Residential Environments," *IEEE Transactions on Vehicular Technology*, Volume: 62, Issue: 2, pp. 486 – 499, Feb. 2013

[54] A. O. Michael, "Further Investigation into VHF Radio Wave Propagation Loss over Long Forest Channel," *International Journal of Advanced Research in Electrical, Electronics and Instrumentation Engineering*, Vol. 2, Issue 1, January 2013.

[55] Savage, N., Ndzi, D., Seville, A., Vilar, E., & Austin, J. (2003). “Radio wave propagation through vegetation: Factors influencing signal attenuation.” *Radio Science*, *38*(5). doi: 10.1029/2002rs002758

[56] Rodriguez, I., Abreu, R., Almeida, E. P. L., Lauridsen, M., Loureiro, A., & Mogensen, P. (2016). “24 GHz cmwave radio propagation through vegetation: Suburban tree clutter attenuation.” *2016 10th European Conference on Antennas and Propagation (EuCAP)*. doi: 10.1109/eucap.2016.7481471

[57] *International Telecommunications Union – Radiocommunication* (ITU-R), Recommendation P.833-4, “Attenuation in vegetation”, 09/2016

[58] J. Ryan, G. R. MacCartney, Jr., and T. S. Rappaport, “Indoor Office Wideband Penetration Loss Measurements at 73 GHz,” *in 2017 IEEE International Conference on Communications Workshop (ICCW), Paris, France,* May 2017, pp. 1-6.

[59] Y. Xing, O. Kanhere, S. Ju, T. S. Rappaport, and G. R. MacCartney Jr., “Verification and calibration of antenna cross-polarization discrimination and penetration loss for millimeter wave communications,” *2018 IEEE 88th Vehicular Technology Conference (VTC2018-Fall),* Chicago, USA, Aug. 2018, pp. 1-6.

[60] T. S. Rappaport, Y. Xing, G. R. MacCartney, Jr., A. F. Molisch, E. Mellios, J. Zhang, "Overview of Millimeter Wave Communications for Fifth-Generation (5G) Wireless Networks-with a focus on Propagation Models," *in IEEE Transactions on Antennas and Propagation, Special Issue on 5G,* Nov. 2017

[61] Chávez-Santiago, R., Szydełko, M., Kliks, A. et al. Wireless Personal Communication (2015) 83: 1617.

[62] Gerzaguet, Robin, et al. "The 5G Candidate Waveform Race: a Comparison of Complexity and Performance." *EURASIP Journal on Wireless Communications and Networking*, vol. 2017, no. 1, Nov. 2017, doi:10.1186/s13638-016-0792-0.

[63] Abouei, Jamshid, et al. "Green Modulation in Dense Wireless Sensor Networks." *2010 IEEE International Conference on Acoustics, Speech and Signal Processing*, 2010, doi:10.1109/icassp.2010.5495986.

[64] Simon, Marvin K. *Bandwidth-Efficient Digital Modulation with Application to Deep-Space Communications*. Great Britain, 2003.

[65] Advantages of Constant Envelope Modulation, *http://sss-mag.com/cem.html*.

[66] What is RF Peak Envelope Power (PEP) *https://owenduffy.net/measurement/RfPowerTerms/PEP.htm.*

[67] Ott, Henry W. *Electromagnetic Compatibility Engineering*. Wiley, 2009.

[68] Abouei, J., et al. "Green Modulations in Energy-Constrained Wireless Sensor Networks." *IET Communications*, vol. 5, no. 2, 2011, pp. 240–251., doi:10.1049/iet-com.2010.0472.

[69] Hossain, Ekram, et al. *Green Radio Communication Networks*. Cambridge University Press, 2012.

[70] Nasir, Ali A., et al. "Non-Coherent FSK: An Attractive Modulation Set for Millimeter-Wave Communications." *2016 IEEE Wireless Communications and Networking Conference*, 2016, doi:10.1109/wcnc.2016.7565093.

[71] Hans, Shifali, and Anand Nayyar. “A Review of De-Facto MAC Standard: IEEE 802.11 DCF.” *2014 Fourth International Conference on Advanced Computing & Communication Technologies*, 2014, doi:10.1109/acct.2014.19.

[72] Bublil, B. “Suboptimal Noncoherent Detection of CPFSK.” *Proceedings of 19th Convention of Electrical and Electronics Engineers in Israel*, doi:10.1109/eeis.1996.567016.

[73] McClaning, Kevin, and Tom Vito. *Radio Receiver Design*. Noble Pub. Corp., 2000.

[74] Xiong, Fuqin. *Digital Modulation Techniques*. Artech House, 2006.

[75] Samimi, Mathew K., and Theodore S. Rappaport. “3-D Millimeter-Wave Statistical Channel Model for 5G Wireless System Design,” *IEEE Transactions on Microwave Theory and Techniques*, vol. 64, no. 7, 2016, pp. 2207–2225., doi:10.1109/tmtt.2016.2574851.

[76] Viswanathan, Mathuranathan. *Digital Modulations Using Matlab Build Simulation Models from Scratch*. Editor No Identificado, 2017.

[77] Sagari, Shweta, et al. “Equivalent Tapped Delay Line Channel Responses with Reduced Taps.” *2013 IEEE 78th Vehicular Technology Conference (VTC Fall)*, 2013, doi:10.1109/vtcfall.2013.6692193.

[78] Kwatra, S. C., et al. Investigation of near Shannon Limit Coding Schemes. *National Aeronautics and Space Administration, Glenn Research Center*, 1999.

[79] Proakis, John G. *Digital Communications*. McGraw-Hill, 2001.

[80] "Innovation in 5G with concept of 4G and 3G – books pearl", *Bookspearl.com*, 2019. [Online]. Available: https://bookspearl.com/innovation-in-5g-with-concept-of-4g-and-3g/. [Accessed: 25- Nov- 2019].

[81] Digham, F.f., and M.-S. Alouini. “Adaptive M-FSK Modulation for Power Limited Systems.” *Proceedings IEEE 56th Vehicular Technology Conference*, doi:10.1109/vetecf.2002.1040795.

[82] Digham, F.f., et al. “Variable-Rate Variable-Power Non-Coherent M-FSK Scheme for Power Limited Systems.” *IEEE Transactions on Wireless Communications*, vol. 5, no. 6, 2006, pp. 1306–1312., doi:10.1109/twc.2006.1638651.

[83] J. Monserrat, G. Mange, V. Braun, H. Tullberg, G. Zimmermann and Ö. Bulakci, "METIS research advances towards the 5G mobile and wireless system definition", *EURASIP Journal on Wireless Communications and Networking*, vol. 2015, no. 1, 2015. Available: 10.1186/s13638-015-0302-9.

[84] C. Gentile et al., "Millimeter-Wave Channel Measurement and Modeling: A NIST Perspective", *IEEE Communications Magazine*, vol. 56, no. 12, pp. 30-37, 2018. Available: 10.1109/mcom.2018.1800222.

[85] MiWEBA Project homepage http://www.miweba.eu (FP7-ICT-2013- EU-Japan, project number: 608637)," 2013.

[86] "mmMAGIC – mm-Wave based Mobile Radio Access Network for 5G Integrated Communications", *5g-mmmagic.eu*, 2019. [Online]. Available: https://5g-mmmagic.eu/. [Accessed: 25- Nov- 2019].

[87] T. Rappaport, Y. Xing, G. MacCartney, A. Molisch, E. Mellios and J. Zhang, "Overview of Millimeter Wave Communications for Fifth-Generation (5G) Wireless Networks—With a Focus on Propagation Models", *IEEE Transactions on Antennas and Propagation*, vol. 65, no. 12, pp. 6213-6230, 2017. Available: 10.1109/tap.2017.2734243.

APPENDIX A

FREQUENCY MODULATION & DEMODULATION

In a digital communication system, the modulator maps a sequence of binary digits into a set of corresponding signal waveforms. The digital modulation allows us to construct signal waveforms that correspond to multidimensional vectors, and these can be represented in signal space diagrams.

One way of creating multidimensional signals is to use M equal energy orthogonal signal waveforms that differ in frequency. Consequently, each transmitted symbol is assigned a specific frequency, and the corresponding MFSK signal is represented as by the following equation:

$$S_m(t) = \sqrt{\frac{2E}{T_{sym}}} \cos\left[2\pi(f_c + m\Delta f)t + \phi\right], \quad \text{(A.1)}$$

where m = 1,2,...,M, with M equal to the number of transmitted symbols in the set, T_{sym} is the symbol duration, E is the signal waveform's symbol energy, Δf is the spacing between any two adjacent frequencies, f_c is the base carrier frequency and ϕ is an arbitrary constant for the phase angle.

In M-ary Frequency-Shift Keying (MFSK), M carrier frequencies are set with a specified bandwidth and spacing to represent M digital symbols. This modulation has been widely used in radio broadcasting, wireless modems, and fax modems.

From a hardware perspective, there exist several ways to generate the FSK signal, known as modulation of the data stream:

1) Direct modulation using Voltage Controlled Oscillator (VCO), a device whose frequency changes linearly with an input voltage, so the output is a different frequency when the data as input changes.
2) Indirect modulation using crystal oscillators and frequency mixers, which create new frequencies with the local oscillator and the input frequency.

Demodulation is performed by detecting the frequency of the signal during the symbol period. To recover the signal, there are multiple types of demodulation techniques:

1) Foster Seeley Discriminator: (for binary FSK) presents the use of a transformer tuned to the "mark" (binary 1) frequency to demodulate the signal. In case the input is the mark frequency, the output is maximum. As the frequency shifts from the tuning frequency of the transformer, the output is a voltage proportional to the frequency shift from the tuning frequency.
2) Phase-Locked Loop (PLL): this device ensures having a fixed phase sinusoid at its output. Thanks to the feedback applied to the PLL, the input signal is regenerated, deleting all unwanted distortion.
3) Converting FM to AM: demodulation is accomplished by a frequency discriminator followed by an envelope detector.
4) Digital FM demodulator: for FSK, the set of transmitted signals is used at the receiver as local oscillator signals that are mixed with the received signal. Mixer outputs are integrated over a symbol time, and integrator outputs are sent to the symbol decision circuits.

After applying one of the methods, the original data stream will be recovered. However, in common modern data transfer applications, the signal must be filtered and amplified, among other techniques required to ensure the correct demodulation and avoidance of symbol errors.

APPENDIX B

NON-COHERENT DETECTION

From the communication channel and implementation aspects of communications, the transmission environment may be sufficiently challenging, e.g. a multipath fading channel, such that acquiring and tracking a coherent demodulation reference signal is practically difficult. Even though the information is transmitted either in amplitude or frequency only, not in the phase of the carrier, coherent receivers require exact knowledge of the channel phase for optimum performance. Even though exploiting the phase of the signal can achieve better performance, for such short wavelength mmWave signals where the phase is changing rapidly, phase estimation will often be a very difficult task.

On the other hand, with noncoherent detection, the carrier phase is not recovered at the receiver. For non-coherent detection of the signal, it is required that the spacing between carrier frequencies is a multiple of the data rate to obtain orthogonality:

$$\Delta f = n\frac{1}{T} \tag{B.1}$$

where n is an integer, T is the symbol time and Δf is the spacing between carrier frequencies. For example, in the BFSK case, the spacing between both signals is the bit rate. Two signals e.g., f and g are considered to be orthogonal and don't produce any interference between them when their dot product is zero.

$$< f, g > = \int_{t1}^{t2} f(t)g(t)dt \quad \text{(B.2)}$$

The equation for an example transmitted signal is,

$$S_i(t) = \sqrt{\frac{2E}{T}}\cos(2\pi f_c t), \qquad 0 \le t \le T \quad \text{(B.3)}$$

and for the received signal, in an AWGN channel is,

$$R_i(t) = \sqrt{\frac{2E}{T}}\cos(2\pi f_c t + \Phi) + n(t) \qquad 0 \le t \le T \quad \text{(B.4)}$$

where Φ is the random variable representing an arbitrary phase. For a mmWave carrier, the value of f_c is very large and λ_c is very small, e.g., at 30 GHz, wavelength ~ λ_c=1 cm, therefore, a change in radio path length of only 1 cm causes a 2π change in carrier phase. For example, if a vehicle (aircraft) travelling 1000 km/h or 278 m/s experiences a carrier phase change of $\frac{278}{0.01}2\pi$ = 55600 π rad/s. Rather than try and track this rapidly varying carrier phase, we may use a non-coherent receiver that does not require tracking the carrier phase.

Example: Consider noncoherent BFSK waveforms,

$$S_1(t) = \sqrt{\frac{2E}{T}}\cos(2\pi f_c t), \quad \text{(B.5)}$$

$$S_2(t) = \sqrt{\frac{2E}{T}}\cos(2\pi(f_c + \Delta f)\, t) \quad . \quad \text{(B.6)}$$

If these waveforms are transmitted on an ideal channel with a propagation delay t_d, then the noiseless received waveforms are:

$$R_1(t) = \sqrt{\frac{2E}{T}}\cos(2\pi f_c(t - t_d)) = \sqrt{\frac{2E}{T}}\cos(2\pi f_c + \Phi_1) \quad \text{(B.7)}$$

$$R_2(t) = \sqrt{\frac{2E}{T}}\cos(2\pi(f_c + \Delta f)\,t - 2\pi(f_c + \Delta f)t_d) = \sqrt{\frac{2E}{T}}\cos(2\pi(f_c + \Delta f)\,t + \Phi_2) \quad \text{(B.8)}$$

where $\Phi_1 = -2\pi f_c t_d$ and $\Phi_2 = -2\pi(f_c+\Delta f)\,t_d$. If we choose $\Delta f = \frac{1}{T}$ then received waveforms $R_1(t)$ and $R_2(t)$ are orthogonal regardless of Φ_1 and Φ_2.

After receiving the modulated signal, demodulation must be performed to recover the original data stream. Several operations must be applied to the signal to get the data stream.